INAUGURAL-DISSERTATION

zur
Erlangung der Doktorwürde
der
Naturwissenschaftlich-Mathematischen Gesamtfakultät
der
Ruprecht-Karls-Universität
Heidelberg

vorgelegt von
Diplom-Physikerin Isabell Düwel
aus Marbach am Neckar

Tag der mündlichen Prüfung: 4. Mai 2007

Spray combustion diagnostics with tracer-based laser-induced fluorescence imaging

Gutachter:

Prof. Dr. Christof Schulz

Prof. Dr. Jürgen Wolfrum

Zusammenfassung

Um die Vorgänge bei der Verbrennung in modernen Motorentypen, wie z.B dem direkteinspritzenden Benzinmotor, besser verstehen und optimieren zu können, haben sich in den letzten Jahren berührungsfreie, laserbasierte Diagnostik-Methoden als besonders vielseitig und hilfreich erwiesen. Die meisten Motorenentwickler benutzen heutzutage bei ihrer Arbeit optische Messtechniken. Um jedoch sicherzustellen, dass diese Methoden genaue und zuverlässige Ergebnisse liefern, ist es nötig, sie genau zu überprüfen und zu charakterisieren.

In dieser Arbeit werden eine Reihe von optischen Diagnostiktechniken für die Sprayanalyse, die auf dem Prinzip der laserinduzierten Fluoreszenz (LIF) von Tracern basieren, auf ihre Anwendbarkeit und ihre Grenzen hin untersucht. Die Methoden wurden dazu auf unterschiedliche Spraysysteme angewendet: Von der Anwendung in einzelnen Tropfen über Modelsprays bis hin zu Kraftstoffsprays in Versuchsmotoren.

Tracer-LIF basiert auf fluoreszierenden Substanzen, die dem Kraftstoff in geringen Mengen beigemischt werden. Deren Fluoreszenzeigenschaften werden dazu verwendet, lokale Größen wie Tropfentemperatur, -größe oder -geschwindigkeit mit hoher Zeitauflösung zu messen. Aus diesen Größen können wichtige Schlüsse über Wärme- und Stofftransportprozesse, die bei der Sprayverbrennung ablaufen, gezogen werden. Jedoch müssen die Eigenschaften der Tracer dazu sehr genau bekannt sein, um verwendbare und vergleichbare Ergebnisse zu garantieren. In dieser Arbeit wurden Tracer im Hinblick auf ihre Verdampfungseigenschaften und die Temperaturabhängigkeit der Fluoreszenzeigenschaften charakterisiert. Außerdem wurden die Farbstoffe Atto 680, Rhodamin 800 und Rhodamin B auf ihre Anwendbarkeit als Tracer in realen Kraftstoffen untersucht.

Gepulste Lasersysteme und hochauflösende CCD oder CMOS-Kameras erlauben die detaillierte und zeitlich wie räumlich hochaufgelöste Untersuchung der Sprayentstehung, -verdampfung und -verbrennung mit Hilfe von Tracer-LIF. Durch Verwendung der sogenannten Laser-Lichtschnitt-Methode können die Signale in zweidimensionalen Schnittebenen simultan erfasst werden. Die Anwendung der zuvor charakterisierten Tracer auf eine Modell-Sayflammen erlaubte durch Vergleich mit den Ergebnissen neuer numerischer Spraymodelle, welche die Flammenchemie über einen Flameletansatz berücksichtigen, neue Einblicke ich diese Vorgänge. Um die Verdampfung eines einzelnen Tropfens zu untersuchen, wurde darüber hinaus eine elektrodynamische Falle konstruiert und aufgebaut, die geladene Tropfen in einem Hochfrequenzfeld über längere Zeit festhalten kann. Die Heizung der Tropfen erfolgte durch einen CO_2-Laser. Der Vergleich mit einem neuen Tropfenverdampfungsmodell, das diese Bedingungen berücksichtigt, lieferte vielversprechende Ergebnisse

In einem Versuchsmotor mit Benzin-Direkteinspritzung konnte außerdem die Wechselwirkung zwischen Kraftstoffspray und Zündkerze, die Beeinflussung des Zündfunkens, sowie die Auswirkungen von Schwankungen im Spraywinkel während der Einspritzung untersucht werden, was Aufschlüsse über die möglichen Ursachen von Fehlzündungen und unvollständiger Verbrennung lieferte. Laserinduzierte Exciplex-Fluoreszenz lieferte, zur weiteren Untersuchung dieses Sachverhalts, quantitative

Informationen über die räumliche Verteilung des zündfähigen Gemischs bei verschiedenen Benzininjektoren unter variierenden Bedingungen.

Abstract

To understand and optimize the combustion processes in new types of internal combustion engines, like gasoline direct-injection engines, non-intrusive laser-based diagnostics methods have proven to be versatile and important tools to measure combustion characteristics. Most engine developers already rely on optical methods in the development of new engines. To guarantee accurate and reliable results of optical measurements it is necessary to carefully evaluate and characterize these techniques under realistic conditions.

In this work a variety of laser-based diagnostics techniques, mostly based on the tracer-LIF principle, have been evaluated for their applicability and limitations and have been applied to different spray systems – reaching from single droplets, over model sprays to fuel sprays in a firing test engine.

The tracer-laser-induced-fluorescence (LIF) method is based on doping the fuel with a fluorescent substance whose fluorescence characteristics are used to measure various physical properties of the spray, such as temperature, droplet size, or droplet velocity. From these properties information about heat and mass-transfer mechanisms in the spray can be gained. However, the characteristics of the used tracers must be known in detail in order to guarantee useful and comparable results. Therefore, in this work various tracers were characterized in terms of their evaporation and temperature-dependent properties. The tracers Atto 680, Rhodamine 800 and Rhodamine B have further been tested for their applicability to realistic fuels.

High-repetition-laser systems and high-resolution CCD or CMOS cameras allow the detailed analysis of spray formation, evaporation and combustion by tracer LIF with high temporal and spatial resolution. The so-called laser-light-sheet method provides two-dimensional information from the area of interest. The application of the before characterized tracers to a model spray burner provided new insights into these processes by comparison with numerical spray simulations implementing detailed chemistry through a spray flamelet model. To study the evaporation of a single droplet, an electrodynamic levitator (Paul-trap), that traps charged droplets in high-frequency electric field, was designed and setup. The droplet was heated by a pulsed CO_2-laser. Comparison with an new droplet evaporation model, that implements these conditions, showed promising results.

In addition, in a gasoline direct-injection test engine the interaction of spray and spark plug, the influence of the spray on the spark and the effect of fluctuations in the spray angle during injection were analyzed and provided insight into the reasons of misfires and partial burns. Further, laser-induced exciplex fluorescence yielded information about the spatial distribution of the ignitable fuel/air mixture for different gasoline injectors at varying conditions.

Contents

1 Introduction

Recent indications of global warming, the limitations in resources of fossil fuels and the growing demand of energy and mobility throughout the world have been leading to an increased need of research and development of new, cleaner, and more efficient technologies for energy production and propulsion. The generation of fuels from regenerative sources may still be far from widespread application, innovative combustion technologies meanwhile promise a severe reduction of fuel consumption and pollutant emissions. The combustion of liquid fuel sprays plays an important role in many of these concepts, especially concerning propulsion systems for passenger cars.

To understand and optimize the combustion processes in these new types of internal combustion engines, non-intrusive laser-based diagnostic methods have proven to be a versatile and important tool for measuring combustion characteristics. Most engine developers are already relying on optical methods in the development of new, more efficient and reduced-emission engines [1]. Many properties of the liquid fuel spray have crucial influence on the combustion efficiency: The local droplet size, temperature and number density defines the evaporation rate and therefore, the ignition-stability. Liquid fuel impacting on combustion-chamber surfaces can cause pool-fires and thus increase the soot emissions. The droplet velocity field can give information on the interaction between the spray and the often turbulent flow field in the combustion chamber. Optical methods provide a way to study these processes in-situ, however, optical access needs to be provided.

There is a variety of established optical techniques for measuring droplet temperatures, size, and velocities, e.g. *Phase-Doppler Anemometry (PDA)* [2], *Fraunhofer diffraction dropsizing* [3] and *rainbow refractometry* [4]. Although these techniques are able to yield very high precision in a laboratory environment, as they are based on interference of light, they meet their limits in dense sprays, as produced by gasoline or Diesel injectors, where it is no longer possible to ensure that only one droplet is present in the measurement volume. In addition, the mentioned methods are point-measurement techniques that yield temporally-resolved information for a single point in the spray. In contrast, planar measurement techniques like *Particle-image velocimetry (PIV)* or planar *Laser-induced fluorescence (LIF)*-based methods applied in this work yield two-dimensional information and therefore provide valuable structural information. The disadvantage of planar methods is their reduced spatial resolution.

Important parameters of spray combustion, such as local droplet size, local liquid- and vapor-phase temperatures which are vital input parameters for the numerical simulation of a spray process, or concentration-distributions of liquid and vaporized fuel can be measured two-dimensionally with a laser-lightsheet setup and highly-sensitive CCD camera systems. The desired spray property can be quantified by detecting fluorescence

light from the liquid or vaporized fuel. As fuel, depending on the fuel type, shows no or fluorescence which is hard to quantify, so-called tracer substances with well-defined fluorescence properties are added to the fuel in very low concentrations. These tracers are selected according to their high fluorescence efficiency (quantum yield), absorption spectra matching the available laser light-sources and if possible evaporative behavior. Depending on the tracer and detection characteristics different kinds of spray properties can be deduced from the fluorescence signals. Tracer-LIF techniques are not limited to dilute sprays, and therefore allow two-dimensional imaging of the spray-development in e.g. a direct-injection engine. Another advantage of this method is, that by careful choice of the tracer, different spray properties, like for instance fuel vapor and liquid concentration can be measured simultaneously and are therefore directly comparable.

The data obtained by spray measurements can be used either to interpret the processes in a spray combustion system directly or as input or benchmark for advanced numerical simulations.

In order to guarantee accurate and reliable results obtained from the tracer LIF method it is necessary to evaluate and characterize the applied tracers very carefully. Two types of fluorescent tracers were applied in this work: Fluorescent organic dyes, that have the advantage of high fluorescence quantum yields, availability for a large range of excitation wavelengths and well defined fluorescence characteristics. Rhodamine B, which shows a large temperature dependence in its fluorescence intensity was used to measure the liquid-phase temperature [5] in a reacting spray, the fluorescence tracer Rhodamine 800 [6] was used in combination with Mie-scattering to measure the local Sauter mean diameter (SMD) in a Diesel spray. Both the liquid temperature and the SMD are important input parameters for spray models. The disadvantage of this type of tracers is their non-evaporative behavior. In general, in a reacting, evaporating spray a tracer will not evaporate at the same rate as the fuel. That results in a changing tracer concentration over time – an effect that can severely influence the accuracy of the results, especially for drop-sizing experiments. The second type of tracer that was studied in this work was especially chosen to overcome this problem: A co-evaporative mixture of n-hexane, fluorobenzene and n,n-diethylmethylamine that, when excited with UV laser light, forms a fluorescing exciplex [7] was used to quantitatively and simultaneously measure liquid and vapor concentrations in an evaporating fuel-injector spray. For this tracer system it is very important to quantify the effect of temperature on the fluorescence properties in order to obtain reliable results.

After the thorough characterization of a tracer substance the successful application to a spray has further requirements. The concentration must be carefully adjusted in order to ensure good signal-to-noise ratios while avoiding absorption effects. The intensity of the laser used as fluorescence-excitation source must be carefully adjusted in order to avoid saturation. In addition, LIF-techniques need calibration which often limits the precision of the method.

This work presents the application of different LIF techniques to a variety of spray systems, ranging from the gasoline spray of an optical test engine, over automotive-type injectors operated in a spray chamber and a model ethanol-spray burner down to the smallest constituent of a spray: levitated single droplets. Where possible, the tracers were dissolved (normally by the use of long-chain alcohols as detergents) in real multi-component fuels to ensure being as close to real spray combustion processes as possible.

In that way, this work shows the potentials and limitations of tracer-LIF and its qualitative and quantitative application to spray systems.

2 Modern concepts for internal combustion engines

Sprays are found in a widespread field of technical applications. One of the most important and most controversial are certainly internal combustion engines as found in passenger cars and trucks. With an increasing demand of mobility in the world, decreasing resources of mineral oil and alternative propulsion systems still being far from mass-production, it is an important mid-term task to optimize the existing internal combustion engines in terms of

- fuel consumption
- CO_2 emissions
- NO_x emissions
- unburned hydrocarbon emissions.

By taking a closer look at the different concepts that are commonly accepted as promising it becomes evident that the injection of liquid fuels into the combustion chamber and spray combustion plays a vital role in most of them. In the following section the most common concepts and their prospects and shortcomings will briefly be reviewed.

2.1 Gasoline Direct-Injection (DISI)

Efforts to reduce pumping losses and thereby improve the part-load fuel economy of gasoline engines by unthrottled stratified-charge operation began nearly a century ago [8], but only within the last decade advances in fuel injectors, engine controls and exhaust-catalyst technology have been permitting such spark-ignited direct-injection (DISI) engines to reach commercial production (see, for example [9,10]). The first generation of wall-guided DISI engines, in which the stratified charge is formed by directing the fuel spray obliquely toward a contoured piston surface, experienced disappointing fuel-economy gains. That was largely due to the limited speed-load range over which successful charge stratification could be achieved without soot emissions. It even showed increased hydrocarbon and soot emissions relative to a premixed-charge engine with comparable output. The reasons for the hydrocarbon emissions being primarily inadequate fuel confinement and lean-fringe flame quenching, soot production is dominated by pool fires supported by the film of liquid fuel remaining on the piston.

The spray-guided (SG) DISI concept, now under vigorous development worldwide, increases the speed-load range of stratified-charge operation by virtue of the close-coupled mixture preparation and ignition, while the more compact fuel cloud and reduced fuel-spray interaction with the piston reduce hydrocarbon emissions and pool-fire-generated soot. However, the close spacing of the injector and spark electrodes can

also lead to high gas-phase and liquid-phase velocities, large numbers of liquid droplets, and steep, rapidly-varying gradients in velocity and fuel-air ratio, all of which can be unfavorable to robust ignition and flame-kernel growth. Occasional random misfires are typically encountered, especially as the charge is diluted to reduce the flame temperature and hence NO production.

There were several approaches of experiments combined with modeling to examine fuel sprays, mixture preparation and combustion in a SG-DISI engine [1,11]. These studies found that, over a substantial range of injection and spark-timing conditions, multi-cycle ensemble averages of key experimental quantities – specifically, spray structure, fuel concentration near the spark gap, combustion (both the initial partially premixed flame propagation and the later mixing-limited combustion of rich products) and the overall heat-release rate – were adequately captured by computational fluid dynamics (CFD) calculations employing k-ε turbulence and two-stage combustion sub-models. Although such CFD codes predict the intensity of velocity fluctuations (via the turbulence kinetic energy), they typically do not *directly* calculate fluctuations in fuel concentration, which are important to cyclic variation in engine performance through their influence on ignition and combustion stability. As illustrated in Fig. 2.1, the cyclic variations in fuel-concentration can be very large in SG-DISI engines.

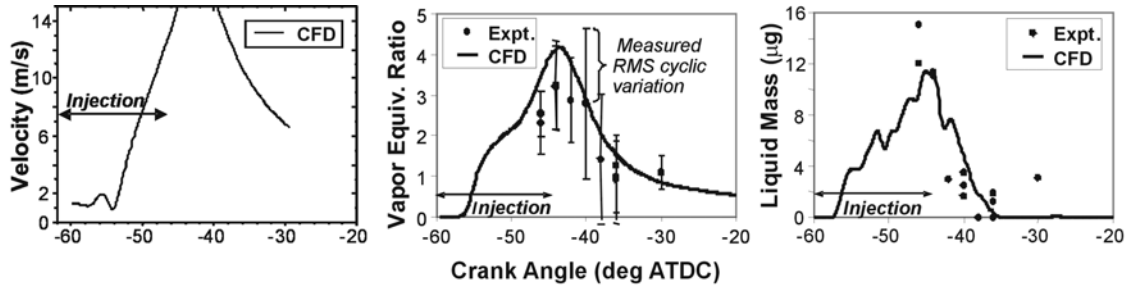

Fig. 2.1 Gas velocity and vapor and liquid fuel concentrations at the spark gap as a function of crank angle. The bars in the middle graph represent the measured rms cycle-to-cycle variation in fuel concentration. Fuel concentration is expressed as fuel-air equivalence ratio (source: General Motors Corp.)[12].

Fluctuations in concentration and velocities at the location of the spark gap – where the combustion is initiated – were identified as sources of unstable combustion behavior like misfires or partial burns. Although the rates could be reduced to about one misfire in 10000 cycles [1] that is still not acceptable for an commercial engine.

The laser-based diagnostic techniques that were applied in this work will help clarifying the reasons for these ignition instabilities and show ways to prevent them in future developments. These techniques can address various spray parameters that may have an effect on ignition stability, such as spray structure, drop size, liquid and vapor phase fuel concentrations and liquid phase temperature as will be discussed in detail in chapter 5.

2.2 Diesel direct injection

Diesel engines have the overall advantage of low fuel consumption, high torque at low engine speed and longer lifetimes, compared to gasoline engines. In recent years, since the appearance of Common Rail direct injection, Diesel engines have been conquering the passenger car market in Europe (in 2005 41% of all newly registered passenger cars and 20% of all registered passenger cars in Germany were Diesels [13]). Modern Diesel engines do not suffer from strong noise development or poor running smoothness anymore. However, emissions of Diesel engines still present a major problem.

The future development of the Diesel engine mainly goes into the direction of reduction of soot and NO_x emissions [14]. The emission regulations in Europe at this time (2006) allow particle emissions of 0.2 g/kWh (EURO IV). In 2008 the limits for NO_x emissions are going to drop from now 5 to 2 g/kWh (EURO V). In the United States these limits are even stricter: 0.1 g/kWh particle emissions (US 07). To achieve these limits advanced exhaust gas after-treatment, for example by the use of soot filters or $DeNO_x$ procedures will become necessary. However, these systems suffer from poor durability, the requirement of regeneration cycles and the need of sulphur-free fuels. In order to be able to regulate emissions by changing the engine itself, engine developers need a deeper understanding of the interrelations of the different processes during Diesel injection. Strongly depending on the respective combustion processes, the characteristics of the injection rate during one engine cycle are crucial for an optimized fuel consumption and emission. Usual regulation mechanisms like increase of the injection pressure or variation of the nozzle geometry can be complemented by optimizing the injection characteristics. If done so for every possible engine operating point, mixture preparation can be optimized and a strong reduction of NO_x, soot and unburned hydrocarbon emissions can be achieved. In order to achieve and control an optimization mechanism, reliable diagnostics techniques must be available. The high droplet density and the small droplet sizes in a usual Diesel spray form a great challenge in this context, especially for optical measurement techniques. This work presents approaches to address these problems.

2.3 Future concepts

2.3.1 Homogeneous Charge Compression Ignition (HCCI) engines

Homogeneous Charge Compression Ignition, or HCCI, engines have a long history, even though HCCI has not been as widely implemented as spark ignition or Diesel injection. In fact, HCCI was popular before electronic spark ignition was used. One example is the hot-bulb engine which used a torch-heated head to add heat to the inducted gases. The extra heat combined with compression induced the conditions for combustion to occur.

Recently, HCCI has become the subject of research due to it advantages compared to conventional engines [15,16]. HCCI is a hybrid of the traditional spark ignition (SI) and the compression ignition process (such as a Diesel engine). HCCI engines provides high thermal efficiencies and low NO_x and particle emissions. Similar to spark-ignition engines, the charge is premixed thus reducing the emissions, and as in compression-ignition direct injection engines, the charge is compression-ignited, reducing the throttling losses and leading to high efficiency. However, unlike SI or CIDI engines, the combustion occurs simultaneously and homogeneously throughout the combustion chamber volume with shorter combustion duration and is controlled primarily by chemical kinetics. HCCI engines can be scaled to virtually any size class of transportation engines as well as used for stationary applications such as power generation and pipeline pumping. Despite the advantages offered by HCCI engines, controlling HCCI combustion is a major hurdle for its commercialization.

A mixture of fuel and air will ignite when the fuel concentration is within the ignition limits and temperature of the reactants is sufficiently high. The concentration and/or temperature can be increased in several different ways, the most obvious being a high compression ratio and the pre-heating of the intake gases. Once ignited, combustion occurs very quickly. When auto-ignition occurs too early or with too much chemical energy combustion is too fast. In such cases, high in-cylinder pressures can destroy the engine. For this reason, HCCI is typically operated at lean overall fuel mixtures and thus low-load conditions.

2.3.2 Laser- or plasma-ignited engines

A different concept to overcome the ignition difficulties of stratified-load direct-injection gasoline engines is to move away from the traditional spark-plug ignition by a high voltage spark plug. One idea is to ignite with a focused laser beam of high intensity. In recent years solid-state lasers have become available that are small and robust but still able to produce output powers suitable for such a purpose [17]. The advantage of this technique is that by use of adaptive optics, it is possible to adjust the focus location to the point optimized for stable combustion, or even scan the combustion chamber to make sure, all fuel is ignited. So ignition takes place at the location of the fuel cloud no matter where it is exactly. A problem of this concept still is the provision of clean optical access to the combustion chamber throughout the lifetime of the engine.

The actual ignition, no matter if a conventional spark plug or an ignition laser is used, is caused by a locally produced plasma. In the case of the spark plug this plasma is formed between the spark electrodes by the spark discharge, in case of the laser a plasma is formed where the intensity is high enough to ionize the surrounding gas. Since plasma is the vital point in either case, the idea to produce a plasma in the whole combustion chamber more or less suggests itself. High-voltage at high-frequency is necessary to achieve this goal [18].

3 Spray modeling and model sprays

The last section showed that in order to further optimize combustion in direct injection engines (Diesel or gasoline direct-injection) it is crucial to understand the injection and the following processes of spray formation, break-up, evaporation and combustion. This can be achieved by an intelligent combination of experimental studies and numerical simulation. Experiments provide the necessary data to develop reliable and realistic models, which in turn can be tested by comparison with experiments and when the desired quality is achieved can be used to advance the optimization process. The first step in the development of new experimental and computational methods is to evaluate them on a well-known model system under defined experimental conditions.

3.1 Single droplets

The first step in understanding a spray must naturally be the understanding of its basic constituents: single droplets.

3.1.1 Evaporation models

Evaporation takes place from the surface of the droplet. Small droplets evaporate faster than big droplets because of the higher surface curvature which leads to reduced forces between the molecules directly at the surface.

The droplet radius dependent vapor pressure p is given by the Kelvin equation:

$$\ln\frac{p_0}{p} = \frac{2M\gamma}{RT\rho}\cdot\frac{1}{r} \tag{3.1}$$

with p_0 being the vapor pressure at $r = \infty$, M the molecular weight, γ the surface tension and ρ the density.

The evaporation of a single droplet is a surprisingly complex process that is governed by the initial conditions such as droplet composition, temperature, size as well as the properties of the surrounding gas. The following basic analysis according to [19] implies steady-state conditions and a single-component droplet in an atmosphere without recirculation. The temperature and concentration profiles are assumed to be determined with constant droplet radius, the surrounding gas is described as a mixture of ideal gases. Under those assumptions the continuity equation of vapor and the energy equation of the surrounding gas can be formulated as

$$r^2\rho_{gas}v_{gas}\frac{dY_{vap}}{dr} = \frac{d}{dr}\left(r^2 D\rho_{gas}\frac{dY_{vap}}{dr}\right) + r^2\dot{\omega}_{vap} \tag{3.2}$$

and

$$r^2\rho_{gas}v_{gas}\frac{dc_pT}{dr} = \frac{d}{dr}\left(\frac{\lambda_{gas}}{c_p}r^2\frac{dY_{vap}}{dr}\right) + r^2\dot{Q} \tag{3.3}$$

Here, r represents the radial coordinate, ρ_{gas} the density and v_{gas} the velocity of the surrounding gas. Y_{vap} is the mass fraction of the vapor, D the diffusion coefficient, $\dot{\omega}_{vap}$ the vapor production rate, $\dot{Q}$ the heat production rate, c_p the specific heat of the gas and λ_{gas} the heat conductivity of the atmosphere. Then, the following equation can be derived for the mass flux of the evaporated droplet liquid mass [20,21]:

$$\dot{m}_{vap} = 4\pi\rho_{gas,s} D_s r_s \ln(1+B) \tag{3.4}$$

The subscript s denotes the respective properties at the droplet surface. The so-called Spalding transfer number B, which describes the mass transfer at the droplet surface, is given by

$$B = \frac{Y_{vap,s} - Y_{vap,\infty}}{1 - Y_{vap,s}} \tag{3.5}$$

From (3.4) the well-known [20] d^2-*law* for evaporation is obtained:

$$d^2(t) = d_0^2 - \gamma t \tag{3.6}$$

where d_0 is the initial droplet diameter and γ is the evaporation coefficient

$$\gamma = \frac{8\rho_{gas} D_s}{\rho_{liq}} \ln(1+B). \tag{3.7}$$

The evaporation coefficient determines the rate of evaporation. It mainly depends on the temperature and the composition of the surrounding gas. This is described by the Spalding transfer number B. If the temperature is low and therefore the vapor concentration at the droplet surface is low (small Spalding transfer number) the evaporation will proceed much slower then for high vapor concentrations (high Spalding transfer number) at the droplet surface. Fig. 3.1 shows an example calculation for a single water droplet in an air atmosphere with an initial diameter of 100 µm at different Spalding numbers.

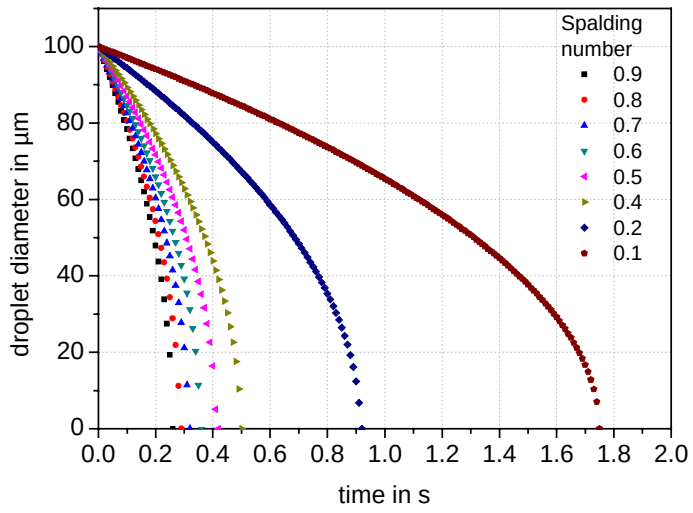

Fig. 3.1: Evolution of the droplet diameter during evaporation, calculated with a simplified d^2-model for a water droplet of d_0 = 100 µm in air for Spalding numbers from 0.1 to 0.9.

As mentioned before, this simple approach includes several assumptions [22].

- no forced or natural convection of the atmosphere
- spherical symmetry
- isolated droplets (no spray effects)
- diffusion-controlled rates are diffusion-controlled
- isobaric process
- constant gas-phase transport properties
- quasi-steady gas-phase
- single-component fuel
- constant and uniform temperature
- saturation vapor pressure at droplet surface
- no radiation effects
- solubility of the gas in the liquid is negligible

These assumptions do not hold for realistic processes as encountered, e.g. in a direct-injection engine. Depending on the conditions under which the evaporation takes place, there are more accurate but more complex numerical models to describe the process. The evaporation behavior of the droplet is governed by the relation of convective heat transport and thermal heat conduction, described by the so-called Péclet number

$$Pe = \frac{l \cdot v}{a} \tag{3.8}$$

where l is the characteristic length-scale, v the velocity and a the thermal diffusivity.

3.1.1.1 Uniform-Temperature Model/ Rapid-Mixing Model ($Pe << 1$)

In this model the simultaneous heating and evaporation cooling is considered. The droplet temperature is iteratively calculated for each time step. The thermal conductivity

is assumed to be infinite which leads to a uniform droplet temperature. This model is applicable for very small droplets with high thermal conductivity in a high-temperature environment [23]. In the case of multicomponent droplets the Uniform-Temperature Model is extended by the Rapid-Mixing-Model: Infinitely rapid mixing of the fuel components is additionally assumed, therefore no gradients in temperature or concentration need to be considered. The component with the currently highest volatility governs the evaporation. The possible formation of azeotropic mixtures is neglected.

3.1.1.2 Thin-Skin-Model/Diffusions Limit-Model (*Pe* >> 1)

In contrast, the Thin-Skin model assumes no heat transport in the droplet at all. Only the outer layer is heated, while the center of the droplet volumes remains at the initial temperature. Mass transport is considered to be purely diffusion controlled – any convection is neglected. These assumptions only hold, if the droplet reaches boiling temperature very early in the process. Therefore, this model is only applied to liquids with low boiling points and for moderate temperatures.

3.1.1.3 Conduction-Limit Model:

This is the most realistic and most general evaporation model. It solves the one-dimensional energy equations inside the droplet by means of an internal discretization scheme. The model can actually simulate evaporation processes where the heating time is in the range of the droplet lifetime. The model is accurate for a large range of temperatures and thermal conductivities, however the complexity of the computations leads to a limited applicability to technical problems.

3.2 Sprays

3.2.1 Basics of spray generation

A spray can be produced in various ways depending the field of application. The simplest technique probably is *pressure atomization* where the fluid under pressure exits through a nozzle. At the nozzle high flow velocities are encountered and the resulting aerodynamic and viscous forces lead to the formation of droplets. This type of atomizer is typically applied in engines, turbines or coating devices. With *rotation atomizers* the fluid is injected to the center of a rotating disc or bowl. Friction and centrifugal forces accelerate the liquid and form a thin film that breaks up at the rim and forms droplets. This type of atomizer is typically used in evaporation cooling or spray drying applications. *Air-assisted atomizers* use gas flows of high velocities that drags the slow liquid along. This leads to atomization even of very high-viscosity media in industrial applications. If the pressurized liquid is additionally mixed with air, tension is released abruptly at the nozzle exit and droplets are being formed – this is the principle of the *effervescent atomizer*.

The atomizer design, the liquid's viscosity, the air pressure as well as the density and temperature of the surrounding gas are the main influences on the produced spray.

3.2.1.1 Spray breakup

The mechanism of spray breakup is slightly different for different types of atomizers. Since the pressure atomizer is the most common type and the most relevant for the applications relevant in this work (fuel injection), spray breakup will be discussed for this type of atomizer. The most simple pressure atomizer consists of a nozzle with a circular hole. A jet of liquid exits the nozzle. Its diameter depends on the hole diameter. the main influence in the droplet formation process is the relative velocity of the liquid jet and the surrounding air. Four regimes can be distinguished [24]:

- **Rayleigh-breakup:** For negligible relative velocities, the liquid exits the nozzle as a cylindrical jet. The surface tension of the liquid leads to oscillations of the jet surface. This leads to a separation of parts of the liquid. These parts form droplets of various sizes larger than the nozzle diameter (see Fig. 3.2a). Monodisperse droplets can be achieved by impressing regular perturbations on the jet surface, e.g. with a vibrating orifice.
- **Small velocities:** The surface tension effects are emphasized by aerodynamic forces between the liquid and the surrounding air cause pressure gradients that amplify oscillations of the liquid surface. Droplet diameters are in the regime of the nozzle diameter (see Fig. 3.2b).
- **Unstable breakup:** With higher velocities aerodynamic forces become more and more important. The jet is sinusoidally deformed and breaks up into smaller ligaments that in turn break up into droplets. The droplets are smaller than the nozzle diameter (see Fig. 3.2c).
- **Direct atomization (high relative velocity):** the jet breaks into droplets immediately after the nozzle exit. The resulting droplets are very small. In an application this is the desired operating condition of a pressure atomizer.

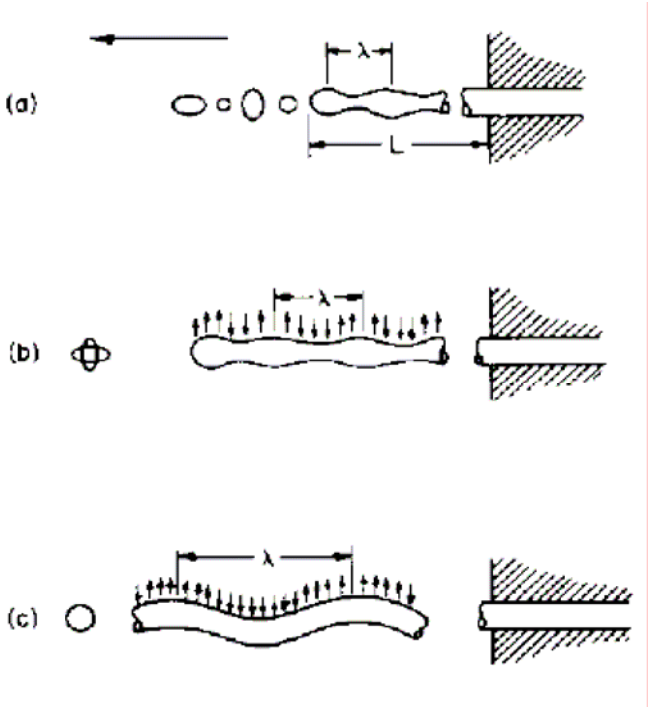

Fig. 3.2 Mechanisms of droplet formation. (a) Rayleigh breakup: oscillations at the surface. The length L until droplet formation occurs depends on viscosity and velocity of the liquid. (b) surface oscillations caused by air friction. (c) wave-like oscillations caused by aerodynamic forces.

3.2.1.2 Secondary droplet breakup

Provided that the relative velocity of the droplets and the surrounding air is high enough, the droplets can break up into smaller droplets by means of aerodynamic forces.

The relation of aerodynamic forces and the surface tension determines whether secondary droplet breakup occurs. For liquids of low viscosity like ethanol or gasoline viscous forces are negligible [24]. The higher the aerodynamic forces the more the droplets in the spray are deformed from their initially spherical shape until they break up into smaller ligaments and droplets.

Secondary droplet breakup occurs if the surface tension equals the effective aerodynamic force:

$$\pi D\sigma = \frac{1}{2} C_T A \rho_a u_r^2 \tag{3.9}$$

D: droplet diameter
σ: surface tension of the liquid
C_T: drag coefficient of the droplet
A: droplet cross-section
ρ_a: air density
u_r: relative velocity

From equation (3.9) the dimensionless Weber number *We* is obtained:

$$We_{crit} = \frac{8}{C_T} = \frac{\rho_a u_r^2 D}{\sigma} \tag{3.10}$$

The Weber number determines whether secondary droplet break-up due to aerodynamic forces is possible. Below the critical Weber number the droplet is stable. The critical Weber number depends on the droplet material and the external conditions.

3.2.2 Spray injectors in engines

In modern direct-injection internal combustion engines different types of injectors are in use that are based on varying principles and produce different types of spray shapes. For direct-injection gasoline engines the most common are the swirl injector, the multi-hole injector and the piezoelectric injector.

3.2.2.1 Swirl injectors

The High-Pressure Swirl (HPS) injectors are the most commonly used injectors in commercial applications today [25,26]. They operate at relatively high pressures (40-120 bar) and their design enhances atomization as well as turbulence levels in the combustion chamber for a more efficient combustion process. Instead of the round jet solid-cone structure common to Diesel injectors, the HPS injector produces a hollow-cone spray structure by providing a swirl rotational motion of the fuel inside the injector. Fig. 3.3 shows the geometry of a typical HPS injector nozzle.

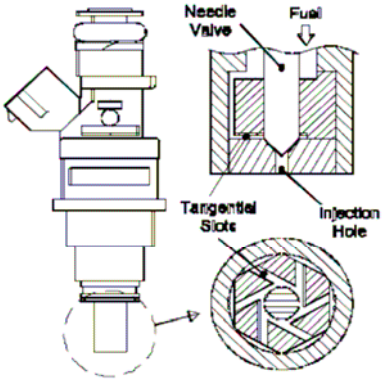

Fig. 3.3 Details of HPS injector nozzle[25].

According to the work of Chryssakis et al. [25] the development of the spray emerging from an HPS injector can be divided into two phases: the transient phase at the start of injection and the steady-state phase that corresponds to the largest part of the injection process. Upon the start of injection, due to the lack of high swirl, a solid cone-like structure appears with narrow cone angle and large droplets. As the fuel velocity inside the nozzle increases, the angular momentum and centrifugal forces also increase, thus forcing the fuel to form a hollow cone as the fuel emerges into the combustion chamber. It can be shown experimentally [9,27,28] that the higher the swirl intensity of the emerging fuel, the larger the cone angle of the resulting spray. The hollow cone formed

starts as a liquid sheet that penetrates into the high-pressure environment of the cylinder until it disintegrates into ligaments and droplets as described in the previous section.

The key advantage of HPS sprays is the high area to volume ratio, which can lead to the required level of atomization without large penetration depth. Their disadvantage, according to [29] is that the spray is very sensitive to the operating and thermodynamic conditions. Collapse of the spray angle and penetration depth for elevated chamber pressures (corresponding to the late-injection strategy) can not be avoided.

3.2.2.2 Multi-hole injectors

The multi-hole injector has been introduced in gasoline direct-injection systems to overcome the disadvantages of the HPS injector. Similar injectors have been applied in Diesel engines before [14]. Investigations on this type of injectors [30] confirmed the improved stability of the spray at elevated chamber pressures compared to swirl injectors. Also, enhanced air entrainment has been observed [29] due to the separated spray jets, and the associated larger surface area. The spray jets can be directed independently to desired locations, achieving improved matching between the injector and the combustion chamber designs.

A variety of multi-hole injector nozzle configurations has been designed and manufactured to take advantage of the flexibility in hole positioning on the injector cap (see Fig. 3.4). The nozzle geometry also defines the spray angle.

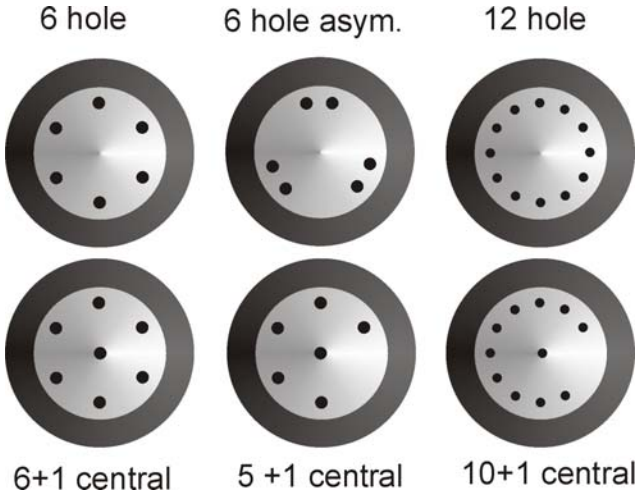

Fig. 3.4 Schematic drawing of possible multi-hole injector nozzle configurations

Multi-hole injectors are operated at injection pressures up to ~200 bar.

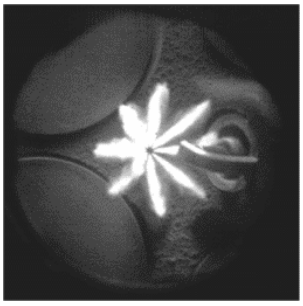

Fig. 3.5 In-cylinder image of a fuel spray in a spark-ignited direct-injection engine, produced by a eight-hole, 70° injector. One spray jet is directly directed towards the spark gap.

However, as shown in [29] and confirmed in this work, multi-hole sprays show significant cycle-to-cycle variations in spray angle and liquid distribution over time. During the opening and closing of the nozzle large droplets are produced.

3.2.2.3 Piezo-electric injectors

New generations of high pressure injectors are controlled by a piezo crystal instead of with a conventional electro-mechanical and pressure-driven control. Piezoelectric injectors are available with nozzles of multi-hole geometry and of annular cone geometry, similar to swirl injectors but without imposed pre-swirl [31]. The advantage of this injector type lies in the very short response-times of the injector needle and the low noise level caused by the comparable small movements. The result is a very stable spray that shows very small cycle-to-cycle variability.

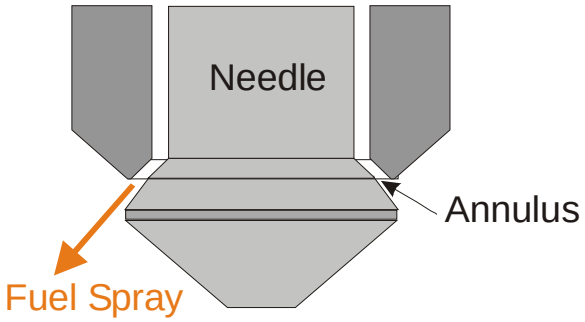

Fig. 3.6 Schematic cross- section of annular cone piezo-electric injector.

Recent studies [31,32] have shown that in contrast to swirl injectors, the spray generated by annular cone piezo-electric injectors does not tend to collapse at elevated back pressures.

3.2.3 Spray modeling

When multiple droplets are present and the average distance between the droplets comes into the range of few droplet diameters the droplets will severely influence each other. One effect that results from this is a non-steady evaporation rate. The following figure (Fig. 3.7) of the calculated concentration field around droplets in a linear chain illustrates the increase of vapor concentration between close droplets:

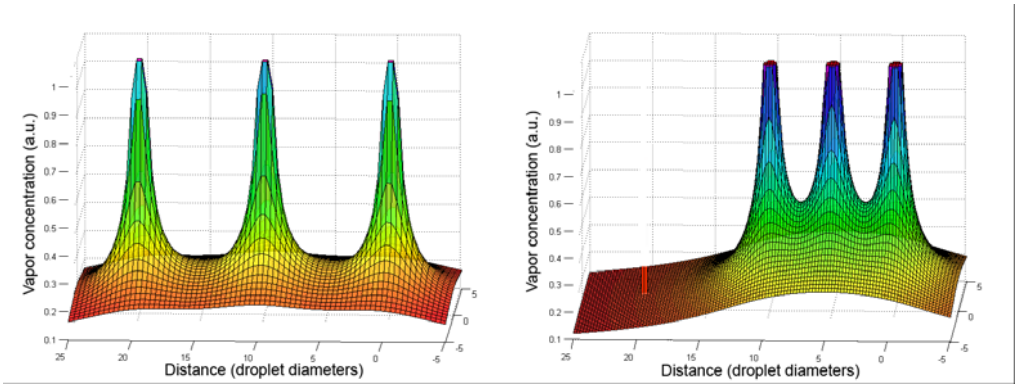

Fig. 3.7 Vapor concentration field around a linear arrangement of three droplets. Left: droplet distance = 10d; Right: droplet distance = 5d.

For droplet distances greater than ten droplet diameters the vapor concentration around one droplet does not influence the evaporation of the others (Fig. 3.7 left hand side). In the case of higher droplet number densities the vapor concentration between the droplets (Fig. 3.7 right hand side) strongly differs from the ambient vapor concentration. According to equations (3.5)-(3.7) this results in a reduction of the evaporation rate. This effect has been experimentally and computationally studied in [33,34].

In typical practical sprays, like in Diesel injection, the liquid fuel is atomized into a number of approximately 10^8 droplets [35]. As a result, direct numerical simulation of every single droplet and its influence on the other droplets is not feasible. Instead, modern CFD codes use statistical methods to describe the spray development. It is assumed that the droplets' behavior in the spray is represented by a limited number of model particles (parcels). Each parcel consists of multiple droplets with identical properties, e.g. size, temperature, and velocity. The parcels are treated as mass points and are described in a Lagrangian framework [36]. Source terms in the conservation equations are used to exchange momentum, mass and energy between the droplets and the gas phase, which is described in an Eulerian framework [37].

There are several different approaches to be found in literature to model the effects of the turbulent flow field. The most commonly used is the k-ε model which describes the development of the turbulent kinetic energy k and the isotropic dissipation rate ε [36]. The low number of additional variables leads to low computation times and high stability of this model. The applicability and accuracy depend mainly on how well the underlying equations represent the experimental conditions. More complex models like Large Eddy Simulation (LES) can be applied to a larger and more general class of problems at the cost of stability and long computation time.

3.2.4 Spray characterization

Given the initial conditions of the experiment, namely drop size and drop velocity distributions, temperature, velocity of the gas phase, spray geometry and droplet number density, the spray development, evaporation and combustion can be computed

with appropriate models. When there is a large number of particles, however, it may not be possible to measure or simulate each particle. In that case, average particle characteristics can be useful for describing a group of particles. For multiphase flows with a large variation in particle diameter, an average diameter can be employed to represent the dynamics or coupling of the particles. This can be especially important for Eulerian representations of particles. Thus, it is computationally convenient and expedient to identify an average particle diameter to represent the polydisperse distribution. For a polydisperse diameter distribution, one can define several “average” diameters.

The general average diameter of a polydisperse spray is given by

$$D_{ab} = \left[\frac{\int_0^\infty D^a P_N(D) dD}{\int_0^\infty D^b P_N(D) dD} \right]^{\frac{1}{a-b}} \tag{3.11}$$

with $P_N(D)$ the droplet size distribution of the spray.

Important average diameters are

D_{10} representing the arithmetic mean value of the droplet diameter.

D_{30} representing the arithmetic mean value of the droplet volume.

D_{32} the so-called "Sauter-Mean diameter" (SMD). A droplet with this diameter has the same volume-to-surface ratio as the entire spray. Many physical processes involve a balance between surface-averaged and volume-averaged physics, e.g., drag force vs. gravitational force, droplet vaporization rate vs. particle thermal inertia, surface tension-energy vs. particle kinetic energy, and so forth. The SMD plays an important role in the modeling of these processes.

Certain experimental techniques (described in chapter 4.3.4) allow the direct measurement of the average diameter. The planar LIF/Mie dropsizing method, for instance, directly yields the local Sauter mean diameter of a polydisperse spray.

While the representative diameters already yield useful information about a spray, for more advanced computational approaches often the entire droplet size distribution of a spray is required. Droplet size distributions can be determined experimentally as will be described in chapter 4.2.6. For many practical sprays the size distribution can be described by a lognormal distribution

$$P_N(D) = \frac{1}{h_{\ln} D \sqrt{2\pi}} \exp\left(-\frac{1}{2} \left(\frac{\ln(D/D_{\ln})}{h_{\ln}} \right)^2 \right) \quad , \tag{3.12}$$

where h_{ln} represents the lognormal spread parameter and D_{ln} represents the lognormal reference diameter.

While the lognormal distribution is the easiest possible droplet size distribution, it does not take into account the limits in drop size set up by the specific practical process and overestimates the number of large droplets in the spray. For a more accurate and detailed understanding, more complex distribution functions are needed.

The Rosin-Rammler [36] distribution gives a more precise description of the drop size distribution in most practical sprays (e.g. a high-pressure swirl-injector [25]) while still being mathematically simple:

$$P_N(D) = \frac{(D/D_{rr})^{\frac{1}{h_{rr}}-4}}{h_{rr} D_{rr} \Gamma(1-3h_{rr})} \exp\left(-\left(\frac{D}{D_{rr}}\right)^{\frac{1}{h_{rr}}}\right) \tag{3.13}$$

Here D_{rr} is a Rosin-Rammler reference diameter and h_{rr} is a spread parameter which describes the width of the size distribution. The distribution involves the Gamma function which is defined for a variable q by

$$\Gamma(q) = \frac{2}{\sqrt{\pi}} \int_0^\infty b^{q-1} e^{-b} db\,. \tag{3.14}$$

Fig. 3.8 shows both model distributions in comparison. Fit parameters typically are the reference diameter and the distribution width.

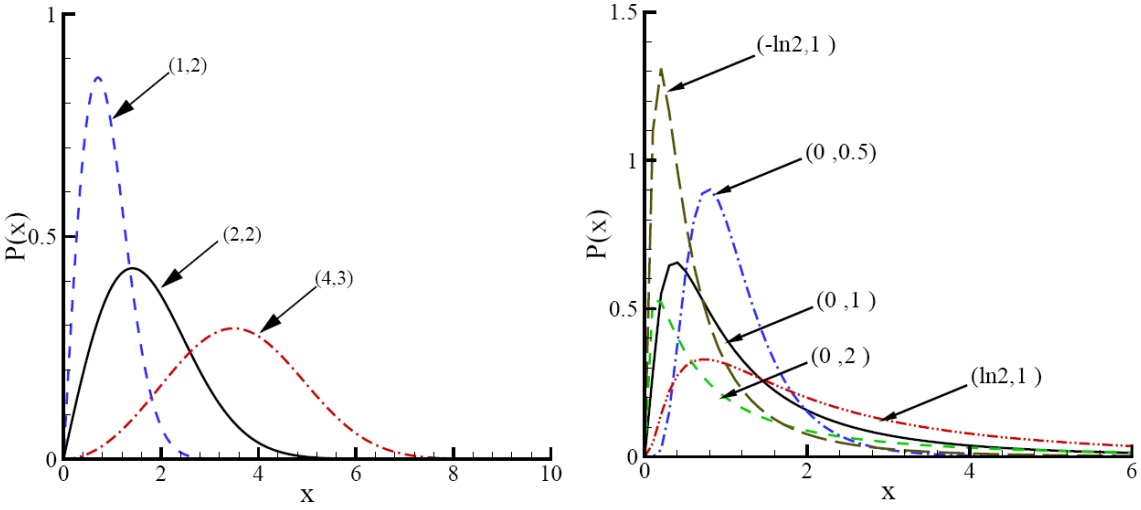

Fig. 3.8 Left: Normalized Rosin-Rammler distributions for different sets of parameters. Right: Normalized lognormal distributions (from [36]).

It can be seen that the lognormal distribution yields a larger standard deviation and includes many large droplets, while the Rosin-Rammler distribution contains more droplets with a radius closer to the SMD value.

The actual droplet size distribution of a spray can be measured with Phase-Doppler Anemometry, an optical technique that will be discussed in the following chapter.

4 Optical diagnostics

4.1 Elastic scattering

A scattering process of photons is called *elastic* if there is no energy transfer from the photon to the scattering matter. The way the photons are scattered mainly depends on the photon's wavelength and polarization, and the size, material and shape of the scattering particle.

4.1.1 Mie scattering

The interaction of electromagnetic waves with matter is governed by the Maxwell equations:

The way of describing the light scattered from small spherical particles mainly depends on the ratio of the particle size and the wavelength of the incident light. The size parameter, defined as follows,

$$\alpha = \frac{2\pi N r}{\lambda} \tag{4.1}$$

provides the distinctive criteria. Here, r is the radius and N is the refractive index of the particle. For $\alpha >> 1$ the scattering process is described by geometrical optics [38]. For $\alpha << 1$ the scattering process is described by the Rayleigh formalism, the scattered intensity mainly depends on the wavelength $\mathrm{I} \sim \lambda^{-4}$ [39]. However, for most applications addressed in this work the size parameter is in the regime $\alpha \approx 1$. For this condition the interaction of light and particle is described by Mie theory, named after the German physicist Gustav Mie (1869-1957). It is based on the application of the Maxwell equations on an isotropic, homogeneous, dielectric sphere. The model is equally applicable to spheres of all sizes, refractive indices and for radiation at all wavelengths. In the Mie formalism, Maxwell's equations are solved in spherical coordinates through separation of variables. The incident plane wave is expanded in Legendre polynomials so the solutions inside and outside the sphere can be matched at the boundary. The solution sought is at a distance much larger than the wavelength, in the so-called far-field zone. The far-field solution is expressed in terms of two scattering functions [40]:

$$S_1(\Theta) = \sum_{n=1}^{\infty} \frac{2n+1}{n(n+1)} \left(a_n \pi_n(\cos\Theta) + b_n \tau_n(\cos\Theta) \right) \tag{4.2}$$

$$S_2(\Theta) = \sum_{n=1}^{\infty} \frac{2n+1}{n(n+1)} \left(b_n \pi_n(\cos\Theta) + a_n \tau_n(\cos\Theta) \right) \tag{4.3}$$

where Θ is the scattering angle. These infinite series can be physically interpreted as a multiple expansion of scattered light. Thus, the coefficient a_1 specifies the amplitude of electric dipole radiation. The functions π_n and τ_n are given by:

$$\pi_n = \frac{1}{\sin\Theta} P_n^1(\cos\Theta) \tag{4.4}$$

$$\tau_n = \frac{d}{d\Theta} P_n^1(\cos\Theta) \tag{4.5}$$

where P_n^1 are the associated Legendre polynomials of the first kind.

Further, the scattering coefficients a_n and b_n for a perfect sphere are given by

$$a_n = \frac{m\psi_n(m\alpha)\psi_n'(\alpha) - \psi_n(\alpha)\psi_n'(m\alpha)}{m\psi_n(m\alpha)\xi_n'(\alpha) - \xi_n(\alpha)\psi_n'(m\alpha)} \tag{4.6}$$

$$b_n = \frac{\psi_n(m\alpha)\psi_n'(\alpha) - m\psi_n(\alpha)\psi_n'(m\alpha)}{\psi_n(m\alpha)\xi_n'(\alpha) - m\xi_n(\alpha)\psi_n'(m\alpha)} \tag{4.7}$$

where m is the relative refractive index of particle and medium. The functions ψ_n and ξ_n are the Riccati-Bessel functions [38].

Using the scattering functions S_1 and S_2 the scattered components of the electric field can be expressed as:

$$\begin{pmatrix} E_{\parallel}^s \\ E_{\perp}^s \end{pmatrix} = \frac{e^{ik(r-z)}}{-ikr} \begin{pmatrix} S_2 & 0 \\ 0 & S_1 \end{pmatrix} \begin{pmatrix} E_{\parallel}^i \\ E_{\perp}^i \end{pmatrix} \tag{4.8}$$

where *i* stands for the incident field, *s* for the scattered field. k is the wave vector of the incident wave. Fig. 4.1 shows a sample calculation of the scattered light intensity for a water droplet. It is visible that the highest intensity is found in forward direction.

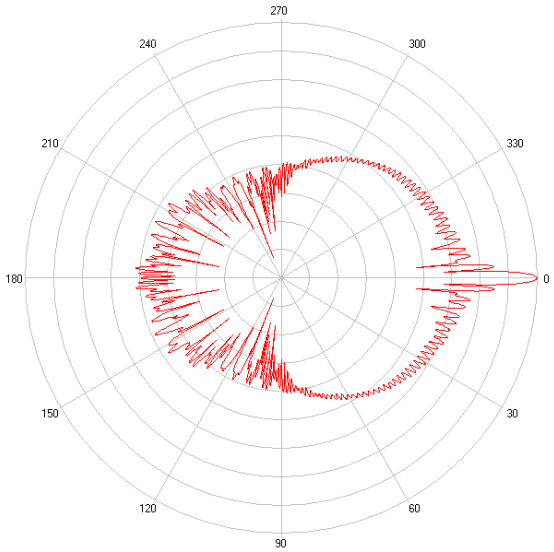

Fig. 4.1 Angle-dependent scattering intensity (parallel polarization) for a water droplet of r = 10 µm and a wavelength of λ = 650 nm. The intensity is plotted in logarithmic scale.

The absolute scattering intensity at one specific angle is very sensitively dependent on the droplet size as can be observed in Fig. 4.2 .

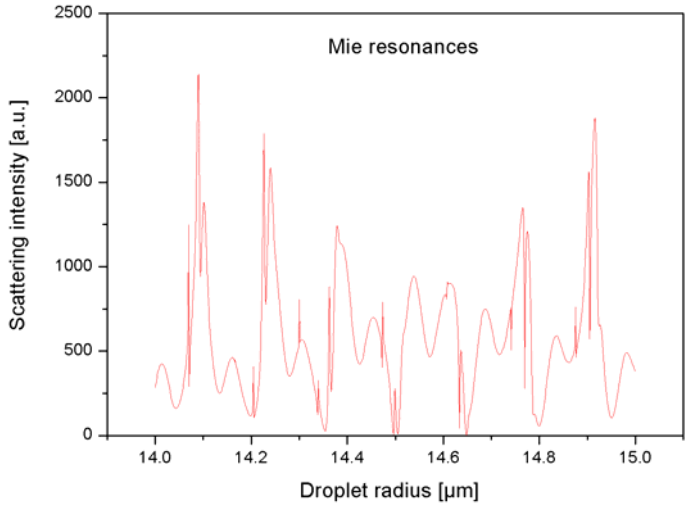

Fig. 4.2 Size dependent Mie resosances for the scattering of laser light (532 nm) in perpendicular polarization. The scattered light is detected at 90°. (Calculated with Mieplot 3.4.07[41])

The Mie-scattering signal can be used to determine various characteristics of a single droplet, such as size, velocity, temperature and refractive index. Many established experimental droplet characterization methods such as Malvern dropsizing [19] rainbow refractometry [4], Laser-Doppler velocimetry (LDV) [42] and Phase-Doppler anemometry (PDA) [42] are based on Mie theory.

4.1.2 Rayleigh scattering

If the scattering particles are single atoms or molecules (or very small particles consisting of a few molecules) of diameter d much smaller than the wavelength of the incident light

$$d << \lambda \tag{4.9}$$

all the induced dipoles will oscillate with the frequency of the electromagnetic wave. Each single molecule can be considered a single oscillating dipole emitting radiation at the same frequency. The emitted electromagnetic waves from each scattering molecule are in phase and show only constructive interference, the scattering cross-section is calculated as follows

$$\sigma_S = \frac{2\pi^5}{3}\frac{d^6}{\lambda^4}\left(\frac{n^2-1}{n^2+2}\right)^2 \tag{4.10}$$

where n is the refractive index of the scattering particle.

It is notable that the cross section and therefore, the scattered intensity increases with λ^{-4} This process is called Rayleigh scattering after Lord Rayleigh (1842-1919) who described this process for the first time in 1871 [43].

4.2 Resonant processes

A resonant interaction of light and matter starts with the absorption of a photon by the involved molecule, changing the internal energetic state of that molecule. The molecule returns to its energetic ground state by emitting a photon of a different energy. All these processes, absorption, energy conversion inside the molecule and emission shall now be discussed in detail.

4.2.1 Absorption

Resonant processes can only occur if some requirements are met:

- The energy of the absorbed photon must correspond to the energy difference between the ground and an excited state of the involved molecule (resonance):

$$\hbar\omega = \Delta E \tag{4.11}$$

- The transition between the involved energy states must be allowed – meaning the transition moment must not be zero.

In contrast to atoms, there are no strictly forbidden transitions in molecules. Depending on size and structure there are all intermediate stages between strictly forbidden and strongly allowed transitions found in molecules. The probability of transition is determined by the electronic structures of the ground and excited states. For simple molecules it can be calculated in a quantum mechanical framework. It can also be determined experimentally by measuring the strength of absorption.

For moderate light intensities the probability to find the molecule in its excited state is proportional to [44]

- the intensity of the light of the resonant wavelength
- the square of the transition moment
- the time of irradiation.

4.2.1.1 Interaction with the electromagnetic radiation field

A simple approach to describe the interaction of light and matter uses a model of two energy states. The lower state represents the ground state, the higher state represents the excited state. The following diagram depicts the different possible interaction processes:

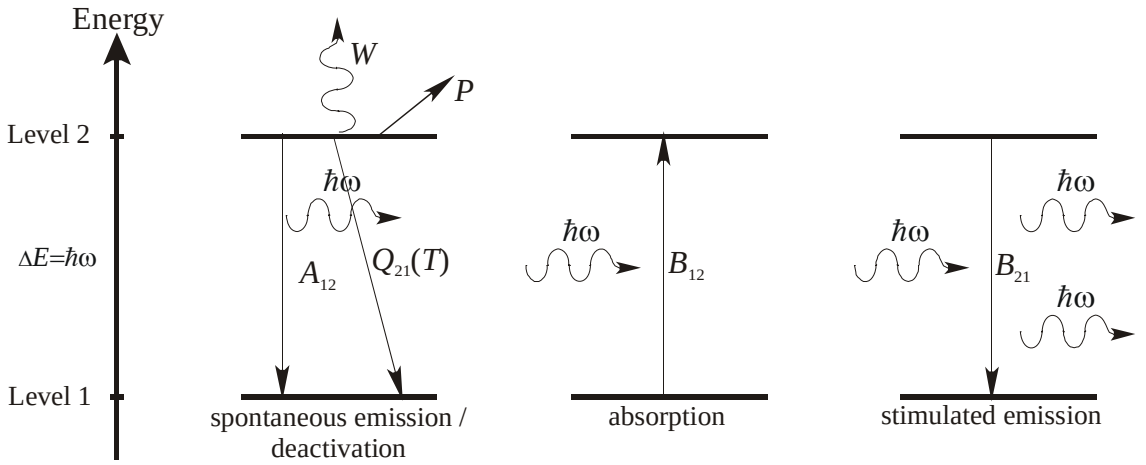

Fig. 4.3 Two-niveau model with Einstein coefficients A, B, and the quenching rate Q for the respective processes.

There are four basic processes involved:

- **Induced absorption:** If the resonance condition (4.11) is fulfilled, the absorption of a photon leads to excitation of the system to the higher energy state E_2. The probability of this process is proportional to the photon density at the location of the molecule.
- **Spontaneous emission:** Spontaneous emission happens independently of the radiation field. The emitted photon has an energy of $\Delta E = E_2 - E_1$ and is emitted into an arbitrary direction. The average time τ the system stays in state E_2 is called the *lifetime* of the energy state. The probability of transition is system specific and proportional to τ^{-1}. The emission process is stochastic in nature and therefore yields only incoherent radiation.
- **Stimulated emission:** Stimulated emission occurs when light of the appropriate energy $\hbar\omega = \Delta E$ meets a molecule in the excited energy state. The excited molecule is stimulated to return to the ground state under emission of a photon of the same energy ΔE. This results in amplification of the incident light. The emitted photon has the same direction and phase as the incident one. Therefore, both photons are considered to be coherent. The laser is based on this principle. The probability of this process is again proportional to the photon density at the location of the molecule.
- **Non-radiative deactivation:** The system can return to the ground state without emitting a photon. There are different effects resulting in non-radiative deactivation. Most of them result from the coupling of the molecule to its environment. They will be discussed in more detail in section 4.2.3.

4.2.2 Organic dyes

A substance appears a certain color if its electron shell can be excited by visible light. For molecules with fully-occupied shells the energy of visible light does not suffice for

electronic excitation – the substance appears colorless (e.g. Benzene). Thus, color results from selective absorption of certain portions of the incident visible spectrum. The rest is reflected elastically and causes the perception of color (complementary to the absorbed color). Organic molecules show color, if there are large π-systems present. For example polyenes with eight or more localized double bonds appear colored. Calculation of aborption bands of organic molecules is possible by application of a free electron gas model that was initially developed for metals to the π-electron system[45] where the electrons are treated as a one-dimensional electron gas.

An organic dye in the classical sense usually means a large organic molecule with strong absorption in the visible spectral range. There are also dyes with strong absorption in the ultraviolet as well as the near infrared spectral range. They find application for instance as laser dyes [46]. The energy absorbed by the molecule can be dissipated by emitting light or by non-radiative processes. Photochemical processes that change the structure of the molecule or lead to its destruction shall not be considered here. The Jablonski diagram in Fig. 4.4 shows the energy states of an organic dye molecule in a simplified way.

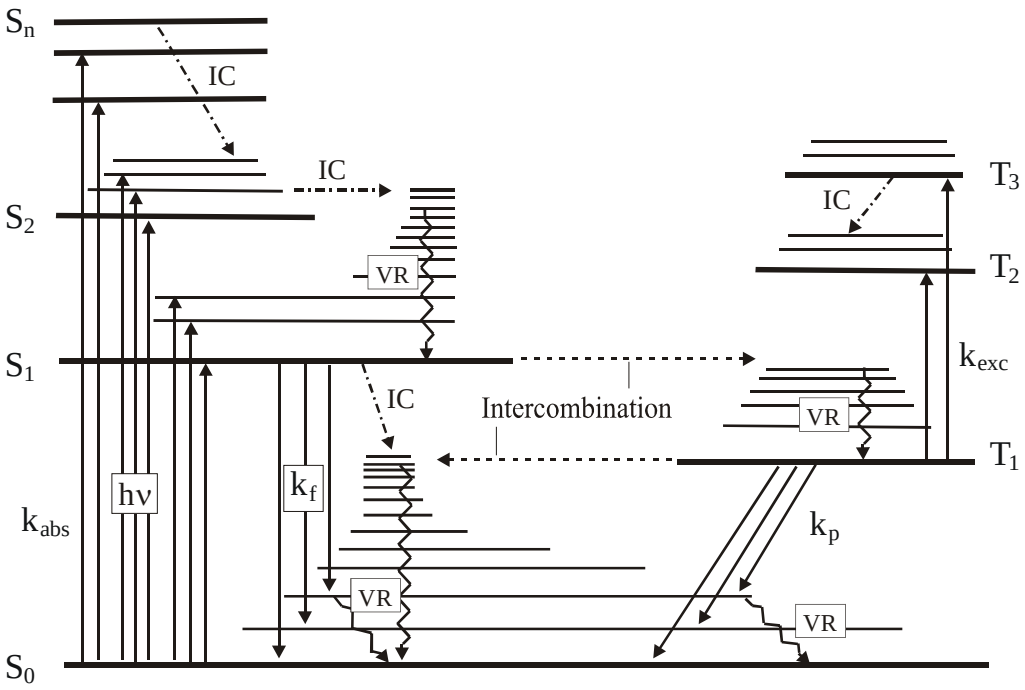

Fig. 4.4 Energy-state diagram of an organic dye (Jablonski-diagram). For simplification there are no rotational states shown. The rate constants k are reciprocal to the according lifetimes. S_i singlet states, T_i triplet states, IC internal conversion, VR vibrational relaxation, k_f rate constant of fluorescence (10^8 – 10^9 s^{-1}), k_p rate constant of phosphorescence (10^6 – s^{-1}), k_{exc} rate constant of triplet-triplet absorption, k_{IC} rate constant of non-radiative deactivation (10^{11} – 10^{13} s^{-1}), k_{abs} rate constant of electronic excitation (10^{15} s^{-1}), k_{VR} rate constant of vibrational relaxation (10^{12} s^{-1}).

By absorption of a photon the molecule is excited from the ground state S_0 to the first electronically excited state S_1. The transition moment of this process is usually very high (≈ 1). For organic dyes the energy difference of this transition is in the order of

magnitude of 1 eV (2.29 eV for Rhodamine 6G, for example). This energy difference is too high to be excited thermally, but is easily overcome by visible light.

In contrast to atoms or smaller molecules, organic dyes do not show a defined line structure in their absorption spectra but a broad absorption band that can span 100 nm or more. Organic dyes are usually large molecules consisting of many atoms. For that reason the molecule has a large number of degrees of freedom. Therefore, the electronic excitation involves a large number of rotational and vibrational transitions. Since the dye molecule is usually present in solution, the solvent induces additional line broadening that in the end lead to the broad absorption spectrum.

4.2.3 Non-radiative deactivation

4.2.3.1 Vibrational relaxation

The interaction of the excited molecule with surrounding solvent molecules can cause a loss in vibrational and rotational energy. It relaxes to a thermal equilibrium with its surrounding within 10^{-12} s. The probability distribution of states is determined by the Boltzmann distribution of the respective electronic state S_n. This leads to the so-called Kasha-rule: A molecule in solution emits light only from its lowest electronically-excited state.

4.2.3.2 Intersystem crossing (ISC)

A transition that changes the total angular momentum of the molecule is called intersystem crossing. For a given electronic configuration the triplet state is always energetically lower than the respective singlet state (Pauli principle). Therefore, the transition from singlet to triplet is energetically allowed but spin-forbidden. However, the spin-orbit coupling in molecules that contain atoms of a high atom number favors intercombination of singlet and triplet states and relaxes the selection rules.

The rate constant of ISC is in most cases comparable to the rate constant of fluorescence. It is, however, strongly dependent on the solvent. For the organic dyes used in this work (Rhodamines), the rate of intersystem crossing is about two orders of magnitude lower than the rate of spontaneous emission [47] and can therefore be neglected. These dyes were specially developed for dye lasers, where low ISC rates are essential to provide high fluorescence quantum yields.

4.2.3.3 Internal conversion (IC)

A transition from a S_1 state to a S_0 vibrational-rotational state of same energy is called internal conversion. This typically happens within the range of 10^{-11} to 10^{-13} s. The transition rate k_{IC} is the sum of the rates for each isoenergetic transition. The target S_0 state is highly excited and usually quickly loses its energy to the surrounding solvent molecules. Molecules possessing freely rotating functional groups show enhanced internal conversion. Rhodamine B, for example, has two rotating diethylamine groups

and shows a fluorescence quantum yield that is strongly dependent on the solvent temperature [47].

4.2.3.4 Triplet-triplet absorption

Each organic dye shows a characteristic T_1-T_n absorption spectrum. The long lifetimes of these states causes increasing levels of excitation up to ionization of the molecule. Followed by chemical reactions this can lead to the destruction of the molecule. Even if this does not happen, the fluorescence yield of the molecule will drastically be lowered by triplet-triplet absorption.

4.2.4 Phosphorescence

A radiative transition from T_1 to S_0 is called phosphorescence. This transition again is spin-forbidden but still possible by spin-orbit coupling. the lifetime of the triplet state however is exceptionally long, typically in the microsecond to second range. Since molecules in solution tend to lose their energy by collisional quenching, phosphorescence is usually observed in solids.

4.2.5 Laser-induced fluorescence

Within $10^{-8} - 10^{-9}$ s the S_1 ground state emits a photon and turns into a rotational-vibrational state of S_0. Usually, the target state does not yet represent thermal equilibrium so that the molecule further looses energy by interaction with its surroundings (without emitting any more photons). Therefore, the energy of the emitted photon can not exceed the absorbed energy $h\nu$ and the maximum of the fluorescence spectrum is red shifted in respect to the excitation wavelength (Stokes shift). The emission spectrum can include wavelengths shorter than the excitation if the molecule was excited thermally into a higher rotational-vibrational levels within the S_1 state before fluorescence occurred (Anti-Stokes shift). If the excitation laser pulse duration is long enough one molecule can go through the excitation-fluorescence process several times.

4.2.5.1 Fluorescence quantum yield

Not every absorbed photon is reemitted as fluorescence light. There are several processes that lead to non-radiative dissipation of the absorbed energy. The ratio of absorbed energy and energy of emitted fluorescence photons is called fluorescence quantum yield φ_F:

$$\varphi_F = \frac{\text{number of emitted photons}}{\text{number of absorbed photons}} = \frac{N_F}{N_A} \tag{4.12}$$

φ_F measures the fluorescence efficiency. Its value is mostly determined by the molecular structure and the environment of the fluorescing dye molecule.

4.2.5.2 Solvent effects

Since fluorescent dyes are mostly applied in solution, various effects of the solvent must be discussed:

- **Line broadening:** Usually an organic dye molecule consists of many atoms, a fact that would lead to a distinctive vibrational line-emission spectrum. However, the solvation shell around each fluorescing molecule has a slightly different structure, therefore, the interaction between dye and solvent is not uniform. An emission spectrum, where we usually look at a whole ensemble of fluorescing molecules, consists of the contributions from each molecule. That leads to strong broadening of the vibrational lines. At very low temperatures when the solvation shell can not change its orientation within the fluorescence lifetime a line spectrum can nonetheless be observed.
- **Relaxation:** Electronic excitation leads to spatial expansion of the electron shell. In general this means an increased polarizability and a decreased excitation energy. It also changes the dipole moment and therefore leads to a change in orientation of the nuclei and all the surrounding molecules. This process takes place within 10^{-10} s and is already finished when fluorescence occurs. Thus, the energy of the excited state is lowered at the time of emission compared to the time of absorption because of the solvent relaxation. The transition from the S_1 occurs according to the Franck-Condon law to a S_0 state with equal nuclear coordinates and equal orientation of the solvent molecules. This state is usually not in thermal equilibrium with its environment an therefore on a higher energy level then the S_0 ground state. Hence, the emission maximum always depends on solvent properties, such as viscosity and polarity.

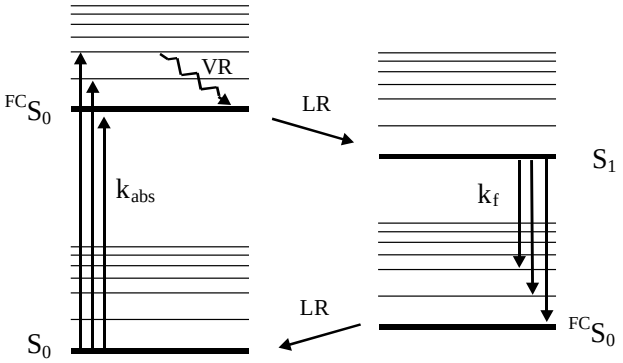

Fig. 4.5 Simplified energy level-diagram for relaxation of an excited dye molecule in solution. FC describes Franck-Condon states, that have not yet relaxed.

4.2.5.3 Fluorescence Quenching

Apart from the processes described in the section before, molecular interactions with the environment can lead to depopulation of the S_1 state. The relevant processes are:

- **Energy transfer:** Energy transfer happens if the quencher molecule Q is present in a state of equal or lower energy as the quenched molecule F. No direct contact

of the molecules is necessary for this process (dipole-diplole transfer [48]). After the interaction the acceptor molecule is excited. Because the intermolecular distances in solutions are usually very small, this energy transfer process can reach high efficiencies provided that the lifetime of the original excited state is larger than the diffusion time.

$$F^* + Q \rightarrow F + Q^* \tag{4.13}$$

According to [48] it also required that the fluorescence spectrum of the excited molecule and the absorption spectrum of the acceptor molecule overlap.

- **Quenching by oxygen:** Molecular oxygen has a triplet ground state. In connection with an excited dye molecule a complex is formed that is present in an excited triplet state. After this complex decays both molecules are in a triplet state. Effectively, the fluorescent molecule has changed from singlet to a long-living triplet state and is therefore lost for fluorescence

$$^1F^* + {}^3O_2 \rightarrow (FO_2)^* \rightarrow {}^3F^* + {}^3O_2 \tag{4.14}$$

- **Collisional quenching:** After collision of an excited dye molecule with another molecule, both molecules are in the electronic ground state. Only vibrational and rotational states are changed after the collision.

$$F^* + Q \rightarrow F + Q' \tag{4.15}$$

- **Chemical quenching:** Chemical quenching processes include complex-forming reactions, proton and electron transfer. If the dye molecules form complexes with other molecules they no longer fluoresce. The complex itself can usually not be excited either. Proton and electron transfer processes lead to non-radiative deactivation.

- **Dimerization:** At high concentrations of dye molecules and at low temperatures the probability of dimer formation increases. It is also possible for more than two molecules to accumulate, but the probability is low and it has not been observed for the types of dyes used in this work [49]. The absorption spectra of dimers show additional strong absorption at shorter wavelengths. They show very litte or no fluorescence. The precise mechanism of dimerization is not fully known. Electrostatic interactions between the polarizable chromophores or the ionic molecular groups as well as hydrogen bonds have been proposed. Dimerization is favored in aqueous solutions, whereas organic solvents do not show the effect up to very high concentrations [47].

4.2.6 Photochemical processes

A chemical reaction where one of the reaction partners must be present in an electronically-excited state is called a photochemical reaction. The different structure of the electron shell and the associated change of chemical properties enable the reaction. The photochemical process most relevant to this work is the exciplex process:

4.2.6.1 Exciplex formation

An exciplex is an unstable complex that is formed by an electronically excited molecule and a suitable reaction partner [42]:

$$M^* + G \leftrightarrow E^* \tag{4.16}$$

In which M^* is the first excited singlet state of a fluorescent exciplex-forming molecule M. This molecule will from now on be designated as “the monomer”. G (which may be identical to M) is a ground state exciplex forming molecule. E^* is the exciplex. The exciplex (short for excited-state complex) is stable only in the electronically excited state. Fig. 4.5 illustrates the intermolecular potentials of an exciplex. If both molecules are in the ground state there is no bound state for the system. If the monomer is in an electronically excited state, attractive forces between the molecules occur and they can form an excited complex at the equilibrium intermolecular distance R_e. The exciplex itself is electronically excited and therefore can undergo all processes described above. After its return to the ground state the exciplex immediately dissociates. Most interesting for practical applications is the fluorescent decay of the exciplex state:

$$E^* \rightarrow G + M + \hbar\omega \tag{4.17}$$

The fluorescence photon is significantly red-shifted compared to the fluorescence of the monomer due to the binding energy of the complex (Fig. 4.5). Because of the repulsive ground state the fluorescence spectrum of the exciplex is usually broad and without line structure.

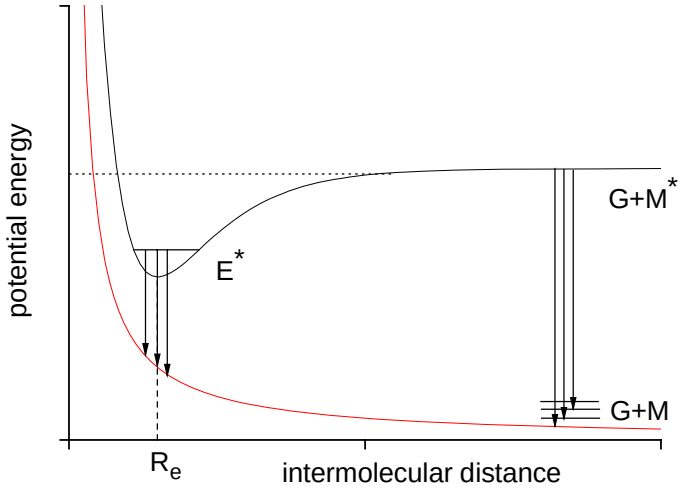

Fig. 4.5 Potential-energy diagram for an exciplex

The exciplex formation reaction is subject to chemical equilibrium with the equilibrium constant K:

$$K = \frac{\left[(MG)^*\right]}{\left[M^*\right] \cdot \left[G\right]} \tag{4.18}$$

The exciplex forming reaction (4.16) can only take place if the excited monomer M^* finds a reaction partner G within the lifetime of its excited state. Thus, the probability of an exciplex formation in solution is high if both molecules are present at high concentrations where the density is high and therefore the mean free path lengths of the molecules are short.

In a two-phase experiment the fluorescence emitted from an appropriate exciplex can be used to track the liquid phase independently from the vapor phase. In the vapor phase, the probability of exciplex formation is very low due to the low absolute concentrations (~1/1000 compared to the liquid phase). Therefore, the fluorescence emitted from the vapor phase can be solely contributed to the monomer.

In practice, the exciplex-based vapor/liquid visualization systems usually are more complex than the ideal system described above. It may not be possible to drive the reaction (4.16) all the way to the right side, so that there may be significant residual M^* fluorescence from the liquid phase. In addition, the exciplex-forming reaction and the fluorescence characteristics are strongly temperature dependent: The equilibrium constant is given by

$$K = \exp\frac{\Delta S}{R} \cdot \exp\frac{-\Delta H}{RT} \tag{4.19}$$

ΔS entropy change

ΔH enthalpy change

R = 8.314472 $JK^{-1}mol^{-1}$ gas constant

T temperature

In order to quantitatively interpret the liquid and vapor phase signals, the temperature dependence must be characterized thoroughly. In turn, if the temperature characteristics of the exciplex are known, the exciplex fluorescence can be used as a temperature probe.

4.3 Experimental methods

Elastic scattering as well as fluorescence of organic molecules provide useful tools to study spray processes from the investigation of spray formation and interaction of the droplets to evaporation and spray combustion. The use of laser light sources provides not only coherent light of high intensities but by using short laser pulses a high temporal resolution can be achieved. The methods are not intrusive, only optical access to the area of interest is needed. Detection of the desired signal is either done by highly sensitive photo detectors or two-dimensionally by CCD or CMOS cameras that will be described in detail in chapter 4.4.2.

4.3.1 Direct visualization

Basic information about a spray can be obtained by simply looking at photographs of the spray. With modern cameras images with high spatial (high pixel density) and temporal resolution (short exposure times in the regime of nanoseconds) can be recorded at high repetition rates (several kilohertz). These “movies” provide information about the spray development, the structure and shape of the spray as well as possible interactions of the spray with its surroundings. Fig. 4.6 shows an example of direct visualization of the spray inside an optical direct-injection gasoline engine. In the left image the interaction of the incoming spray with the spark plug is visible. Information from direct visualization can be the starting point for application of more complex experimental methods that yield quantitative spray properties.

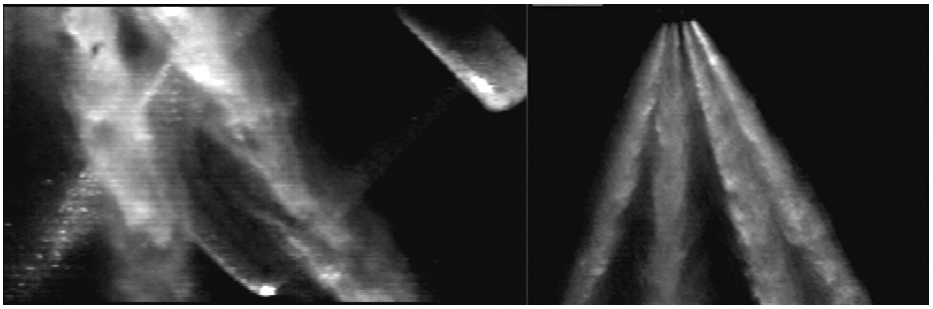

Fig. 4.6 Direct visualization of a fuel spray in a direct injection engine. Left: Interaction between spray and spark-plug Right: Multihole injector spray.

Nonetheless, direct visualization can also yield quantitative information, for example on spray angles and diameters of individual droplets.

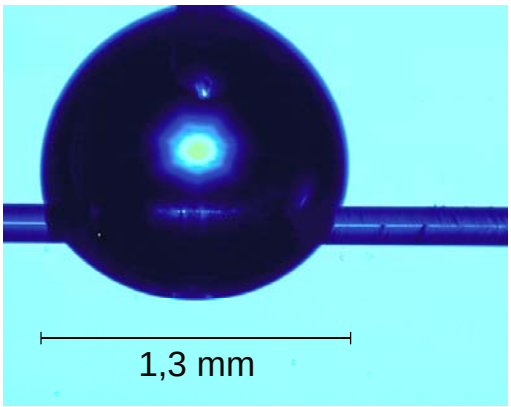

Fig. 4.7 Backlight image of a water droplet suspended on a glass fiber [50].

4.3.2 Phase-Doppler anemometry (PDA)

Phase-Doppler Anemometry [51,52] provides information about the droplet size distribution and droplet velocity distribution at a specific point in the spray. The method

is based on Mie theory as described in section 4.1.1. The measurement is performed at the intersection of two laser beams where the beams form an interference pattern. Droplets that traverse the measurement volume scatter the interference pattern. Receiving optics placed at an off-axis location focus the scattered light onto multiple detectors which convert the oscillating optical signal into a so-called Doppler burst. The amplitude of the Doppler signal follows the Gaussian light intensity profile of the laser beams. By knowledge of the fringe spacing in the interference pattern Δs, the velocity component perpendicular to the fringes can be easily calculated from the frequency f_D of the Doppler signal:

$$v = \Delta s \cdot f_D \tag{4.16}$$

Δs is given by the crossing angle 2α of the laser beams and the wavelength λ of the laser light:

$$\Delta s = \lambda / 2 \sin \alpha \tag{4.17}$$

In order to determine the droplet size from the Doppler signal, at least two detectors are needed. The different detectors are located at the same scattering angle θ but are elevated by different angles ϕ in respect to the observation plane. For a given setup, the Doppler signals detected at different elevation angles ϕ show a phase shift with respect to each other. This phase shift depends only on the droplet diameter and the refractive index. For reflected light the phase shift is given by

$$\Phi = \frac{2\pi d_p}{\lambda} \frac{\sin\alpha \cdot \sin\phi}{\sqrt{2(1 - \cos\alpha \cdot \cos\phi \cdot \cos\theta)}} \tag{4.18}$$

for refracted light, it is

$$\Phi = \frac{2\pi d_p}{\lambda} \frac{m \sin\alpha \cdot \sin\phi}{2(1 + \cos\alpha \cdot \cos\phi \cdot \cos\theta)(1 + m^2 - m\sqrt{2(1 - \cos\alpha \cdot \cos\phi \cdot \cos\theta)})} \tag{4.19}$$

.The equations (4.18) and (4.19) allow the calculation of the droplet diameter d_p from the measured phase shift. It should be stated that both terms do not contain any calibration parameters.

Fig. 4.8 shows the schematic setup of a Phase-Doppler system with two detectors.

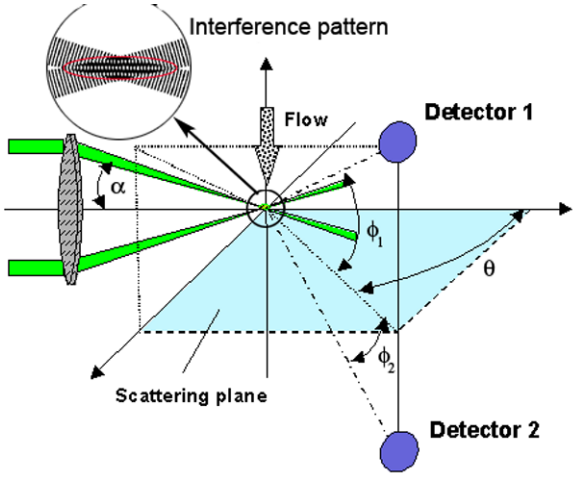

Fig. 4.8 Setup for a Phase Doppler Anemometer with two detectors. This setup measures the velocity component perpendicular to the interference fringes, i.e. in flow direction.

The phase shift increases with increasing difference between the elevation angles of the detectors. However, if the phase shift is larger than the Doppler frequency the results get ambiguous and a third detector with a smaller difference in the elevation angle is needed to remove that ambiguity [2] as illustrated in Fig. 4.9. It is apparent that the dropsize range in which the method works strongly depends on the relative detector positions. Furthermore, the use of three detectors allows additional validation of the measurement. If the resulting diameters measured by Φ_{12} and Φ_{13} do not agree within a certain tolerance range, the measurement will be discarded. It should be mentioned that the Phase Doppler method only works for spherical particles and a low-enough spray density, so that at each measurement time there is only one droplet present in the measurement volume.

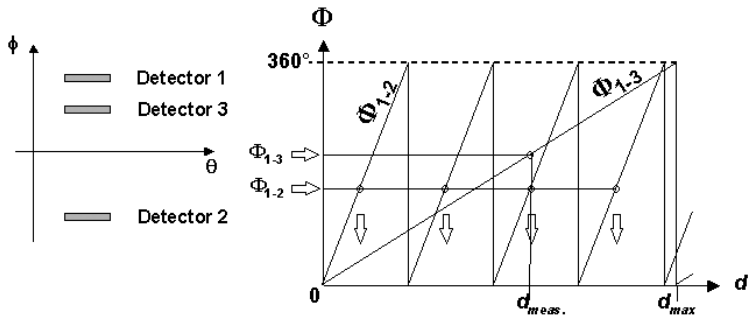

Fig. 4.9 Illustration of the phase shift ambiguity and its overcoming by application of a third detector.

In order to measure more than one velocity component the setup must be extended by a additional pairs of laser beams that form interference patterns perpendicular to the velocity component of interest. In order to keep the scattering signals separable the lasers must operate at different wavelengths.

4.3.3 Tracer LIF

Laser-induced fluorescence (LIF) is a highly sensitive method to detect molecules or species, even in very low concentrations, and has therefore become a frequently used tool in combustion and spray diagnostics. High selectivity can be achieved by tunable, narrowband laser-light sources. Short laser pulse durations provide for high temporal resolution, high enough to study turbulent objects. To study non-fluorescing materials, fluorescence tracers of high quantum yield and well-known characteristics can be added.

Below moderate tracer concentrations ($<10^{-5}$ mol/l) the fluorescence intensity is

$$I_{LIF} \propto C\varepsilon \frac{A_{21}}{Q_0\ m \exp\left(-E_a/kT\right)} \tag{4.20}$$

with the tracer concentration C, the absorption cross-section ε, the spontaneous emission rate A_{21}, and the temperature-dependent quenching $Q_0\ m \exp\left(-E_a/kT\right)$ caused by the quencher at concentration m [53]. E_a is the activation energy of the quenching process. (The expression (4.20) will be derived in section 4.3.3.5) With knowledge of all the constants and after calibration LIF can hence be used to measure the tracer concentration. If the tracer concentration in the liquid phase is known and can be assumed to be constant, the LIF signal will measure the local liquid-phase concentration – for instance in a fuel spray.

4.3.3.1 Problems and possibilities of tracer LIF

Applying tracer LIF for quantitative measurements of spray properties like D_{32}, liquid temperature or liquid and vapor-phase concentration requires thorough knowledge of the spectral properties of the tracer molecule and careful choice of tracer concentration and solvent. An ideal tracer would have the same properties as the fuel in respect to evaporation. In reality this can rarely be achieved. The tracer will evaporate at a different rate than the fuel resulting in a tracer concentration varying with time. The accuracy of measurement techniques that rely on a constant or at least a known tracer concentration (like LIF/Mie dropsizing, see 4.3.4) suffers from that effect. In [50] the error caused by different evaporation rates was systematically analyzed by comparing tracers with vapor pressures lower and higher than that of the fuel (see Fig. 4.10).

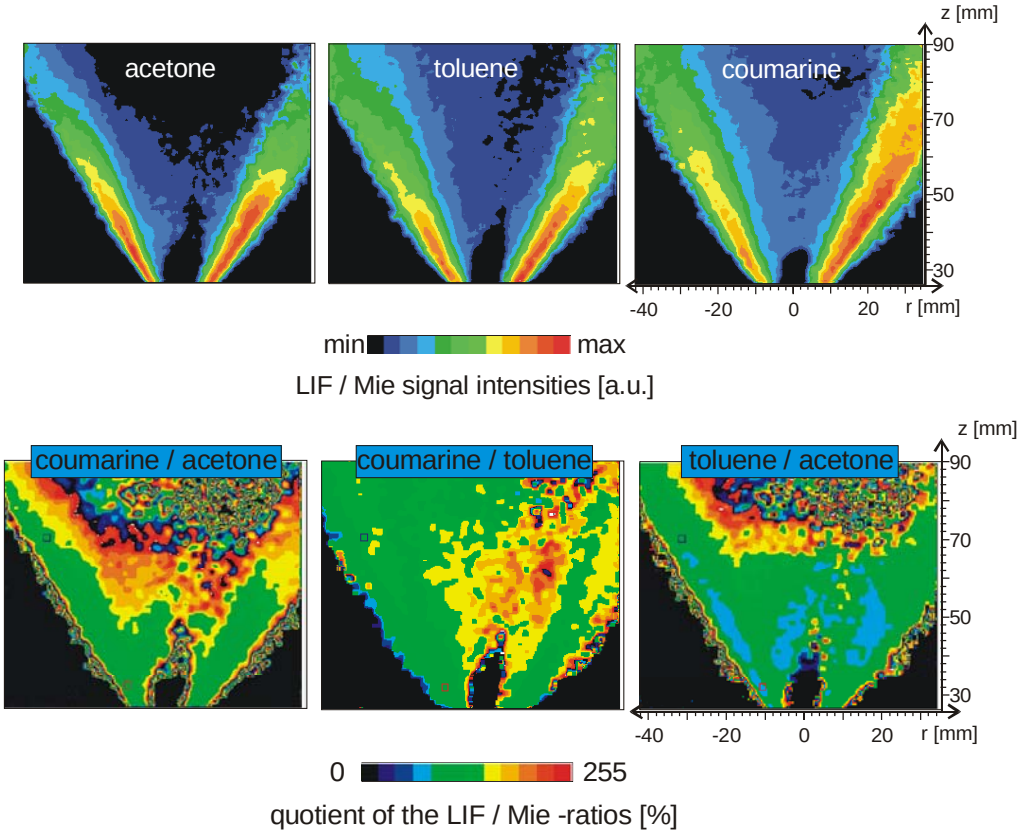

Fig. 4.10 Top row: Sauter mean diameter in an ethanol spray flame measured by LIF/Mie dropsizing using three different fluorescence tracers: acetone (higher evaporation rate than ethanol), toluene (lower evaporation rate) and Coumarine 47(does not evaporate). Bottom row: The ratios between the results for the different tracers illustrate the measurement error (from [50]).

Solid tracers that are solved in the fuel are expected to fully accumulate within the droplet during the evaporation process. Although this leads to a known total amount of tracer, the increasing concentration poses new problems: High concentrations of a tracer that is chosen to show an efficient absorption of the provided laser wavelength causes the laser beam to be partially and at last totally absorbed within the droplet – causing non-homogeneous illumination of the droplet. As the absorption and emission spectra of most tracers overlap, high tracer concentrations can also lead to signal re-absorption in case of dense sprays. Finally, for very high concentrations of accumulating tracers the linearity of the LIF signal and concentration is no longer valid [54]. The effect is exemplarily displayed in Fig. 4.11 for the laser dye Rhodamine 6G where the fluorescence signal becomes non-linear for concentrations above 0.958 mg/l (corresponding to an optical density of 0.2). Reasons for this behavior called self-quenching lie mainly in the dimerization of the tracer molecules at high concentrations [55]. Therefore, the tracer concentration should be chosen as small as possible while still providing sufficient signal-to-noise ratio.

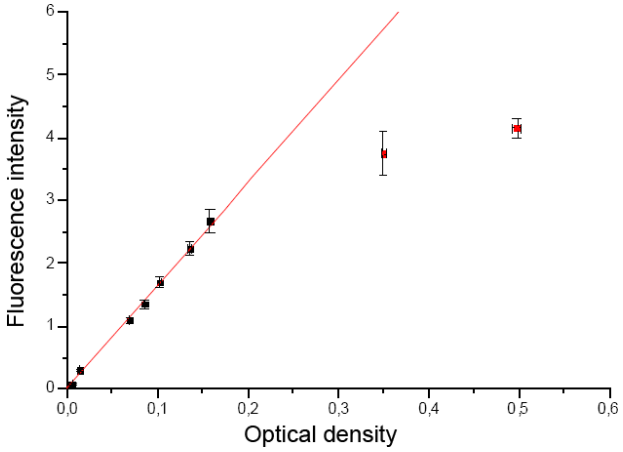

Fig. 4.11 Self-quenching of Rhodamine 6G in ethanol [56].

By using an evaporating tracer that also fluoresces in the vapor phase, it is basically possible to measure liquid and vapor concentrations in a spray. The difficulty lies in the discrimination between liquid and vapor phase. Because as an effect of density the tracer concentration in the liquid phase is expected to be higher by factor of ~10^3, the vapor phase will be very difficult to extract. To overcome this problem a tracer is needed, that shows different fluorescence characteristics in the vapor phase than in the liquid phase. (One possibility, laser-induced exciplex fluorescence, is presented in 4.3.3.3)

In addition, the application of fluorescent tracers in evaporating or even reacting sprays requires a spectral characterization of the tracer in respect to the temperature dependence of the emission. The spectral shape as well as the fluorescence intensity can be temperature dependent. This effect can be utilized to actually measure the temperature in the spray (as will be discussed later), but must be avoided or corrected for in concentration measurements.

4.3.3.2 Fluorescent dyes as tracers

Particularly in spray diagnostics fluorescent dyes as discussed in section 4.2.2 are used as fluorescence tracers. For tracer-LIF experiments to yield high-quality results, the tracer must meet several requirements: First of all it must show efficient absorption at the preferred laser wavelength, furthermore, a high fluorescence quantum yield is desired. In order to reduce deactivation effects the tracer molecule should

- have a rigid structure without rotating functional groups to reduce internal conversion, unless a strong temperature dependence of the fluorescence is desired for temperature measurement.
- show a low rate of intersystem crossing. That means the spin-orbit coupling should be weak, which can be achieved by avoiding heavy atoms in the tracer molecule.

- have a short fluorescence lifetime. That enables multiple excitation within one single laser pulse and by that reduces quenching effects.

Laser dyes such as Rhodamines usually fulfill these requirements. They are available for a large variety of excitation wavelengths. Their fluorescence quantum yield lies in a range of 0.6 - 0.99, so that small concentrations are sufficient for LIF applications. Experiments have shown that tracer concentrations below 10^{-5} mol/l do not influence the droplet, for instance in respect to vaporization [57].

4.3.3.3 Laser-induced exciplex fluorescence, LIEF

On first view LIEF provides a very convenient method for simultaneous measurement of gas- and liquid-phase fuel concentrations in an evaporating spray. The fluorescence signals of the liquid and the gas phase are spectrally well separated and therefore imaging of the evaporation process of – for example – fuel sprays in direct-injection IC engines with oxygen-free atmosphere should be possible. (Usually, exciplex fluorescence is strongly quenched by oxygen.)

However, on a closer look one realizes that reasonable quantitative analysis of LIEF signals requires thorough knowledge of the spectral properties of all the involved substances. Knowledge of the temperature dependence of the quantum yield of the liquid exciplex fluorescence as well as of the monomer fluorescence in the gas phase is especially important to quantify the signals and to correctly address the liquid/gas-phase cross-talk which is the major error source.

The fluorescence spectra of exciplex and monomer usually show a slight overlap, so that fluorescence in the monomer band contains liquid phase information that depends on the optical filter that is used to detect the vapor phase. The influence of this so-called crosstalk signal depends on the separation between the monomer and exciplex spectra, as illustrated in Fig. 4.12.

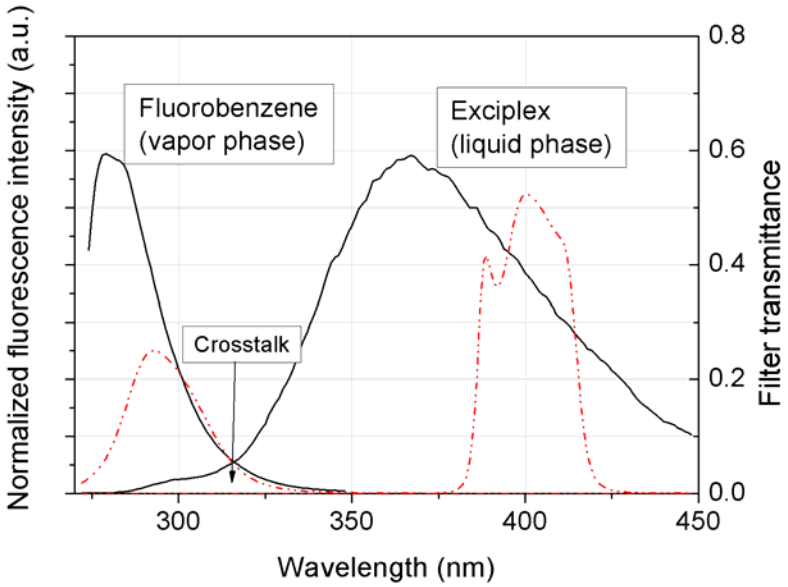

Fig. 4.12 Normalized monomer and exciplex spectra of the fluorobenzene/N,N-diethylmethylamine system at room temperature. The dashed lines denote the transmittance of optical filters suitable for this exciplex system.

For the application of the exciplex technique to the study of evaporating sprays it has to be made sure that all the exciplex components evaporate at the same rate as the fuel and form an azeotropic mixture resulting in a constant composition of the liquid and the vapor phase.

The exciplex systems reported in the literature involve the reaction of an aromatic dopant with an amine. Usually, substantial quenching of the vapor-phase fluorescence of the aromatic dopant by oxygen occurs [58]. In [59] a decrease in the fluorescence signal of the vapor phase by a factor of 40 is reported for air atmosphere compared to a nitrogen atmosphere. The reduction of total signal strength is not the only effect of oxygen presence. The fluorescence signal becomes dependent on the local oxygen concentration and does not solely represent the fuel concentration anymore [60]. This effect can be eluded by conducting LIEF experiments in a nitrogen atmosphere although this limits the technique to the study of non-reacting environments. Modern intensified CCD cameras nonetheless allow the application of this method in a firing engine as far as the low signal is concerned, as has been shown in [61], but at the cost of a fairly low signal-to-noise ratio and a considerable uncertainty concerning the vapor concentration.

4.3.3.4 LIF thermometry

According to [5] fluorescence intensity in general depends on temperature. One reason for that is that the population of vibrational and rotational levels of the molecular electronic ground state is strongly temperature dependent which can lead to significant changes in the line spectra of small molecules with varying temperature. Some

molecules in solution that usually show a broadband fluorescence can experience characteristic shifts in the fluorescence spectra with changing temperature (Rhodamine B). In addition, the fluorescence lifetimes are strongly temperature dependent due to collisional quenching. By thorough knowledge of these dependencies for certain well-behaved tracer molecules, LIF can be used to measure temperatures to a high degree of accuracy.

Ideal fluorescence temperature tracers should have the following qualities:

- High fluorescence quantum yield
- Strong absorption at the desired laser wavelength
- High temperature sensitivity in intensity or spectral shape
- No influence on the chemical reactions or fluid dynamics of the process under observation
- For fluids: similar evaporation behavior as the respective liquid

4.3.3.5 Liquid phase

According to [53], the temperature dependent LIF intensity of an organic tracer at low enough concentration to avoid absorption of the incident laser light and reabsorption of the fluorescence, is proportional to the tracer concentration C:

$$I = K_{opt} I_0 \varepsilon \varphi C \tag{4.21}$$

Where K_{opt} is a constant describing the optical setup, I_0 is the incident laser intensity, ε is the absorption coefficient at the excitation laser wavelength and φ is the fluorescence quantum yield.

The major contribution of the temperature dependence is assumed to be found in the fluorescence quantum yield. According to [62] the temperature dependence of ε is proportional to the Boltzmann fractional population of the molecules in the absorbing state. However, in condensed media, where large band-width energy levels are involved, at low temperatures (0 – 100°C), the fractional Boltzmann population is quite insensitive to temperature. The major part of the temperature dependence can be found in the fluorescence quantum yield. Quenching phenomena, which compete with the fluorescence emission in depopulation of the excited state, are all the more important when temperature is high. These phenomena correspond to non-radiative transitions, as described in section 4.2.3. The total number of possible transitions (radiative or not) per unit of time is $A_{21} + Q$, where A_{21} is the spontaneous emission Einstein coefficient and Q the rate of non-radiative losses. The spontaneous emission Einstein coefficient A_{21} depends only on the fluorescent molecule. The fluorescence quantum yield is defined by [63]:

$$\varphi = \frac{A_{21}}{A_{21} + Q} \tag{4.22}$$

For large organic tracer molecules the loss rate Q *is* assumed to be dominated by the interaction of the tracer with its surrounding. The temperature dependence of the loss rate Q can be (empirically) modeled with an Arrhenius expression:

$$Q = Q_0 e^{-E_a/kT} \tag{4.23}$$

E_a is the activation energy required for the quenching process in collisions between a fluorescent molecule and a molecule of the solvent and Q_0 is a constant. Both depend only on the properties of the fluorescent tracer and of the solvent. Further it can be assumed that the loss rate Q is much higher than the rate of radiative decay A_{21} [64]. This leads to the following temperature dependent formulation for the fluorescence intensity:

$$I = K_{opt} \varepsilon \frac{A_{21}}{Q_0} C e^{E_a/kT} \tag{4.24}$$

Two functions may now be defined, depending only on the spectral and physical properties of the fluorescent molecule:

$$K_{spec} = \varepsilon \frac{A_{21}}{Q_0} \tag{4.25}$$

and

$$\beta = E_a / k \tag{4.26}$$

From now on β will be called the temperature-sensitivity coefficient. With these two functions a consistent formulation for the temperature-dependent fluorescence signal of a fluorescent molecule is obtained:

$$I_{LIF} = K_{opt} K_{spec} I_0 C e^{\beta/T} \tag{4.27}$$

The organic tracer molecules that are considered for temperature measurement usually have broad emission spectra. In general, β depends on the excitation and the detection wavelengths. Usually the excitation wavelength is fixed by the use of a laser as excitation light source. Fig. 4.13 shows exemplary spectra of solutions of Rhodamine B in ethanol at three different temperatures excited with an Argon-Ion laser at 514 nm and the hence calculated sensitivity coefficient.

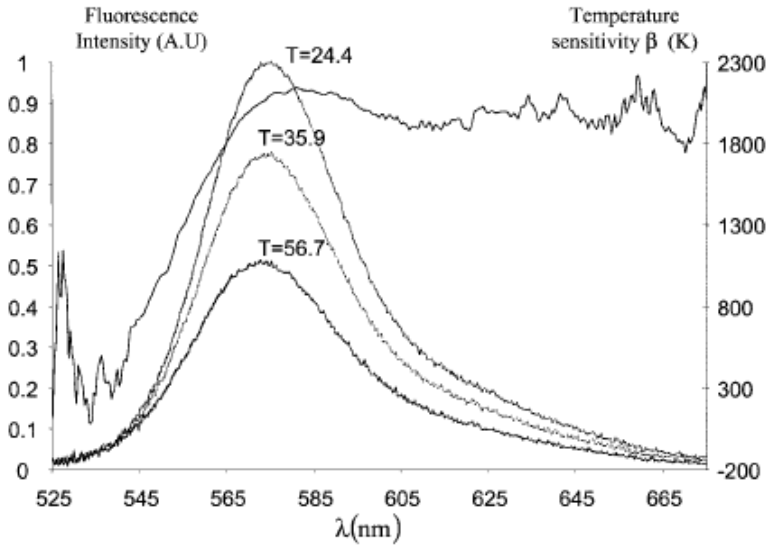

Fig. 4.13 Three spectra of Rhodamine B at different temperatures and the wavelength-dependent sensitivity coefficient β. The solvent was ethanol, the excitation wavelength was 514 nm.

The accurate measurement of temperature requires on one hand a high sensitivity in one part of the emission spectrum and on the other hand a low sensitivity in a different, spectrally well separable part of the same emission spectrum. The fluorescence signals detected in the two spectral bands can be written, according to (4.27) as

$$I_{b1} = K_{opt1} K_{spec1} I_0 C e^{\beta_1 / T}$$
$$I_{b2} = K_{opt2} K_{spec2} I_0 C e^{\beta_2 / T} \tag{4.28}$$

The ratio of the two signals allows the elimination of the laser intensity I_0 and the tracer concentration C. This means that the two-color method can also be applied in evaporating sprays where the tracer concentration C varies with time.

$$R_f = \frac{K_{opt1} K_{spec1}}{K_{opt2} K_{spec2}} e^{(\beta_1 - \beta_2)/T} \tag{4.29}$$

By measuring the fluorescence intensity ratio at an appropriate reference temperature the system dependence can also be eliminated and the fluorescence intensity ratio can be measured as a function of temperature and reference condition:

$$\ln\left(\frac{R_f(T)}{R_f(T_0)}\right) = (\beta_1 - \beta_2)\left(\frac{1}{T} - \frac{1}{T_0}\right) \tag{4.30}$$

Calibration is needed to determine the relative temperature sensitivity $\beta_1 - \beta_2$. For a single tracer molecule species, it depends on the excitation wavelength and the solvent. A high accuracy in the temperature measurement can be achieved by choosing a molecule with large gradients in $\beta(\lambda)$. The laser dye Rhodamine B, which was used in this work shows the desired behavior within a limited wavelength range, as visible in Fig. 4.13.

The described method is also known as two-color LIF thermometry. It is especially suited for two-dimensional measurements of temperature fields in sprays. In that case (4.30) is applied to each pixel of the two-dimensional spray images.

Because of strong spatial variation of signal intensity in a spray and the non-linear dependence of the signal of the signal intensity in either detection channel, it is crucial to determine the temperature for each pixel at each individual laser shot, rather than averaging signal for each channel individually, with the subsequent application of the above equations.

The accuracy of the technique could be increased by using a third detection band. Also, it can turn out be more accurate to extend the linear model for the fluorescence intensity ratio by a second order correction term.

4.3.3.6 Vapor phase

The temperature of the gas-phase is not possible with a fuel-based tracer due to the too strong signal from the droplets. Therefore, seeding the gas-phase with a temperature-sensitive tracer molecule provides a solution. NO has proven to be a suitable tracer molecule for gas-phase temperature measurements. The so-called multilane-LIF thermometry with NO allows temperature measurements in both reactive and non-reactive zones of a spray. In contrast to two-color LIF thermometry the multi-line technique yields absolute temperatures without calibration [65]. The laser is tuned over a part of the absorption spectrum of the respective molecule while individual images are taken with an intensified CCD camera for each excitation wavelength. NO is a molecule with a temperature-sensitive line spectrum that can be numerically simulated and can therefore be used as the tracer species. NO can be seeded to the unburned gas and therefore allows measurements in both, the unburned and burned gases. This is a clear advantage compared to OH thermometry that is restricted to the area of natural occurrence of this intermediate species. Usually some hundreds of ppm of NO are added to the surrounding gas as a fluorescent tracer.

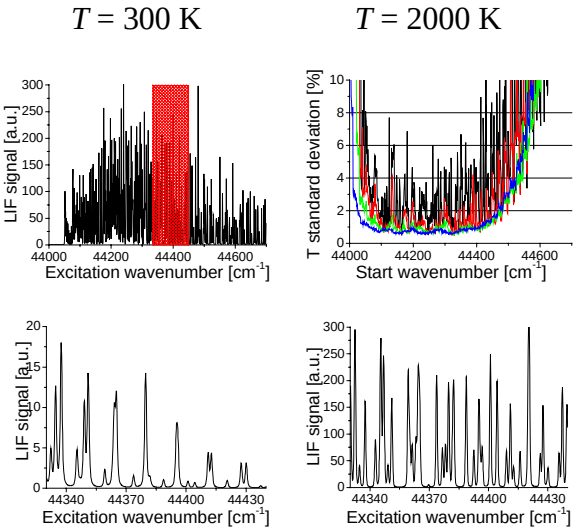

Fig. 4.14 The upper diagrams show NO-LIF excitation spectra of the entire A-X (0,0) band at 300 K (left) and 2000 K (right). The laser tuning range of the Raman-shifted KrF-excimer laser system we used is marked red. The lower diagrams show shows the detailed excitation spectra in the KrF-excimer laser tuning range.

For the best temperature precision the shape of the observed spectra should show a maximum temperature dependence. This is achieved by using a part of the excitation spectra where neighboring peaks assess transitions with a large variation in ground state energies. In order to find the best scan range within the NO A-X(0,0) band, a numerical analysis based on LIFSim [66] was performed by Helmut Kronemayer [67]. The first step is to simulate an excitation spectrum for a given initial temperature, pressure, spectral position and wavelength range. Next, one adds synthetic noise (determined before from typical experimental camera noise) to the calculated spectra. Simulated spectra are fitted to the noisy spectra with temperature as the free parameter. Finally the temperature from the fit of the noisy spectra and the initial temperature are compared. This procedure is repeated 200 times and the results are statistically analyzed and conditions with minimum standard deviations of the initial temperature are chosen. The optimum scan range depends on the temperature range of interest.

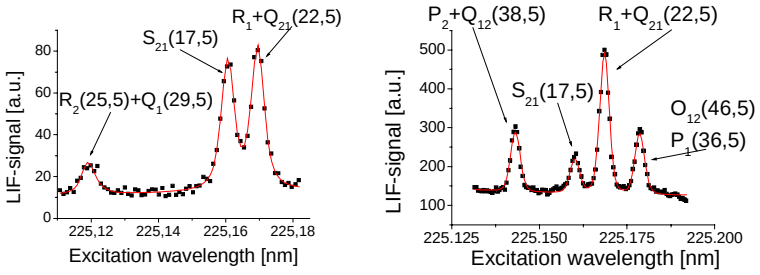

Fig. 4.15: Optimum scan range for the 300 K range (44411 – 44421 cm^{-1}, left) and 2000 K (44407 – 44417 cm^{-1}, right) Black dots are experimental data and red lines show the fitted spectra. The labeling shows the rotational ground state quantum number in the NO A-X(0,0) band.

From the resulting stack of pictures (each with the laser tuned to the next wavelength) LIF excitation spectra can be extracted for each pixel. Simulated spectra are then fitted to the experimental data with absolute temperature, broad-band background and signal intensity as free parameters. Therefore, the technique can be applied even in systems with strong scattering and fluorescence background [68]. Because the complete shape of the spectra (including line-broadening) is included in the data evaluation, the technique disregards background signal and is calibration free. NO-LIF excitation spectra are simulated using the software LIFSim [66,69].

4.3.4 LIF-Mie dropsizing

In a spray the measured Mie signal consists of the superposition of scattered light from all individual droplets. It can be shown that for a poly-disperse spray the Mie signal intensity at detection angles of 60° to 90° is proportional to the mean droplet surface area and therefore to the droplet diameter squared [54].

$$I_{Mie} \propto d^2 \tag{4.31}$$

Combined with the perception that the fluorescence of a droplet containing a solved fluorescence tracer in low concentrations is proportional to the droplet volume (if the tracer concentration is kept constant) [70]:

$$I_{LIF} \propto d^3, \tag{4.32}$$

this yields an non-intrusive measurement technique for the Sauter-mean diameter from the signal ratio of LIF and Mie [71]. For a polydisperse spray the relation between the fluorescence signal scattered light of n droplets in the measurement volume is given by

$$\frac{I_{LIF}}{I_{Mie}} \propto \frac{\sum_{i=1}^{n} d_i^3}{\sum_{i=1}^{n} d_i^2} \propto D_{32} \tag{4.33}$$

using equations (4.31) and (4.32). The actual SMD can be determined after calibration of the LIF/Mie ratio at a point of a known SMD.

The advantage of this method compared to PDA is the possibility to detect a two-dimensionally resolved distribution of local D_{32} using a laser light-sheet for excitation and two CCD cameras for detection (at the expense of not measuring size distributions but average sizes only). Also the LIF/Mie method can be applied in dense sprays that do not allow PDA measurements because of multiple scattering [72]. The accuracy of the method depends strongly on how well the exponents in equations (4.31) and (4.32) are met. Deviations of the LIF exponent can be caused by high tracer concentrations [73] that can lead to absorption of the incident laser light inside the droplet and to self-quenching (see section 4.3.3.1). The critical tracer concentration depends not only on the tracer species but also on the expected size range and refractive index of the droplets. For the Mie exponent it is crucial that the spray really is poly-disperse so that morphology-dependent Mie resonances are compensated.

4.4 Tools

4.4.1 Lasers

In recent years lasers have become a common tool in all kinds of fields. Most types of lasers (Nd:YAG, CO_2, Copper-vapor) used in this work were standard systems that have been described in detail in the literature [74,75] and will just briefly be discussed in this chapter for that reason. One laser system however, that was developed in collaboration with EADS especially for LIF application in Diesel sprays [76] shall be discussed in more detail.

4.4.1.1 Nd:YAG laser

Nd:YAG lasers are very common laser systems which have found widespread applications in industry and science. They are robust and easy to handle while providing high output energy at a good stability.

Nd:YAG is an acronym for neodymium-doped yttrium-aluminium garnet ($Nd:Y_3Al_5O_{12}$). The YAG crystal is doped with an active medium, in this case triply ionized neodymium, which replaces another ion of roughly the same size, typically yttrium. Generally the crystalline host is doped with around 1 % neodymium by weight [75]. It is pumped by either flash lamps or in more modern systems with diode lasers that specifically excite the high energy levels of the laser active medium and can therefore achieve high efficiencies. The most efficient laser transition of the Nd:YAG has a wavelength of 1064 nm.

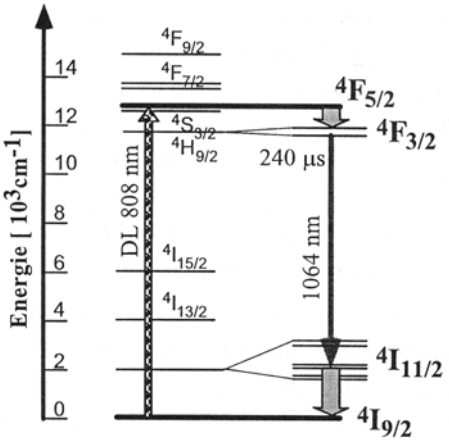

Fig. 4.16 Energy levels of the Nd:YAG laser pumped with a diode laser at 808 nm[75].

A Pockels cell within the resonator serves as active Q-switch that produces short laser pulses of 5-9 ns at high energies. For flash-lamp pumped systems a repetition rate of 10 Hz gives the best stability of the system. Diode-pumped systems can operate at several kHz. Via second-harmonic generation in a non-linear crystal, usually beta-barium borate BaB_2O_4 (BBO) behind the resonator the fundamental wavelength of the Nd:YAG laser can be converted into 532 nm (frequency doubled), 355 nm (frequency tripled) or 266 nm (frequency quadrupled).

The high pulse energies and short pulse durations make Nd:YAG lasers a very applicable tool for LIF measurements. In this work a flash-lamp pumped, frequency doubled Nd:YAG laser *(B.M.Industries, Model 5013 COMP 10)* with a maximum pulse energy of 260 mJ was applied.

4.4.1.2 CO_2 laser

The CO_2 laser, which is mainly used for industrial applications like metal processing, welding and engraving, is a powerful infrared laser source [77]. Like most gas lasers it is based on vibrational transitions. The laser medium is a gas mixture consisting of 7% CO_2, 18% N_2 and 78% He. Population inversion is achieved by a high energy gas discharge that excites the N_2 molecules with a high efficiency (the CO_2 molecules can be directly excited, too). As shown in Fig. 4.17 the excited state energy of the N_2 and the CO_2 molecule are very similar. The excited state of N_2 is a triplet state and therefore has a long lifetime resulting in a high probability of energy transfer between an excited N_2 molecule and a ground state CO_2 molecule. There are several strong transitions in the CO_2 molecule corresponding to different vibrationally excited states. The strongest transition emits infrared light at 10.6 µm. Due to the rotational splitting of the vibrational energy levels, the CO_2 laser can be tuned over a whole range of wavelengths. The CO_2 laser applied in this work (*Edinburgh Instruments, Modell PL6*) can be tuned over about 100 lines in the vibrational-rotational spectrum. The strongest line reaches 180 W. For wavelength selection a grating is used (90 lines/mm, blazing for 10 µm).

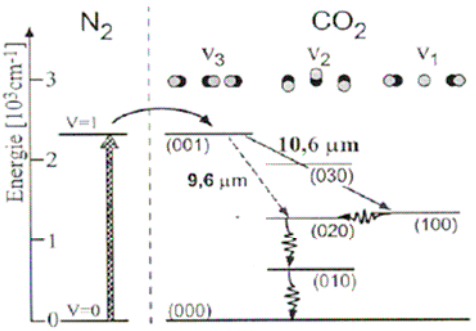

Fig. 4.17 Energy levels and intermolecular energy transfer mechanisms of the CO_2 laser [75]

For laser wavelengths in the far infrared, as produced by the CO_2 laser, common quartz optics are no longer of use. Lenses and collimating optics are usually made of ZnSe, mirrors are made of Cu, Mo or Si.

4.4.1.3 Copper-vapor laser (CVL)

As its name implies, the copper-vapor laser uses vaporized copper atoms as the lasing medium. The laser head for a copper-vapor laser is schematically shown in Fig. 4.18.

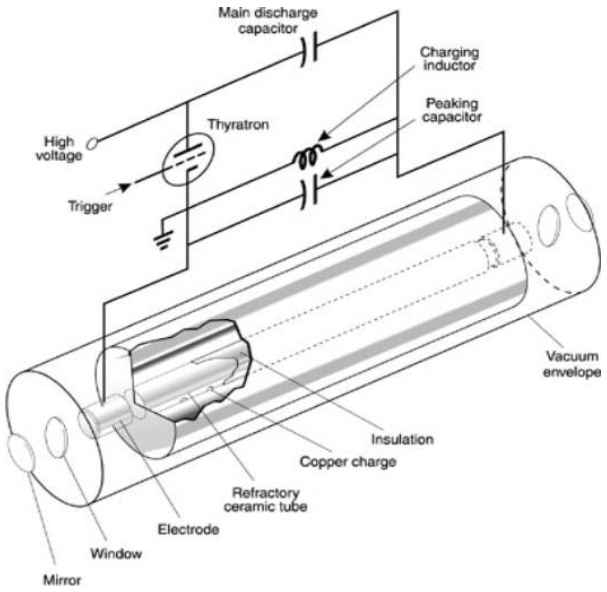

Fig. 4.18 Schematic diagram of a CVL laser head (from[78]).

The refractory ceramic tube contains pellets of copper and a low-pressure buffer gas, usually neon. A pulsed electrical discharge between electrodes at each end of the tube raises the temperature to about 1450°C producing a copper vapor at a low partial pressure. Excited electrons in the electrical discharge collide with the vaporized copper atoms and excite them in a single step to the upper $^2P_{3/2}$ and $^2P_{1/2}$ laser levels illustrated

in Fig. 4.19. The electrons in the $^2P_{3/2}$ level decay to the lower $^2D_{5/2}$ laser level producing green laser light at a wavelength of 510 nm. Transitions from the $^2P_{1/2}$ to the $^2D_{3/2}$ level produce yellow laser light at a wavelength of 578 nm.

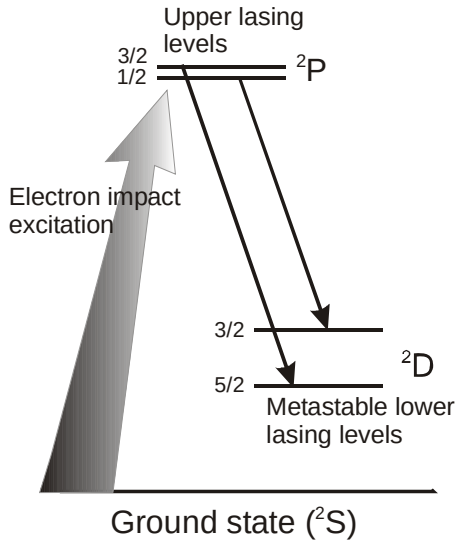

Fig. 4.19 Energy levels of a copper vapor laser

The electrons in the lower lasing level require a relatively long time to relax to the ground state, hence, the population inversion cannot be sustained continuously and the laser action self-quenches. The power of the laser is therefore contained within 5 – 60 ns pulses, each pulse having a very high peak energy; typically 1 – 25 mJ. Repetition rates of 2 – 100 kHz can be obtained. These pulse rates are higher than those of most other high-power visible laser (new diode-pumped solid-state lasers come close). It is, in fact, the copper vapor laser's combination of high power and fast pulse repetition that makes it very useful for imaging experiments in engines.

Kinetic enhancement [79] is achieved by adding a small quantity of a hydrogen halide, typically 1% hydrogen bromide, to the neon buffer gas. This addition speeds up essential chemical reactions involving copper atoms that support the lasing action, resulting in a marked increase of the laser's optical performance. Kinetic enhancement improves the following properties of the copper vapor laser:

- Output power is increased by a factor of 2-3
- Output power is almost independent of pulse repetition frequency

This property is illustrated in Fig. 4.20. Note that the time-averaged output power is almost flat from 10-40 kHz, i.e. single-pulse energy decreases.

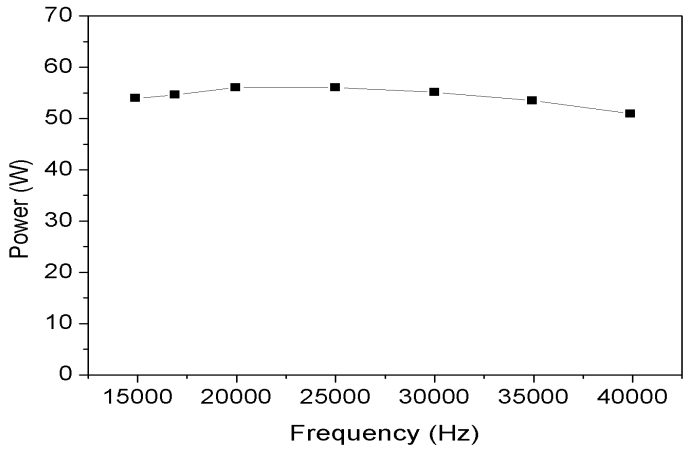

Fig. 4.20 Power-frequency relationship in an enhanced CV laser[78].

In the engine experiments described in this work a copper vapor laser (*Oxford Lasers LS-20*, 30 ns pulse duration, 2 mJ/pulse, wavelengths 511 and 577 nm) was applied at repetition rates of 9 to 13.5 kHz.

4.4.1.4 Multi-pulse diode-pumped Nd:YAP-laser

For LIF experiments in Diesel fuel (described in chapter 5.1.3) a compact all-solid-state laser was developed and constructed by Peuser et.al. [76] in order to optimally meet the requirements of the fluorescence experiments such as a laser wavelength close to 671 nm, a pulse energy greater than 1 mJ and the ability of generating pulse bursts with a minimum time interval between the pulses around 30 µs (corresponding to a repetition rate of about 33 kHz) [6]. This feature was implemented in order to have a high enough repetition rate to analyze the temporal development of the Diesel spray in an engine environment by multi-time-step imaging. Further necessities were a high pulse-to-pulse amplitude stability, and a high beam quality. The laser is optimized to generate pulse bursts with a total duration no longer than 300 µs. Therefore, quasi-continuous diode lasers can be used for as pumping source, which strongly reduces thermal requirements and costs. It was decided to use the $^4F_{3/2} - {}^4I_{13/2}$ laser transition of the Neodymium ion, that provides an emission wavelength of ~1340 nm. By second harmonic generation this wavelength can be converted to 671 nm – a wavelength were Diesel becomes adequately transparent.

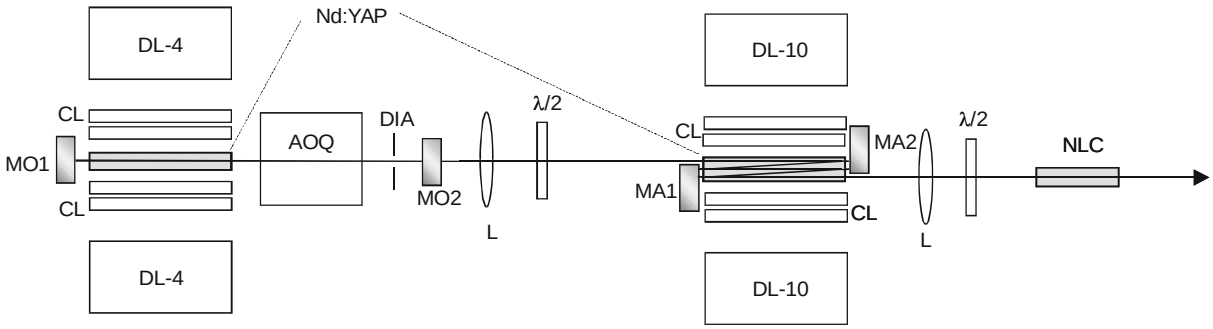

Fig. 4.21 Set-up of the laser system. MO1,2: mirrors of oscillator; MA1,2: mirrors of amplifier; DL-4,-10: qcw diode laser stacks of oscillator and amplifier (resp.); CL: cylindrical lenses; AOQ: acousto-optical Q-switch; DIA: diaphragm; L: lens; λ/2: retardation plate; NLC: nonlinear crystal

The laser configuration consists of an acousto-optically Q-switched oscillator and a five-pass amplifier (Fig. 4.21), each of which is transversally pumped by two quasi-cw AlGaAs-diode laser stacks, providing maximum pump powers of 2×400 W (2×4 linear array bars) for the oscillator, and 2×1 kW (2×10 linear array bars) for the amplifier at an emission wavelength of about 810 nm. The diode stacks are micro-channel cooled, and they can be operated up to a maximum duty cycle of 30%. Each of the linear array bars is equipped with an aspherical cylindrical microlens that collimates the fast axis of the diode laser beam. The pump radiation emitted by the diode laser stacks is focused by a pair of cylindrical lenses into the crystals of the oscillator and the amplifier, generating a nearly 500 µm thick horizontal layer of inversion in the center planes of the crystals.

The active material selected for the laser is Nd:$YAlO_3$ (Nd:YAP). This crystal is characterized by a large laser cross-section of 1.2×10^{-19}cm^2 at an emission wavelength of 1341 nm, a naturally polarized radiation, and high optical and mechanical quality. The crystals have a length of 20 mm and a quadratic cross section of 3×3 mm^2 (oscillator) and 5×5 mm^2 (amplifier). The end faces are anti-reflection coated at a wavelength of 1341 nm, and additionally at 1079 nm, in order to prevent lasing at this transition which has a nearly three times larger laser cross-section. Furthermore, the lateral faces have triple AR coatings at 810 nm, 1079 nm and 1341 nm, to increase the transmission of the pump radiation and to prevent parasitic lasing due to these surfaces.

The stable resonator of the laser oscillator is formed by a flat, highly-reflecting mirror and a concave outcoupling mirror with a 1 m radius of curvature and a transmission of 30% at the laser wavelength. The resonator length is 110 mm. A diaphragm inside the laser resonator is used to achieve TEM_{00} laser operation. An electronic circuit generates the delay and the steering pulses for the acousto-optical Q-switch, by which stable laser pulse bursts are produced with uniform, equal amplitudes during a pumping period of 250 µs (Fig. 4.22).

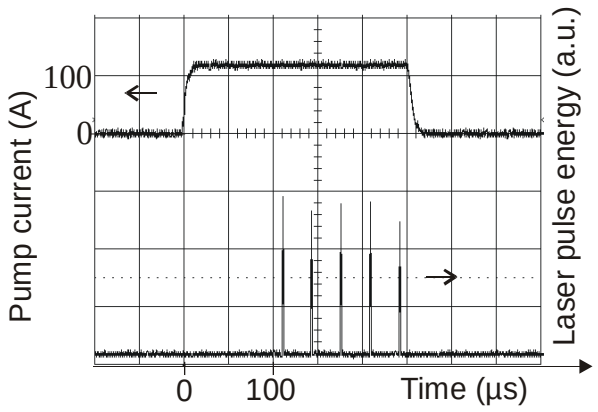

Fig. 4.22 Oscilloscope traces of pump current (top part) and pulse burst (bottom part). Time scale: 50 µs per unit. Differences of the amplitudes are due to the oscilloscope resolution.

Under operating conditions with pulse-to-pulse intervals of 33 µs the energy of a single pulse is 0.44 mJ, while the pulse width is 30 ns. For optimum coupling of the oscillator beam to the amplifier an $f = 500$ mm lens and a $\lambda/2$ retardation plate are used. A five-fold path in the amplifier crystal is generated by means of two plane mirrors. These elements had to be adjusted very carefully in order to achieve reflection of the laser beam within a planar layer for optimum matching to the pump beams, and simultaneously to suppress parasitic lasing.

At a maximum pump current of 110 A an amplification of nearly a factor of ten was achieved which resulted in an energy for a single pulse of 4.4 mJ (Fig. 4.23).

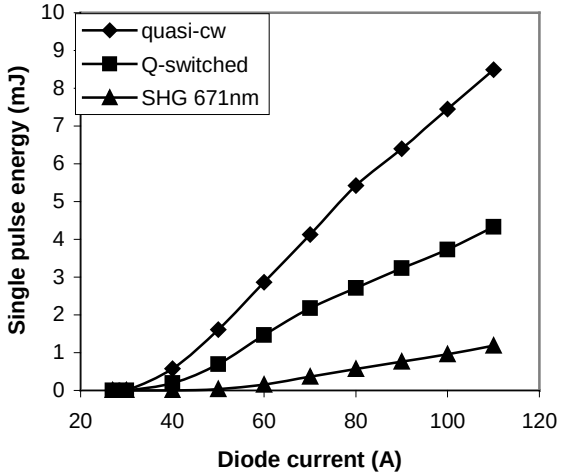

Fig. 4.23 Energy of a single pulse of the pulse train as a function of the current driving the diode laser stacks of the oscillator and of the amplifier.

A beam quality factor M^2 of 1.2 was measured, which represents an optimum prerequisite to achieve high conversion efficiency in the subsequent frequency doubling process. The amplified laser beam is focused into a 10 mm long KTP crystal, which is

anti-reflection coated at 1341 nm and 671 nm. By using an f = 250 mm lens and a $\lambda/2$ retardation plate a maximum pulse energy of up to 1.3 mJ is generated at a wavelength of 671 nm. Due to the phase-matching properties of the nonlinear crystal the red output beam has a slight ellipticity of about 1:2.5, which is advantageous with respect to generating a light sheet for the imaging experiments.

4.4.2 Detection systems

For the two-dimensional imaging of spray processes several different camera systems were used in this work.

4.4.2.1 CCD cameras

"CCD" stands for "charge-coupled device", meaning a two-dimensional semi-conductor detector array where incoming photons generate electron-hole pairs due to the photoelectric effect and therefore allowing quantitative measurement of light intensities. By application of a voltage to the implemented electrodes, charge barriers are being generated that cause the electrons to accumulate in small spatial regions (pixels). The accumulated charge is considered to be proportional to the incident light intensity. However, there is a maximum charge each pixel can hold. If the maximum intensity is exceeded, the additional charges overflow to the adjacent pixels, causing image blooming.

After the exposure the accumulated charges are transported to an amplifier by a shift register where the charge is being shifted from pixel to pixel by consecutive lowering of the potential barriers in each line of the sensor. A central amplifier generates an analog signal, proportional to the accumulated charge for each pixel. This signal is converted to digital data by a analog-digital converter and can be further processed.

In order to avoid thermal production of electron-hole pairs that would cause a temperature-dependent noise level, the CCD chip is thermostatically cooled.

4.4.2.2 CMOS cameras

An active pixel sensor (APS) is an image sensor consisting of an integrated circuit containing an array of pixels, each containing a photodetector as well as three or more transistors. Because it can be produced by an ordinary CMOS (complementary metal-oxide semiconductor)[1] process and is hence also known as the CMOS sensor, APS is emerging as an inexpensive alternative to CCDs.

---

[1] Complementary metal-oxide semiconductor (CMOS) is a major class of integrated circuits. Since around 1998 CMOS technology has also been used for a wide variety of analog circuits such as image sensors, Data Converters, and highly integrated Transceivers for many types of communication. CMOS is also sometimes explained as *complementary symmetry metal-oxide semiconductor*. The words "complementary-symmetry" refer to the fact that the design uses complementary and symmetrical pairs of p-type and n-type MOSFET transistors for logic functions.

CMOS sensors also rely on the inner photoelectric effect for the detection of light intensities. In contrast to the before-mentioned CCD chip a CMOS sensor does not transport the accumulated charges of each pixel to one single amplifier. Instead each pixel has its own amplifier that converts the charge to an analog signal that is directly given to the analog-digital converter. A CMOS sensor consists, in addition to the photosensitive part, of a multitude of transistors that generate the signal, the overall light sensitive area of the detector is severely reduced compared to a CCD sensor. This problem was overcome in recent years by the application of micro lenses.

The main advantage of CMOS cameras consists in the flexibility of the signal readout, the possibility of high repetition rates and the avoidance of blooming effects. The disadvantage is the low sensitivity compared to a standard CCD.

4.4.2.3 Image Intensification

For the detection of weak signals, as often encountered in tracer-LIF where the concentrations of the fluorescent marker are low, narrow spectral filters are applied and short exposure times are needed, the sensitivity of a CCD or CMOS detector is not high enough and amplification of the incoming photons becomes necessary. The working principle of an image intensifier is illustrated in Fig. 4.24. The incoming light is focused on the input window which consists of cathode that converts the photons into electrons by virtue of the photoelectric effect. In the intensified cameras used in this work the cathodes were typically sensitive from 190 to 900 nm with a maximum sensitivity around 400 nm. During the exposure time, the potential of the photo cathode is switched from +50 to –180 V so that photoelectrons can reach the MCP only during this time gate. An MCP ("micro channel plate") is an electron multiplier. It consists of a thin glass plate (0.5 mm) with a large number of parallel channels. The diameter of the channels is typically 10 µm for standard tubes and 6 µm for high resolution tubes.

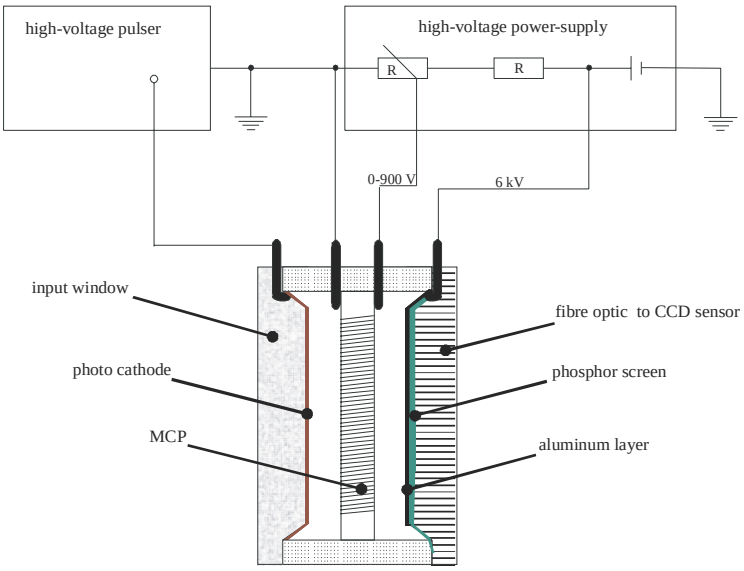

Fig. 4.24 Image intensifier: The photo electrons are accelerated towards the micro channel plate (MCP) where they are multiplied and accelerated in a second stage onto the phosphor screen where they are transformed into photons again. Via fiber optics these photons are directed to the CCD sensor (from [80], LaVision)

A 25 mm diameter MCP contains approximately 1.5 million channels, which are set at a small angle to the major axis of the MCP. This increases the probability of electrons to collide with the channel walls. Every electron entering a channel in the MCP collides with the channel wall and produces secondary electrons. These electrons are accelerated through the channel by means of the high potential gradient applied to the MCP and by further collision with the channel wall, produce further secondary electrons at each collision. The result of these repeated collisions is an electron gain up to 10^3. The l/d parameter (length /diameter) of the channels determines the maximum gain. A typical value is $l/d = 40$.

The output window consists of a glass or fiber optical base, covered by the luminescent phosphor. The phosphor is covered by an aluminum surface which acts as a mirror in both directions. This guarantees a low transparency of the image intensifier and reflects both, the emitted light of the phosphor into the direction of the exit plane and the residual light from the entrance surface that passed through the photo cathode and the MCP.

Various phosphors can be used. They differ in their luminescence color, efficiency, decay times and grain size. The electron-to-light conversion at the phosphor is realized by impact of the accelerated electrons. After leaving the MCP the electron cloud is pulled by a voltage of 5 – 6 kV onto the phosphor. At $U = 6$ kV for each electron ca. 60 photons are generated at a P46 phosphor. Due to the light-to-electron conversion (at the photo cathode) and re-conversion (at the phosphor) the color information of the original image is lost (i.e. the light shows the green phosphor color). The intensity maximum of the described phosphors is in the green color region, where the CCD shows a sensitivity maximum. Different types of phosphors are being used within image intensifiers. The

selection depends on the phosphor emission color, its efficiency and in the phosphor decay time. The table below shows some typical data [81].

Phosphor type	Color	Relative Efficiency	Decay time
P20	Green	1	~50 ms
P43	Green	0.9	~1 ms
P46	Green	0.3	~1 µs
P47	Blue	0.25	~100 ns

Tab. 4.1: Different phosphor types and their properties

Usually P43 phosphors are used. These provide highest efficiency in combination with a reasonably short decay times. For the *LaVision Streak Star* camera used in this work a phosphor with a short decay time is needed (P46) because of the high temporal resolution (30 µs). The lower efficiency can be compensated by a booster tube. The StreakStar camera uses an *inverter tube* as booster. It mainly consists of two elements: a photo cathode, and a phosphor without MCP. In the vacuum in between the electrons are accelerated. The tube is externally supplied with a DC voltage of 24 V. High voltage modules inside the tube potting generate a steady high voltage field. Light amplification is achieved in two ways:

- Generated electrons are accelerated to energies around 15 kV. With P46 phosphors the typical light amplification is 7:1 (for green light).
- The demagnification of 25 mm down to 18 mm gives an additional intensity enhancement of $(25/18)^2 \approx 2$.

The output window may be a glass window or a fiber-optical window. The latter allows fiber-optical coupling to additional intensifiers (boosters) and the CCD chip. By fiber optical coupling the most efficient light transmission from the image intensifier to the CCD can be realized. The efficiency of lens coupling strongly depends on the demagnification factor and on the *f#* of the lenses used, but in any case the fiber coupling is at least two times more efficient.

The two-stage conversion of photons to electrons and back to photons leads to a certain deterioration of the spatial resolution of the image, even for the best image intensifier. In addition the booster causes a geometrical distortion of the image which must be corrected for.

4.4.2.4 Image processing

Images of LIF or scattered light or any kind of signal from the area of interest contain quantitative information that needs to be extracted by digital image processing. The first step usually is to correct the image for background signal and for geometric distortion. In this work several experiments are presented that make use of two simultaneously-

recorded images from two different cameras. In this case the thorough correction of spatial distortions and mapping of the images are important.

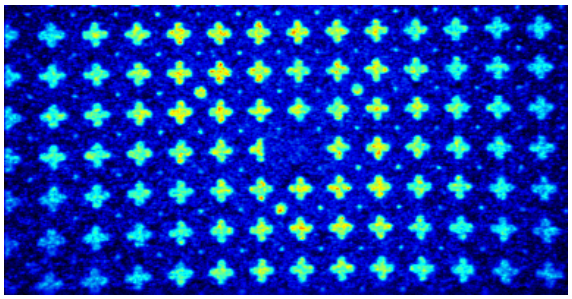

Fig. 4.25 Uncorrected image of a calibration plate taken with a Streak Star camera (LaVision). The pincushion distortion caused by the two-stage image intensifier is clearly visible.

In this work the imaging processing software *DaVis* from *LaVision* was used [82]. It utilizes a distortion correction algorithm based on the following relations.

$$\begin{aligned} x &= x' + dx(s,t) \\ y &= y' + dy(s,t) \end{aligned} \tag{4.34}$$

where x, y are the coordinates of the undistorted image, x' and y' the coordinates of the distorted image, dx and dy are the distortion functions. the distortion functions are calculated using intermediate coordinates s and t

$$\begin{aligned} s(x') &= 2(x' - x_0)/nx \\ t(x') &= 2(y' - y_0)/ny \end{aligned} \tag{4.35}$$

where nx and ny are the numbers of pixels in each row and column respectively. (x_0,y_0) is the user-defined point of origin. The distortion functions are approximated with polynomials of third degree in s and t (equivalent to x' and y') with 20 coefficients. These coefficients are calculated for each camera from the image of an calibration plate (see Fig. 4.25). The number of cross marks on the calibration plate and the contrast are important for the accuracy of the method. At least 40 marks should be clearly visible to provide good correction. Fig. 4.26 shows a typical calculation of the correction coefficients for images taken with a Streak Star 3 camera (*LaVision*).

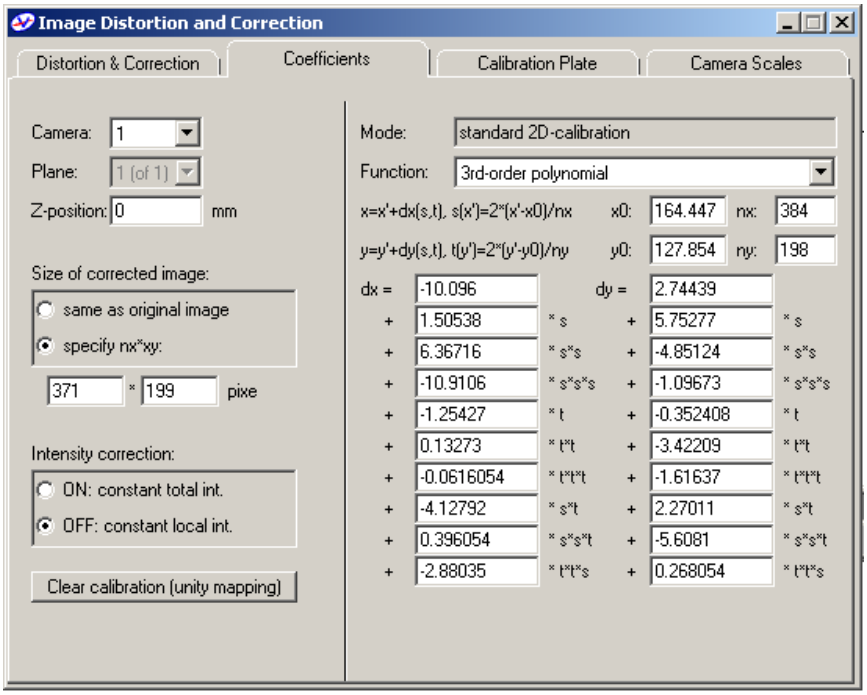

Fig. 4.26 Coefficients for the image correction in DaVis 6.3. The calibration plate in Fig. 4.25 was used to determine the coefficients.

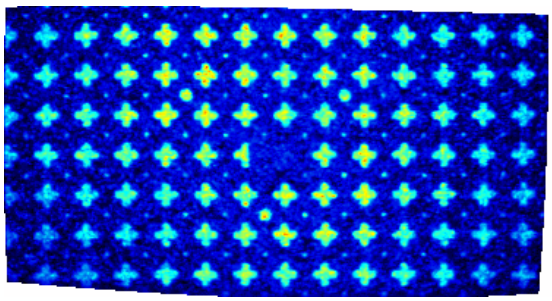

Fig. 4.27 Corrected version of the image shown in Fig. 4.25. The pincushion distortion is gone.

By thorough application of this method, accuracies of less than one pixel can be achieved. This accuracy is necessary when two images showing small structures like droplets in a spray need to be overlaid.

5 Experiments

In this work the various discussed laser-optical methods of spray diagnostics have been applied and evaluated in several spray systems. Reaching from technically most relevant applications like fuel injection sprays in engines over model sprays to single droplets. The objective was not only to analyze the involved sprays in terms of better understanding of the underlying processes and the possibility for optimization but also to further evaluate the applied measurement techniques and show their strengths and limitations. For these purposes comparison with simulations is needed. On the other hand, the measured properties are used as input for newly developed numerical models.

5.1 Experiments in engine-like environments

The combustion stability of engines is mainly determined by the quality of the in-cylinder mixing of liquid fuel and air. Modern engine concepts (DISI) make use of the possibility to form a variable mixture by injecting liquid fuel directly into the combustion chamber. The resulting stratification of the fuel allows unthrottled operation of the engine with the benefit of a noticeable reduction in overall fuel consumption. However, direct injection engines still suffer from ignition instabilities. Therefore, experimental investigation of the spray formation, mixture formation and evaporation processes are necessary for further improvement. The major challenge for experiments is the multi-phase character of the system where variables like pressure temperature, flow velocity, liquid and vapor fuel concentration constantly interact.

Experiments require optical access to the combustion chamber. For this purpose so-called optical engines are built that contain several windows in the cylinder and the piston. This allows laser-optical spray diagnostics under realistic reactive conditions. The short time scales of in-cylinder processes (typical injection durations ~ 0.4 – 1.3 ms) require high repetition rate imaging systems.

Engine environments pose several challenges to optical diagnostics:

- highly turbulent reactive environment with complex interactions between spray and air flow
- gasoline and Diesel fuels show fluorescence that can interfere with tracer fluorescence and is hard to quantify
- present oxygen may influence the fluorescence properties of tracers (quenching)

Therefore, it can be easier and more insightful to study spray processes in a more controlled environment like a spray chamber or to use single component model fuels.

The following section will cover three different approaches. First the spray structure and interaction with the combustion chamber will be discussed in an engine experiment

using a firing optical engine. Thereafter, the so-called LIEF measurement method for simultaneous measurement of liquid and vaporized fuel will be discussed and applied to a non-reactive fuel spray in a controlled spray chamber, using conventional fuel injectors. The last section will discuss a method for the application of tracer LIF in real Diesel fuels.

5.1.1 Spark-Spray-Interaction

In modern direct injection gasoline engines ignition stability is still a problem. The close spacing of the injector and spark electrodes can lead to high gas-phase and liquid-phase velocities, large numbers of liquid droplets, and steep, rapidly-varying gradients in velocity and fuel-air ratio, all of which can be unfavorable to robust ignition and flame-kernel growth. Occasional random misfires are typically encountered, especially as the charge is diluted to reduce the flame temperature and hence NO production.

In the literature one can find combined experiments and numerical simulations to examine fuel sprays, mixture preparation and combustion in a SG-DISI engine [1,11]. These studies found that, over a substantial range of injection and spark-timing conditions, multi-cycle ensemble averages of key experimental quantities – specifically, spray structure, fuel concentration near the spark gap, combustion (both the initial partially premixed flame propagation and the later mixing-limited combustion of rich products) and the overall heat-release rate – were adequately captured by computational fluid dynamics (CFD) calculations employing k-ε turbulence and two-stage combustion sub-models. Although such CFD codes predict the intensity of velocity fluctuations (via the turbulence kinetic energy), they typically do not directly calculate fluctuations in fuel concentration, which are important to cyclic variation in engine performance through their influence on ignition and combustion stability. As illustrated in Fig. 2.1, the cyclic variations in fuel-concentration can be very large in SG-DISI engines.

This work quantifies fluctuations associated with the fuel spray itself, the spray–spark-plug interaction, and their effect on the spark as potential sources of misfires and unstable combustion in a SG-DISI engine.

5.1.1.1 Apparatus and Techniques

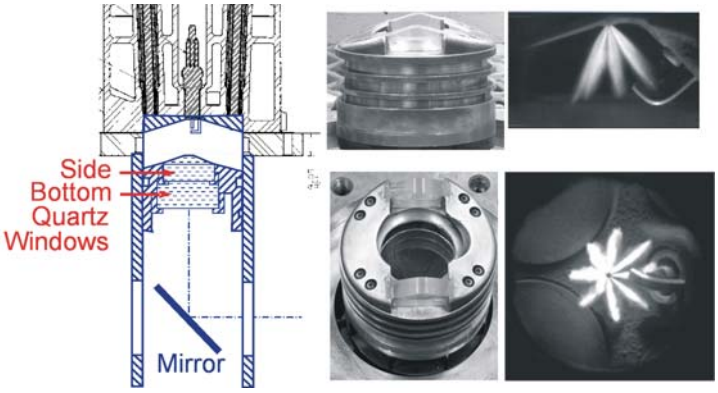

Fig. 5.1. Left: Schematic of optical SG-DISI engine. Center: Photographs of piston. Right: Views of fuel spray through piston side and bottom windows.

Fig. 5.1 shows a schematic diagram of the four-valve, single-cylinder optical SG-DISI located engine (86 x 86 mm bore x stroke; 9.7 compression ratio) at the General Motors Research & Development Center, Warren that was used for the experiments. The piston had a centered, cylindrical combustion bowl whose bottom was formed by a flat quartz window. Flat quartz side windows permitted a view of the spark plug, even at the highest piston position (Top-Dead Center, TDC). A water-cooled pressure transducer measured the cylinder pressure. For many experiments, the spark current and voltage were also digitized at a rate of 500 kHz.

All the experiments reported here were performed at conditions corresponding to a part-load cruise for a mid-size vehicle equipped with a four-cylinder naturally aspirated engine: an engine speed of 2000 RPM, a manifold absolute pressure (MAP) of 95 kPa, and 10 mg gasoline fuel injected per cycle, producing an air-fuel ratio of approximately 50:1 without dilution.

Most of the experiments used a multi-hole injector operated at an injection pressure of 11 MPa. The injector produced eight spray plumes in an axisymmetric pattern, with a nominal angle of 70° between opposite plumes. Extended-electrode spark plugs (a J-gap plug and a special pointed-electrode plug) were used with the 70° injector (see Fig. 5.1). To simulate exhaust-gas recirculation (EGR), the intake charge was diluted with nitrogen, typically to a level of 30%. Note that for continuous firing, this produces an oxygen concentration in the cylinder equivalent to approximately 42% EGR. For this dilution, the optimal end-of-injection (EOI) command timing and spark-advance (SA) timing were EOI = 48°BTDC and SA = 40°BTDC.

Fig. 5.1 shows typical spray images (70° injector, extended-electrode J-gap spark plug) recorded with floodlight illumination. Mie-scattering images were also acquired with volume and light-sheet illumination through the piston window by a copper-vapor laser (*Oxford Lasers LS-20*, 30 ns pulse duration, 2 mJ/pulse, wavelengths 511 and 577 nm)

synchronized to a high-speed intensified CCD camera. Three high-speed cameras were used at different stages of the experiments: a monochrome Kodak 4540 (8-bit- dynamic range, typically operated at 9000 frames/s to produce a 256 x 128 pixel image); a Photron Fastcam Spectra (same speed, dynamic range and spatial resolution as the Kodak 4540, but providing simultaneous images at three wavelengths determined by dichroic beamsplitters and narrowband filters [1]); and a Phantom 7.1 monochrome camera (12-bit dynamic range, operated here at 368 x 360 pixels at 12000 frames/s or 128 x 144 pixels at 60000 frames/s).

5.1.1.2 Spray fluctuations

Fig. 5.2 presents a sequence of high-resolution (10 µm/pixel), high-speed (9000 frames/s) Mie-scattering images of the spray obtained with the Kodak 4540 camera, a K2 long-distance microscope, and laser-light-sheet illumination along the injector axis. The engine was fired continuously with 30% nitrogen dilution and with the optimal EOI=48°BTDC and SA=40°BTDC timings. To highlight the fluctuations, individual-cycle images, shown in red, are overlaid on 100-cycle ensemble-average images (green) at the same crank angle, so that a spray image would appear yellow throughout if the individual-cycle and ensemble-average images agreed perfectly.

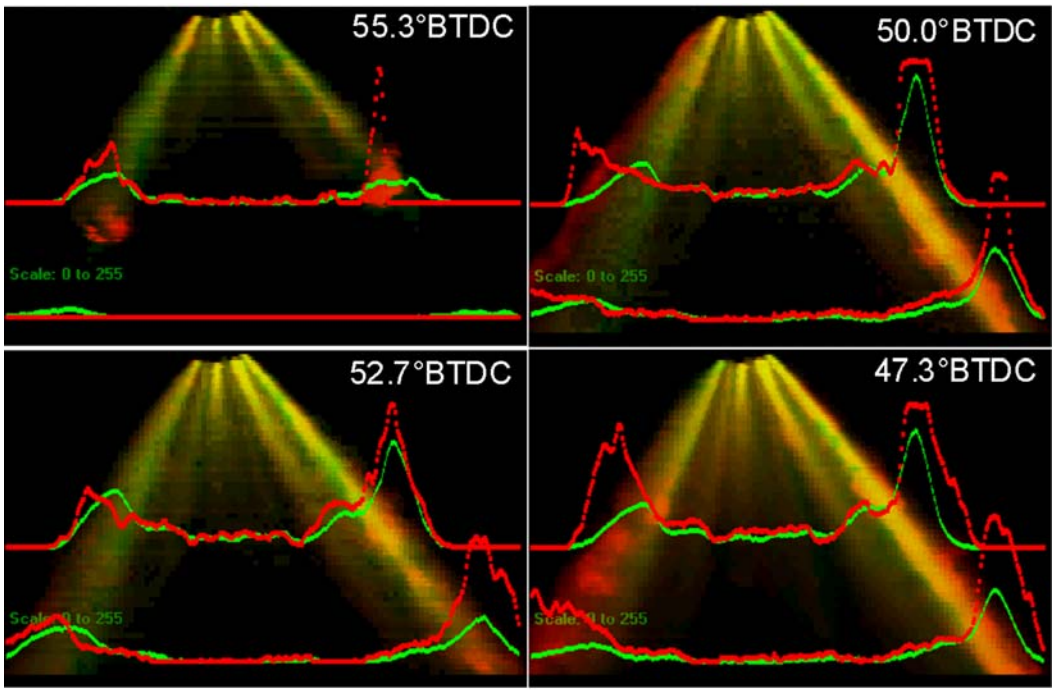

Fig. 5.2 Selected high-resolution Mie-scattering images of the fuel spray from one engine cycle (red) overlaid on corresponding images of the ensemble average of 100 continuously fired cycles at the same crank angles (green). Mie-scattering intensities along lines perpendicular to the cylinder axis are plotted at two distances from the injector. The field of view is 9 mm high.

Near the injector exit, all the spray plumes are within the laser sheet. For the individual engine cycle in Fig. 5.2, both the leftmost and rightmost spray plumes make larger angles with the cylinder axis than for the 100-cycle ensemble average. Variations in

these angles within individual cycles as well as from cycle to cycle have been observed. The individual-cycle images also show significant non-uniformities in the Mie-scattering intensity on the scale of 1–2 mm (comparable to the 1.5-mm spark gap).

Because the spark gap was located only a few mm downstream of the lower right corner of the images, variations in spray angle [83] and liquid distribution must be considered as potential sources of misfires and partial burns.

5.1.1.3 Fluctuations in spray angle

The left and right spray plume angles in Fig. 5.4 were evaluated from a Mie-scattering intensity trace taken approximately midway between the two traces shown in Fig. 5.2. The locations of the opposite spray plumes d_l and d_r relative to the center line was identified from the peaks in the Mie intensity profile (see Fig. 5.3).

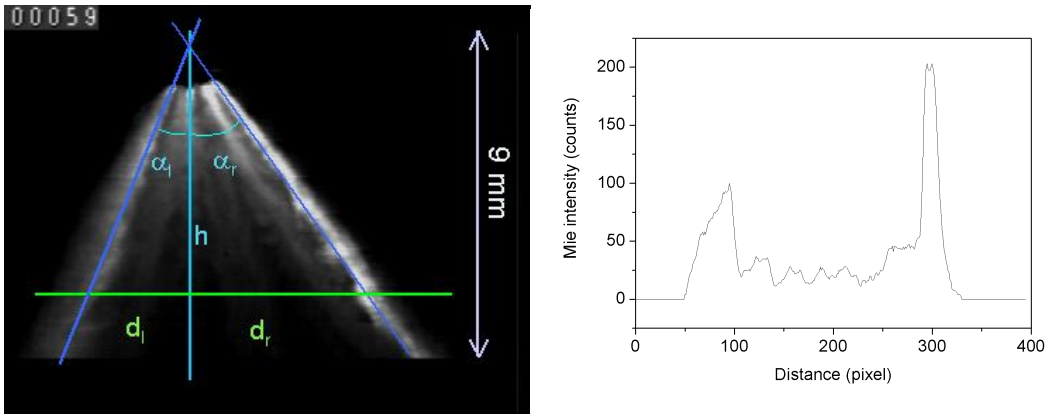

Fig. 5.3 Determination of the spray angle from Mie scattering images of the fuel spray. Left: Spray image at 50°CA, right: Mie intensity profile.

Thus, the left and right spray angle were determined for one hundred consecutive engine cycles. A histogram of the results is shown in Fig. 5.4 (upper image).

For the right plume – the plume nearest the spark gap – the cycle-to-cycle variation in spray angle with respect to the cylinder axis is no more than a few degrees, and the individual-cycle spray-angle variations are uncorrelated with individual-cycle combustion stability (Fig. 5.4 lower image). The nitrogen dilution was increased here to 37.5% in order to increase the sensitivity of ignition to the local fuel distribution.

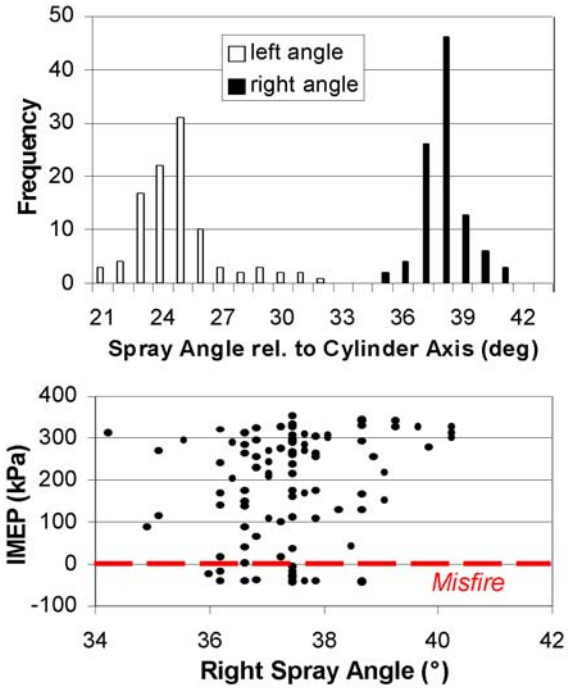

Fig. 5.4 Cyclic fluctuations in spray plume angle. Upper: Histograms of left and right spray-plume angles relative to the cylinder axis. The injector axis is inclined 11° with respect to the cylinder axis. Lower: Individual-cycle results for IMEP vs. angle of spray plume nearest the spark gap.

In addition the variation of the spray angle within one cycle was studied for different settings of the in-cylinder swirl. The results of a forty cycle average is shown in Fig. 5.5. The angles have not been calculated separately, instead the distance between the peaks is used as a measure for the overall spray angle. The large error bars are again evidence for the large cycle-to-cycle variability of the spray angle for both conditions. Nonetheless the trend shows a more stable and slightly larger spray angle for a high intake swirl compared to an obvious decrease in spray angel for low swirl. Altogether the low swirl condition showed a slightly higher ignition stability.

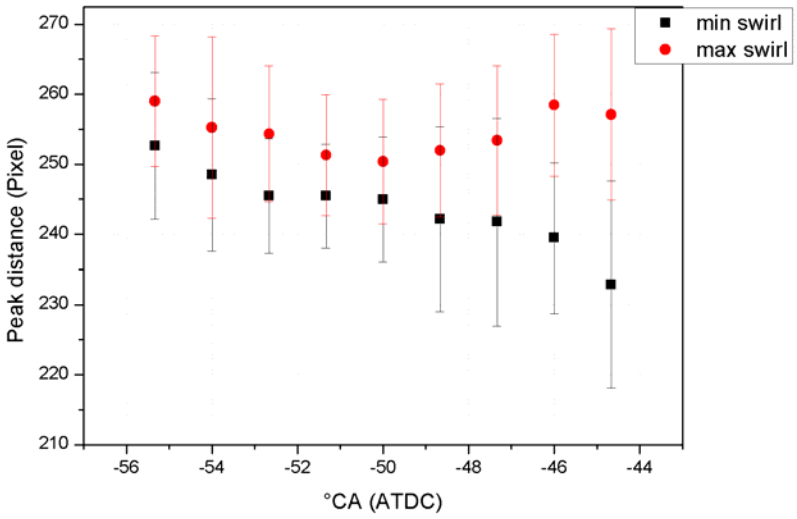

Fig. 5.5 In-cylinder variation of the spray angle (measured by the distance between left and right spray peak) for minimum and maximum swirl settings of the engine

5.1.1.4 Fluctuations in liquid distribution

For an ensemble of droplets of the size typically produced by high-pressure gasoline injectors (Sauter mean diameter ~15 μm), the Mie-scattering intensity is proportional to total droplet surface area. Here, this has been used to characterize cycle-to-cycle fluctuations in the liquid-fuel distribution by spatially integrating the Mie-scattering intensity either along a spray plume (Fig. 5.6, left) or in small regions (Fig. 5.6, right) whose scale (1.5 mm) is the same as the spark gap width. The examples in Fig. 5.6 are for crank angle 48.7°BTDC; although this is just before the end-of-injection command, the injector does not actually close for about another five degrees.

The results in Fig. 5.6 show that the liquid-surface-area fluctuations in region 2 (normalized by the ensemble-average) are significantly larger than the fluctuations along the spray plume. Similar results were obtained over the course of the injection event along the spray plume and for all three measurement boxes in Fig. 5.6.

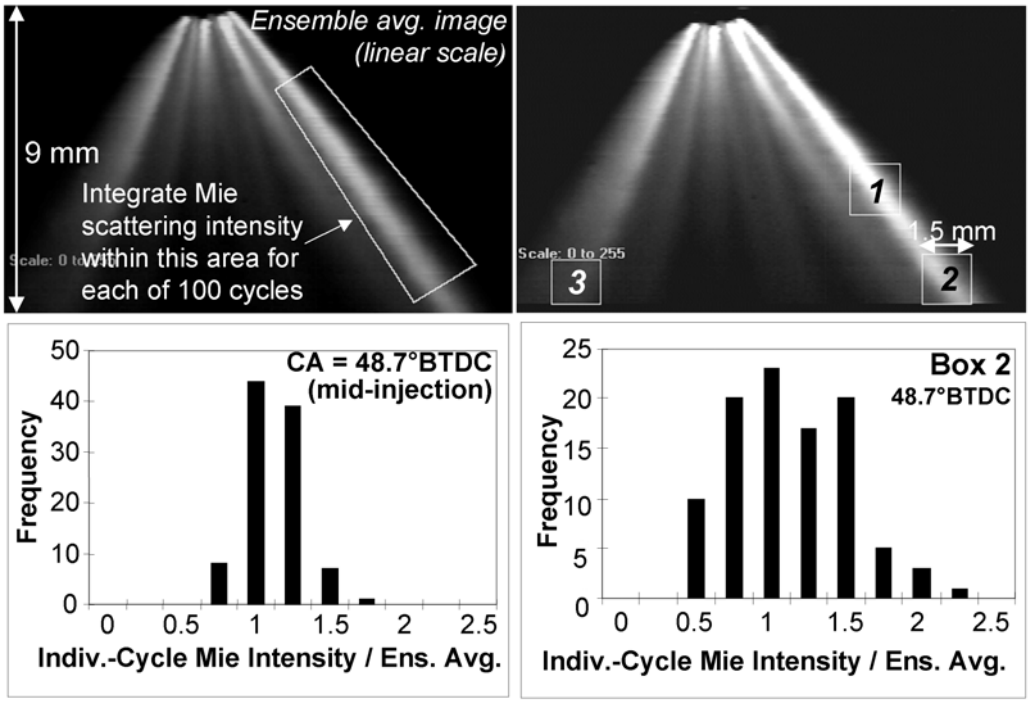

Fig. 5.6 Cycle-to-cycle fluctuations in liquid distribution as measured by integrated Mie scattering intensity along a spray plume (left) and in a small region a few mm upstream of the spark gap (right).

Fig. 5.7 shows the results of a similar analysis for a 1.5-mm region (C) near the tip of the spark plug at crank angle 42°BTDC, i.e., 2° before ignition. At this time, the injector has closed, and there is much less liquid near the spark plug; the ensemble-average Mie-scattering image in the upper part of the figure is therefore shown on a logarithmic intensity scale. The inset sketches how the laser light sheet passed between the pointed electrodes. The range of fluctuations in the local droplet surface area (Fig. 5.7, lower) in region C at this time is similar to that for the small region 2 upstream of the spark gap in Fig. 5.6 earlier in the injection event. A similar fluctuation range is also found in regions A (upstream of the gap) and B (in the wake of the electrodes) of Fig. 5.6 just before ignition. Thus, just before the optimal ignition timing, the liquid surface area near the spark gap can vary over a range of about a factor of four from cycle to cycle.

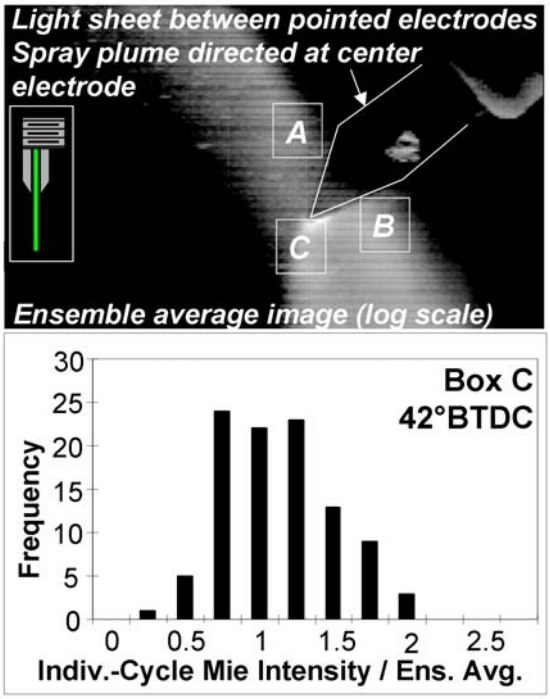

Fig. 5.7 Cycle-to-cycle fluctuations in liquid distribution at tip of pointed-electrode spark plug shortly before ignition.

5.1.1.5 Effects of injector and electrode orientation

In the foregoing examples, one spray plume was always aimed directly at the center electrode of the spark plug (see Fig. 5.1, lower right), whether a conventional J-gap or a special pointed-electrode geometry was used. Fig. 5.8 shows the effect of spray-plume targeting on the vapor-phase and (relative) liquid-phase fuel concentrations at the gap of the pointed-electrode spark plug as measured by high-speed spectrally resolved imaging of CN* and C_2* spark emission, respectively[11,84,85]. The right-hand bars are for gasoline fuel with one plume impacting the center electrode while the center (gasoline) and left-hand (isooctane) bars are for the injector rotated so that two spray plumes straddled the center electrode. The absence of detectable liquid fuel at the spark gap with isooctane (a single-component fuel with normal boiling point of 99°C) highlights the role of the less volatile constituents in multicomponent gasoline. Despite the large differences in the ensemble-average vapor and liquid fuel concentrations, there was scarcely any difference in ignition stability. Furthermore, the J-gap plug could be rotated up to ±90° from the orientation shown in Fig. 5.1 without significantly affecting performance.

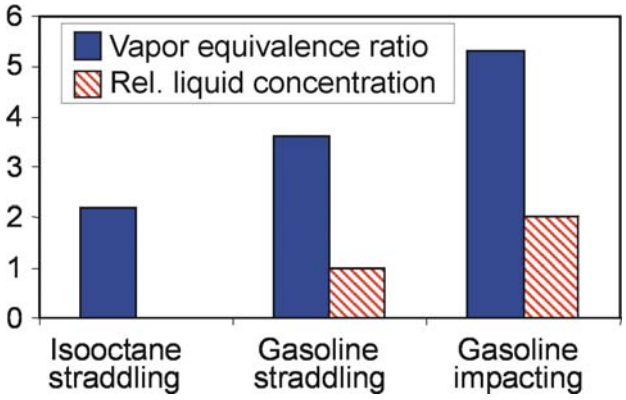

Fig. 5.8 Vapor-phase fuel concentration (expressed as fuel-air equivalence ratio assuming uniform distributions of air and diluent in the cylinder) and relative liquid fuel concentration for two fuels and for spray-plume targeting with respect to spark-plug center electrode.

Larger changes in spark-plug orientation caused the spray to interact strongly with the J-gap ground electrode and degraded ignition stability. Fig. 5.9 shows the extreme case in which the spray plume strikes the ground electrode head-on. Although the ground electrode shields the spark gap from the spray plume and reduces the local velocity at the time of spark, the resulting wake causes strong fluctuations, leading to significantly increased misfire rates.

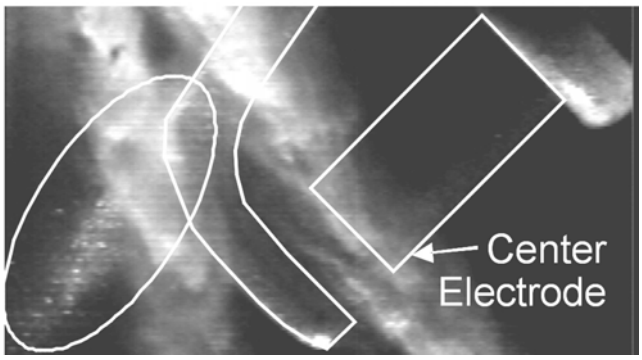

Fig. 5.9 Extreme example of spray/spark-plug interaction in firing SG-DISI engine imaged using volume illumination from a copper-vapor laser. In this orientation, the spark plug ground electrode faces the approaching spray. One spray plume strikes the ground electrode and produces a stream of large droplets (marked by the ellipse).

5.1.1.6 Spark stretching and restrikes

SG-DISI engines typically employ a high-energy inductive ignition system (e.g., approximately 120 mJ spark energy, as in this work). As illustrated by the 60000-frame/s images in Fig. 5.10 (see also [86]), the ignition event is then definitely *not* a nearly instantaneous, point process, as one might naïvely expect. The overall spark duration here is about 2 ms, or 24° crank angle at the 2000 RPM engine speed. The spark is highly distorted and stretched out of the gap to distances of at least a few mm. The glowing fireballs as well as the more diffuse light extending from the bright spark represent predominantly thermal emission from locally rich combustion ignited by the

spark. (The broadband visible-wavelength images here do not show ultraviolet OH* chemiluminescence from partially premixed stoichiometric or lean combustion.)

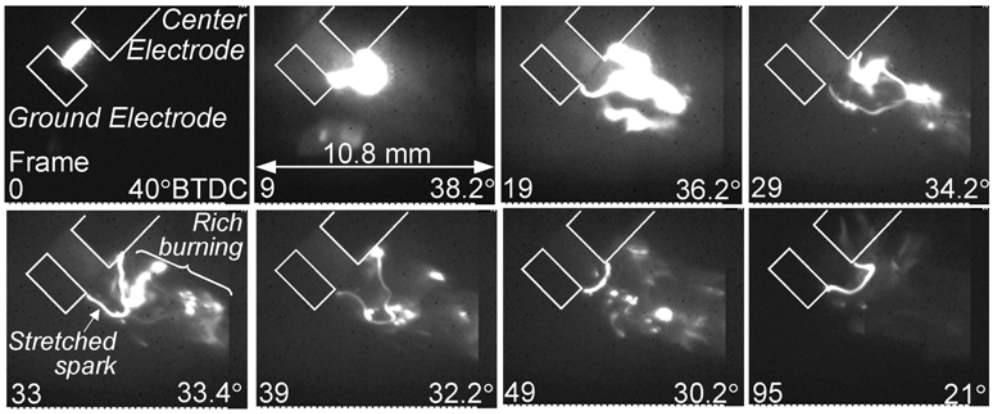

Fig. 5.10 Broadband visible-wavelength (400 – 800 nm) images of ignition in a spray-guided DISI engine selected from a sequence recorded at 60000 frames/second with 7.5-µm/pixel spatial resolution. The spark-plug electrodes (overlaid in white) are oriented so that the camera looks directly into the opening of the J-gap. A spray plume from the multi-hole injector approaches the spark plug from the upper left.

Spark voltage and current measurements can provide useful information, especially when combined with high-speed imaging [86]. Fig. 5.11 shows relatively slow spark stretching for non-injected (premixed-charge) operation with the pointed-electrode spark plug. As the spark is stretched, its electrical resistance and the voltage drop across the spark increase until eventually the available coil voltage can no longer sustain the spark. Unless this occurs when the coil is almost fully discharged, there will usually be enough energy left to cause another breakdown, i.e., a restrike, sometimes directly across the spark gap (e.g., between frames 39 and 49 of Fig. 5.10 and at 1.19 ms in Fig. 5.11) and sometimes into the existing ionization channel, which can be seen to persist in Fig. 5.11 even though in this case the restrike occurred across the gap.

In contrast, Fig. 5.12 shows similar results selected from a dataset of 1000 continuously fired cycles recorded during direct-injection stratified-charge operation (EOI = 48°BTDC, SA = 40°BTDC). The strong spray-induced motion here leads to locally higher velocities and more rapid spark stretching, as shown by the steeper slope of the spark voltage curve around 0.5 ms Furthermore, from 0.8 ms to the end of the spark discharge at 1.4 ms (indicated by the return of the spark current to zero), the voltage trace shows a series of very rapid restrikes. This occurs when the spray interacts very strongly with the spark, producing such high local velocities and such rapid stretching that the available voltage cannot sustain the spark for more than a few tens of microseconds. This rapid restriking also shortens the spark duration (≅1.3 ms here compared to ≅2.4 ms in the non-injected example of Fig. 5.11).

The cycle-to-cycle variability in the spark current and voltage traces and in the spark images is large, but no straightforward correlation of these features (e.g., spark energy or frequency of restrikes) with misfires or partial burns has emerged in this work.

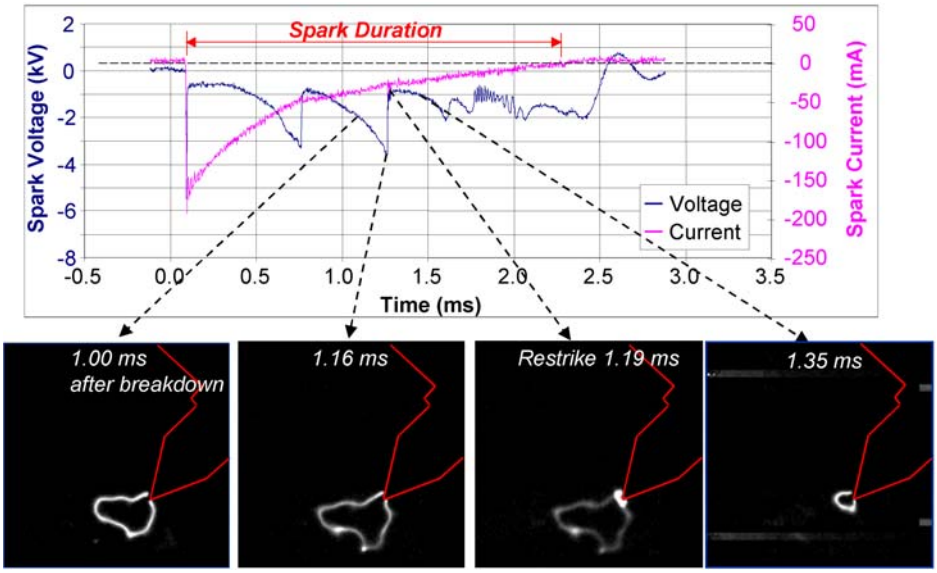

Fig. 5.11 Spark voltage and current traces together with images from a 60000-frame/s sequence selected to illustrate spark stretching and a restrike during premixed-charge (non-injected) operation.

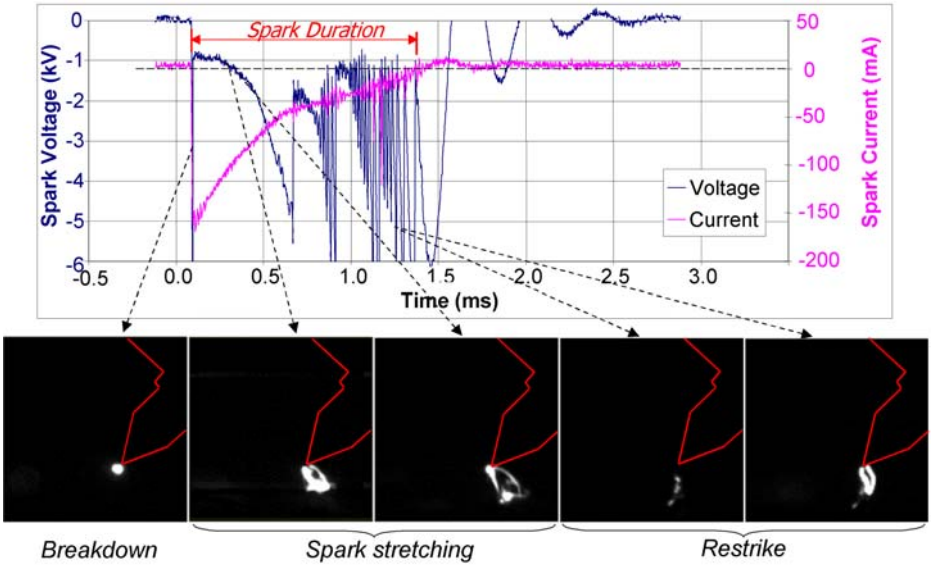

Fig. 5.12 Spark voltage and current traces and selected high-speed images during direct-injection operation.

The cycle-to-cycle variability in the spark current and voltage traces and in the spark images is large, but no straightforward correlation of these features (e.g., spark energy or frequency of restrikes) with misfires or partial burns has emerged in this work.

This study has used high-speed imaging, image analysis and spark diagnostics to characterize aspects of the fuel spray, its interaction with the spark electrodes, and its effect on the spark in a spray-guided direct-injection gasoline engine. The principal conclusions are:

- Fluctuations in spray angle within an engine cycle and from cycle to cycle with the multihole injector examined here are small (a range of about 6° for the spray plume nearest the spark gap).
- Fluctuations in liquid distribution as gauged by the Mie-scattering intensity are significant: ~25% rms relative to the mean when integrated along the spray plume and several times larger when integrated over small (1.5-mm) regions within the plume or near the spark plug.
- The high velocities present near the spark gap at the time of ignition, coupled with the long spark duration, lead to dramatic spark stretching and frequent restrikes, which shorten the spark duration.
- The effects listed above show no significant correlation to misfires and partial burns in the engine configuration examined here.

It becomes apparent that the interaction of the spray with the spark cannot solely be responsible for the ignition instabilities observed in spray-guided DI engines although the spray shows significant cycle-to-cycle variability. For a closer understanding of the in-cylinder processes, the vapor phase must be taken into account.

5.1.2 Measurement of vapor and liquid phase concentrations with laser-induced exciplex fluorescence (LIEF)

For an internal extended study of the complex interaction of liquid and vapor fuel in a direct-injection combustion engine the laser-induced exciplex fluorescence methods can be a useful tool. As explained in section 4.2.6.1, on first view Laser-Induced Exciplex Fluorescence (LIEF), where the monomer is excited by a high energy laser beam, provides a convenient method for simultaneous measurement of gas- and liquid-phase fuel concentrations in an evaporating spray. The fluorescence signals of the liquid and the gas phase are spectrally well separated and therefore, imaging of the evaporation process of fuel sprays should be possible. However, on a closer look one realizes that reasonable quantitative analysis of LIEF signals requires thorough knowledge of the spectral properties of all the involved substances. Knowledge of the temperature dependence of the fluorescence intensity [87,88] of the liquid exciplex as well as of the monomer in the gas phase is especially important to quantify the signals and to correctly address the liquid-phase/vapor-phase cross-talk which is the major error source. In addition most exciplex system suffer from severe fluorescence quenching by oxygen – a fact that does not limit the applicability for the diagnostics of spray combustion processes as long as the interest is on qualitative information on spray processes only. Quantitative measurements, however, require a nitrogen atmosphere and are therefore limited to non-reactive processes, such as spray formation and evaporation in an DISI-engine before ignition.

After Melton [89] proposed the method in 1983, several different exciplex systems suitable for the study of in-cylinder mixing processes of gasoline and Diesel DI-engines have been applied and presented in literature:

Author	**System**	**(C_M/C_G)**	**λ_{em} [nm] M*/E***	**b.p. [°C]**	**Application**	**λ_{exc} [nm]**	**Fuel**	**Comments**
Melton 83 [89]	TMPD / naphthalene	10 / 1%	380 / 470	260 / 218	fuel vapor/liquid	313	synthetic diesel	qualitative
Parigger 98 [87]	TMPD / naphthalene	2.5 / 1%	380 / 470	260 / 218	temperature	308	n-heptane	$\Delta T < 1°$
Yeh 93 [90]	TMPD / naphthalene	0.5 / 5%	380 / 470	260 / 218	vapor conc.	355	3-component model fuel	in N_2
Kim 96 [91]	DMA / TMN	5 / 7%	355 / 405	193 / 145 (15 torr)	vapor/liquid	308	isooctane	fundamental investigations
Leipertz 96 [92]	TEA / benzene	2.9 / 2%	290 / 350	81 / 89	vapor	248	isooctane	qualitative
Shimizu 92 [93]	DMA / naphthalene	5 / 5%	335 / 410	193 / 218	vapor conc.	308	gasoline	
Melton 93 [94]	TEA / FB NPDEA / FT	10 / 0.5% 10 / 0.5%	290 / 350	90 / 85 108 / 116		266	hexane isooctane	in N_2; crosstalk from monomer
Ghandhi 94 [7]	DEMA / FB	9 / 0.5%	290 / 380	65 / 85		266	hexane	in N_2; coevaporative
Fröba 98 [95]	TEA / benzene	2 / 3.4%	290 / 350	90 / 80		248	isooctane	
Styron 00 [96]	TEA / FB	0.77 / 10.9%	290 / 337	90 / 55	vapor/liquid in engine	266	4-component model fuel	
Styron 00 [96]	TMPD / naphthalene	0.77 / 10.9%	380 / 470	260 / 218	vapor/liquid in engine	355	4-component model fuel	
Skogsberg 05 [97]	TEA / FB	9 / 1%	290 / 337	90 / 85		266		
Wieske 06 [61]	DEMA/FB	9 / 0.5%	290 / 380	65 / 85	vapor/liquid/ temp. in engine	266	hexane+ 20% MTBE	in air

Tab. 5.1: Laser-induced exciplex fluorescence in literature.

Melton [94] compared the fluorobenzene (FB) / triethylamine (TEA) exciplex system with the 4-fluorotoluoene (4FT) / n-propyl-diethylamine (NPDEA) system in different solvents (2-methylhexane, heptane, isooctane and n-hexane) and recommended 10% TEA, 0.5% FB in n-hexane ecause the good coevaporation properties of this particular

mixture. Ghandhi[7] used 0.5% fluorobenzene, 9% diethylmethylamine (DEMA) in n-hexane for imaging of injection processes.

More suitable for the study of Diesel sprays or the heavier components of gasoline is the system N,N,N',N'-tetramethyl-*p*-phenylendiamine (TMPD) / naphtalene / hexadecane that was used amongst other systems by Styron [96]. In this work an extensive characterization of the fluorescence of the fluorobenzene (FB) / diethyl-methylamine (DEMA) / n-hexane exciplex system is presented. This specific system was chosen for its excellent coevaporative behavior and because of its fluorescence characteristics. Fluorobenzene plays the role of the laser-excited monomer [98].

All presented experiments were conducted in nitrogen atmosphere to prevent oxygen quenching effects. Fig. 5.13 shows absorption spectra of both molecules. For most experiments a frequency quadrupled Nd:YAG laser at a wavelength of 266 nm served as excitation light source. Fluorobenzene shows moderate absorption, the absorption of DEMA at this wavelength is negligible. At conditions as encountered in a typical direct-injection engine (injection of 10 mg of fuel per cycle, combustion chamber volume of 30 ccm at TDC) this results in a overall attenuation of the exciting laser beam by ~25% neglecting scattering losses.

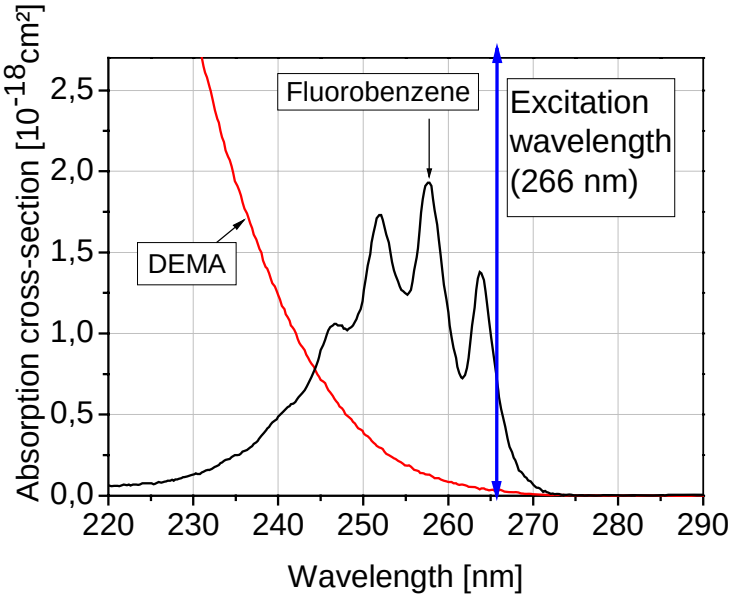

Fig. 5.13 Absorption spectra of fluorobenzene and DEMA.

5.1.2.1 Coevaporation

To guarantee quantitative interpretability of the LIEF data for the study of evaporating sprays one must ensure that all the exciplex components form an azeotropic mixture resulting in a constant composition of the liquid and the vapor phase and, hence, evaporate at the same rate as the fuel. Studies by Ghandhi [7] have shown that a mixture

of 0.5% fluorobenzene, 9% DEMA and 90.5% n-hexane evaporates without significant changes in the relative concentrations (see Fig. 5.14, right side). In order to improve the sensitivity of the vapor channel, in this work the fluorobenzene fraction was increased to 2%. The composition of the evaporating mixture, heated to its boiling point of T_b = 343 K, was checked by regularly taking samples during the process that were in turn analyzed for their composition with a gas chromatograph. The result can be seen in Fig. 5.14 (left side). The composition remains constant within the error margins of the measurement (~ ±1.5%).

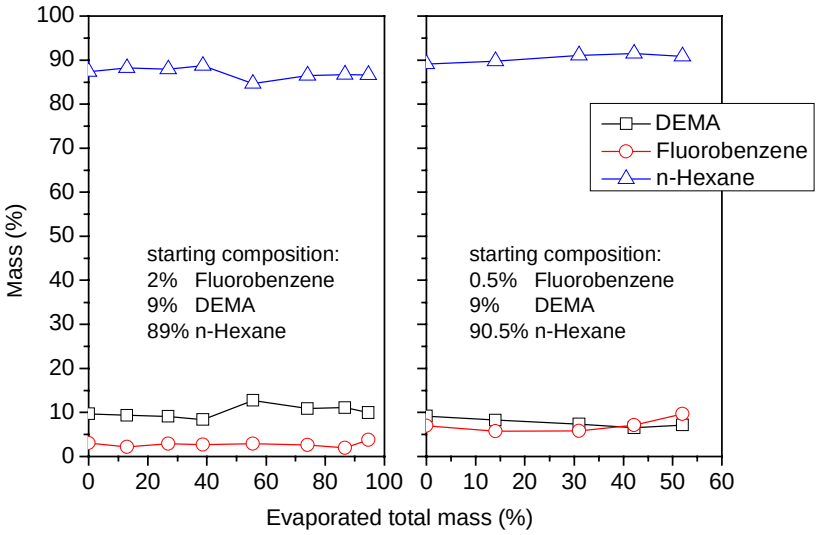

Fig. 5.14 Change of relative concentrations in the exciplex mixture- Left: Composition used in this work. right: composition used by Ghandhi [7].

5.1.2.2 Spectral characterization of the liquid exciplex

The high optical density of the exciplex solution in the given composition prevents the spectral characterization of the solution by means of a standard 10 mm cell. (over 99% of the excitation light at 266 nm would be trapped in the fuel/tracer mixture after 1 mm.) Simple dilution is not an option because that would cause a strong equilibrium shift in the exciplex forming reaction [99]. The temperature-dependent fluorescence of the liquid exciplex was therefore studied in a thin-layer cell with UV-light (266 nm) excitation. The cell was designed to avoid excitation light attenuation and signal re-absorption by the exciplex solution by reducing the layer thickness to 0.3 mm.

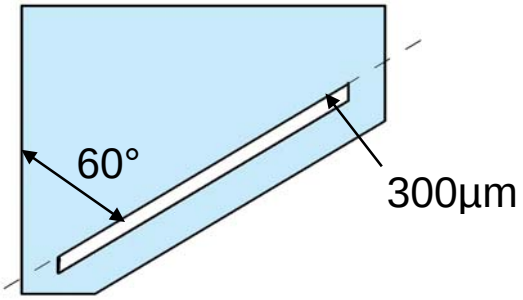

Fig. 5.15 Cross-section of the thin layer cell that was used for obtaining the liquid phase spectra.

Spectra of the liquid exciplex were measured using the described thin layer cell in a UV-vis photospectrometer (*Varian Cary Eclipse*). As shown in Fig. 5.15 the spectra are measured in reflective mode in order to keep the excitation intensity at the point of measurement is kept constant. The angle of inclination of the cell was chosen to 60° in order to prevent the excitation beam to be reflected directly into the detector. In order to suppress the residual stray light a WG 295 longpass filter was applied. The exciplex solution was purged with nitrogen before the measurement. During the measurement the sample compartment of the spectrometer was also purged with nitrogen.

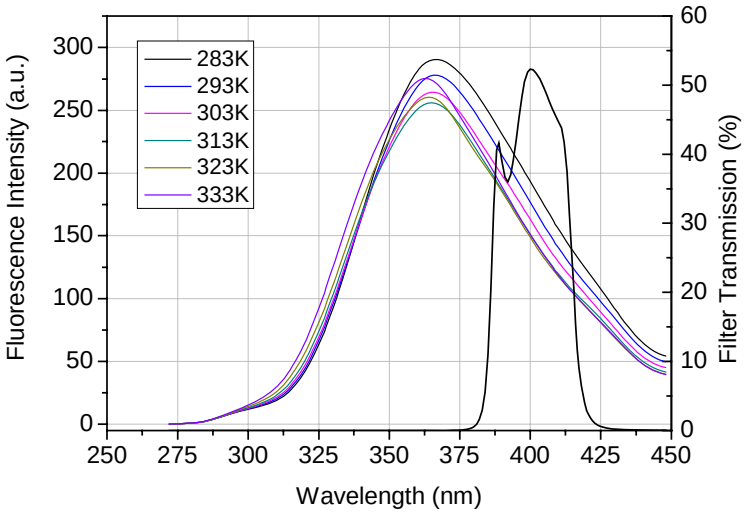

Fig. 5.16 Fluorescence spectra of the liquid exciplex system at temperatures between 283 and 333K. Excitation wavelength was 266 nm.

The set of curves shown in Fig. 5.16 are the fluorescence spectra of the liquid exciplex at temperatures from $T_l = 283$ K to $T_h = 333$ K. In contrast to earlier works on this subject[61,98], the overall fluorescence intensity is not decreasing substantially (see Fig. 5.18). Instead a distinct blueshift of the entire spectrum and a slight increase of residual monomer fluorescence around 295 nm with increasing temperature is observed (see Fig. 5.17). The origin of the spectral blueshift is controversial. It may indicate a reduced binding energy of the fluorobenzene/DEMA exciplex at elevated temperatures,

but it could also be attributed to a change in the interactions of the exciplex with the solvent (n-hexane) molecules.

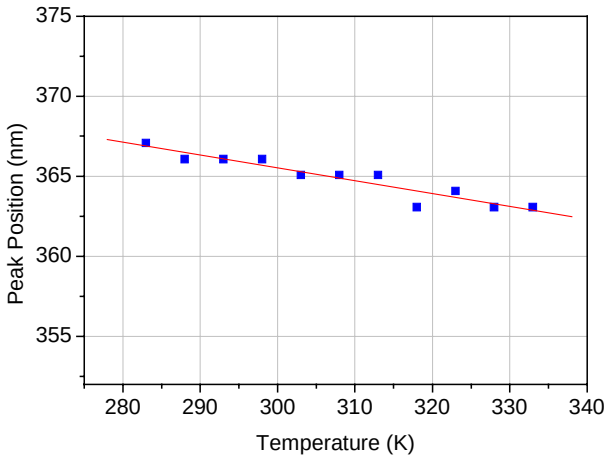

Fig. 5.17 The peak of the exciplex spectrum shifts to shorter wavelengths with increasing temperature.

The increasing monomer signal indicates an equilibrium shift in the exciplex formation reaction.

The fluorescence intensity that is transmitted through a narrowband filter centered at 400 ±10 nm (as was used in a spray experiment to detect the liquid phase, see Fig. 5.16), drops by 23% when the temperature is increased from 283 to 312 K and then stays roughly constant until the boiling point of the exciplex mixture is reached (see Fig. 5.18). The intensity drop is mainly due to the observed blueshift in the spectra since the peak “moves out” of the filter’s transmission window with increasing temperature (compare Fig. 5.16).

If we look at the temperature dependence of the total fluorescence intensity of the liquid exciplex, we observe only a slight decrease by ~13% from 283 to 312 K. For higher temperatures the intensity even increases again to about 93% of the intensity at 283 K. This result is different from the results of similar experiments by other groups [61] who found strong decrease of the fluorescence intensity with increasing temperature. The main difference in the experimental setup was that 10 mm cells were used for the spectral analysis.

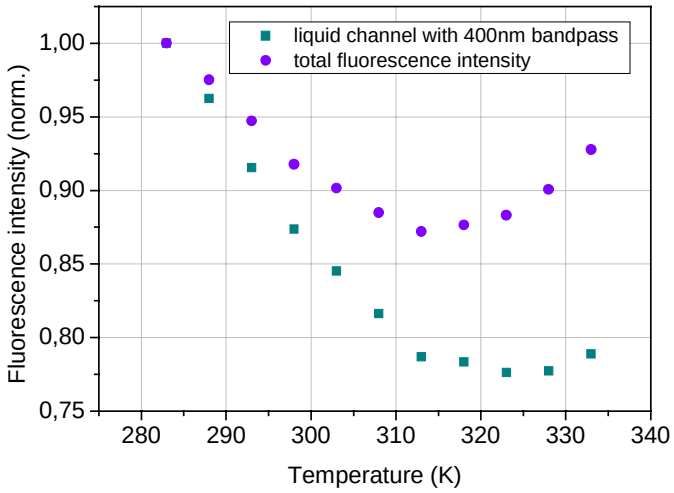

Fig. 5.18 Integrated signal intensity of the liquid exciplex

5.1.2.3 Liquid-vapor cross-talk

One major error source in the quantitative measurement of liquid and vapor phase concentrations in an evaporating fuel spray with the laser-induced exciplex fluorescence technique is the so-called cross-talk signal. It arises from the spectral overlap between the liquid exciplex and the monomer (fluorobenzene) fluorescence. The absolute amount of cross-talk signal depends on the optical filters used for detection of the vapor and liquid phase fluorescence.

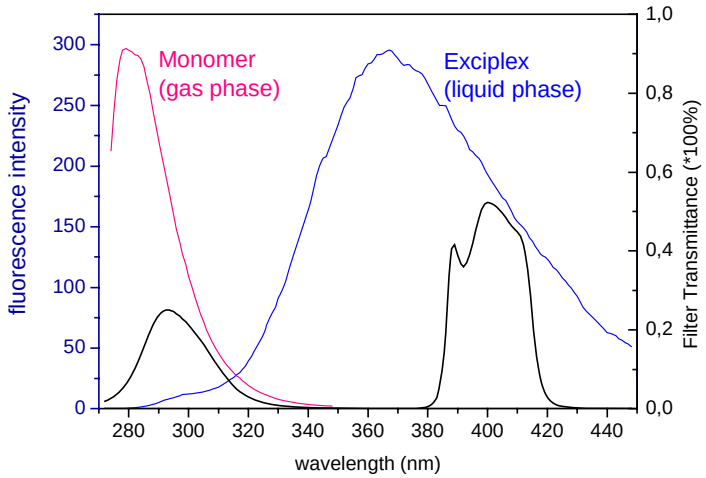

Fig. 5.19 Normalized fluorescence spectra of fluorobenzene vapor and the liquid exciplex together with two filter curves for detection of vapor and liquid phase.

In our case, while there is no vapor-phase signal present in the liquid channel around 400 nm, there is a considerable amount of liquid-phase signal to be expected in the vapor phase channel around 295 nm (see Fig. 5.19). In order to quantify the vapor phase

signal correctly, this cross-talk signal must be corrected for. As we saw in the previous section, the liquid phase signal is strongly dependent on temperature, therefore, the cross-talk signal is also expected to show a significant temperature sensitivity.

For a known temperature one can calculate from the liquid phase signal the cross-talk contribution to the vapor phase channel.

As Fig. 5.20 shows, the cross-talk seems to increase linearly with increasing temperature up to the boiling point of the exciplex mixture.

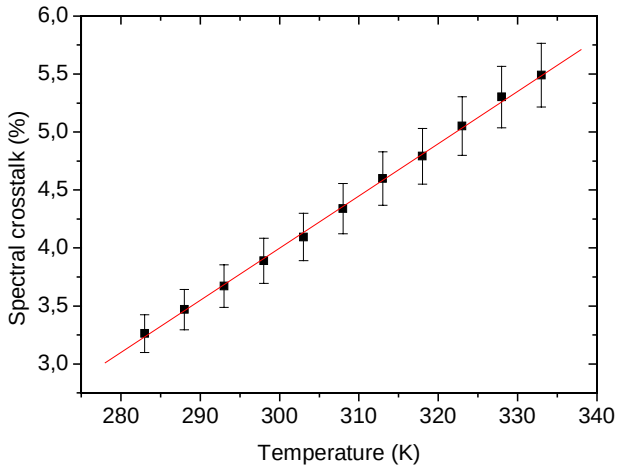

Fig. 5.20 Absolute cross-talk signal for the filter combination used in this work

Fig. 5.21 shows an example of the cross-talk effect in a spray measurement.

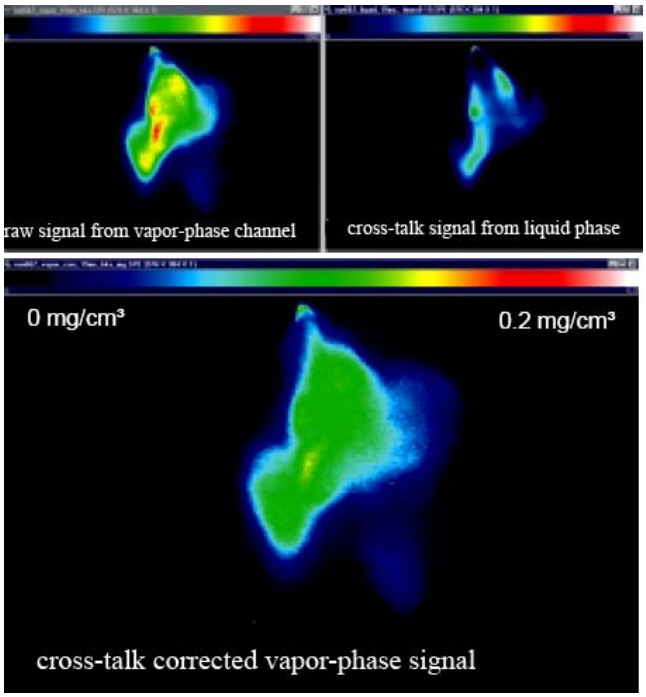

Fig. 5.21 Example of the cross-talk effect in a spray image. The top left image shows the uncorrected vapor-phase signal, the top right image shows the cross-talk signal as obtained from the liquid phase channel. The lower image shows the corrected vapor-phase signal. In this example the temperature dependence of the cross-talk is not yet considered.

5.1.2.4 Exciplex LIF as liquid-phase temperature probe

The temperature sensitivity in intensity and spectral shape of the liquid exciplex fluorescence can be used to actually measure the temperature of the liquid phase in the way that was described in chapter 4.3.3.5.

To obtain the spectral temperature sensitivity coefficient $\beta(\lambda)$ (see equation (4.27)) the logarithmic intensity ratio at each temperature is plotted against $\left(\frac{1}{T_0}-\frac{1}{T}\right)$. The sensitivity coefficient β can then be obtained by determining the slope of the linear regression. In that way β is calculated for every single wavelength in the fluorescence spectrum, as shown in Fig. 5.22. Negative β indicates an increase, positive β a decrease of the fluorescence intensity with rising temperature. The objective is to find two wavelength regions that, while both showing high overall fluorescence intensity, have a preferably high difference in β.

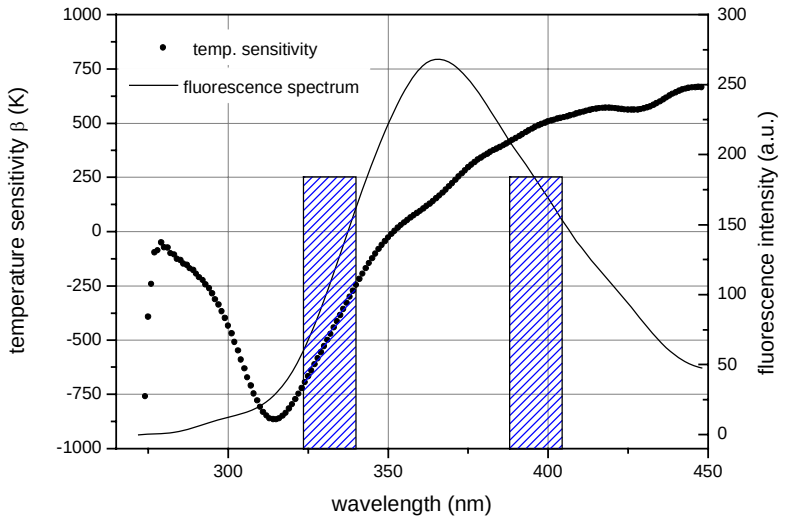

Fig. 5.22 Temperature sensitivity of the fluorescence spectrum of the FB/DEMA exciplex

Fig. 5.22 shows the temperature sensitivity curve of the exciplex together with an emission spectrum according to the definition in paragraph 4.3.3.5. The shaded boxes denote a possible combination of bandpass filters for a two-color LIF temperature measurement. If we decide to fix one detection band at 400 ± 10 nm (which will later be also used for the liquid concentration measurement) we must determine the ideal transition wavelength regime for the second filter. There is, however, a trade off between temperature sensitivity and signal-to-noise ratio. As can be deducted from the spectral shape of the exciplex fluorescence and as shown in Fig. 5.23, unfortunately the higher the temperature sensitivity of a filter combination is the lower is the overall signal strength in the second liquid channel. The combination of a 400 ± 10 nm and a 335 ± 10 nm bandpass seems to be a reasonable compromise. This combination shows a fair temperature sensitivity ($\Delta\beta \approx 800$ K) together with a comparable signal intensity in both detection channels – resulting in a good signal-to-noise ratio.

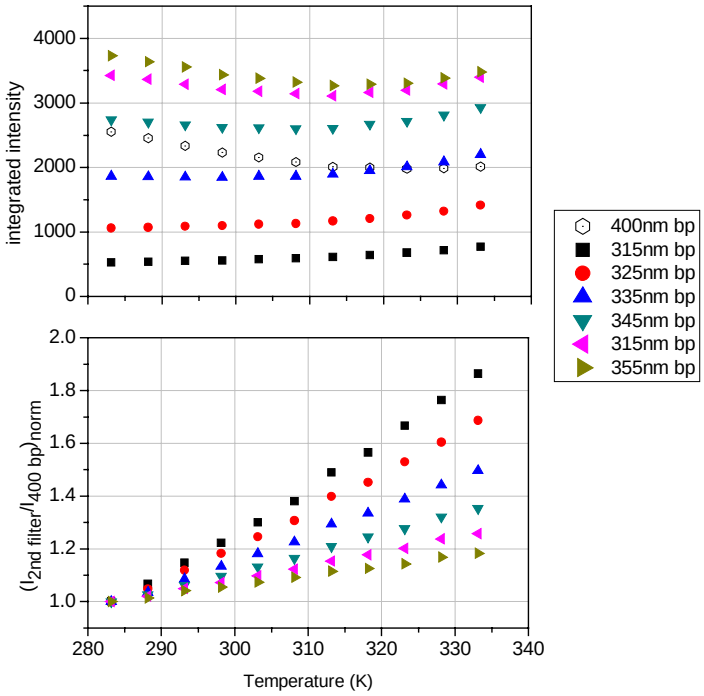

Fig. 5.23 Top: Absolute exciplex fluorescence intensity for different bandpass filters. Bottom: Normalized ratio of the fluorescence intensities for different filter combinations.

5.1.2.5 Characterization of the gas-phase fluorobenzene fluorescence

After correcting the vapor-phase signal for cross-talk by subtracting a liquid-phase-temperature-dependent fraction of the liquid-phase signal from the vapor phase, we assume the vapor-phase fluorescence to originate solely from excited fluorobenzene molecules. Earlier studies of structurally similar molecules such as toluene [58] or benzene hint that there might be also a strong temperature dependence in the fluorescence of fluorobenzene vapor. Experiments in a heated nitrogen stream containing ~0.1% fluorobenzene surrounded by a nitrogen co-flow were conducted in order to quantify the temperature dependence of the fluorobenzene fluorescence. Fluorobenzene was excited by the focused beam of a frequency-quadrupled Nd:YAG laser (*Continuum*), fluorescence was detected by a UV-sensitive photomultiplier. To avoid stray light from the laser a bandpass filter at 295 ± 10 nm was applied. The schematic setup is shown in Fig. 5.24.

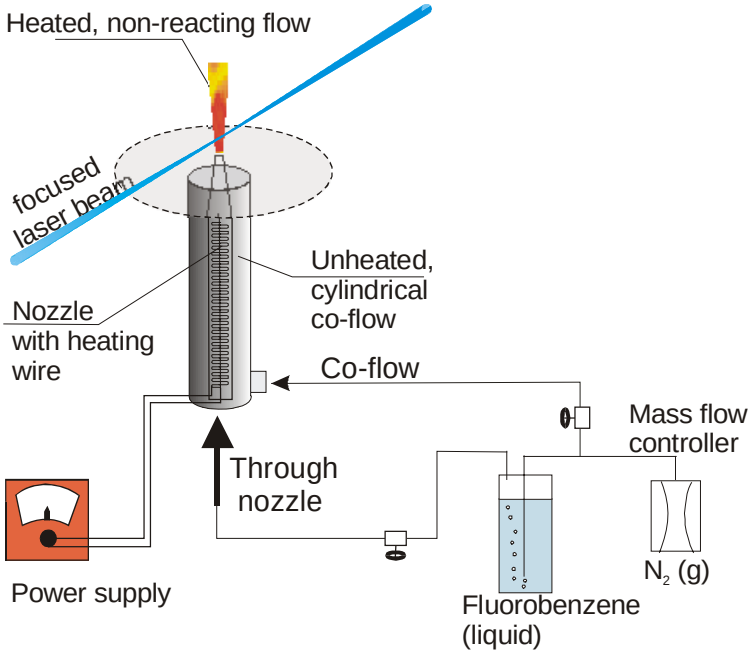

Fig. 5.24 Experimental setup for the characterization of the fluorescence of fluorobenzene.

To exclude saturation effects, the fluorescence at room temperature was measured at various laser energies. As clearly visible in Fig. 5.25, the LIF signal of fluorobenzene is linear only for fluences below 30 mJ/cm^2. Therefore, all experiments were conducted with a laser energy fluence of 10 mJ/cm^2.

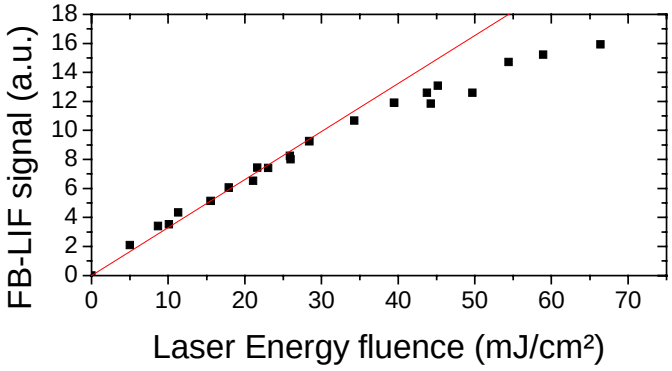

Fig. 5.25 Saturation of the fluorobenzene LIF signal

The temperature of the gas stream could be varied between room temperature and 600 K. The temperature was calibrated at the point of measurement with a precision K-type thermocouple. The results are presented in Fig. 5.26.

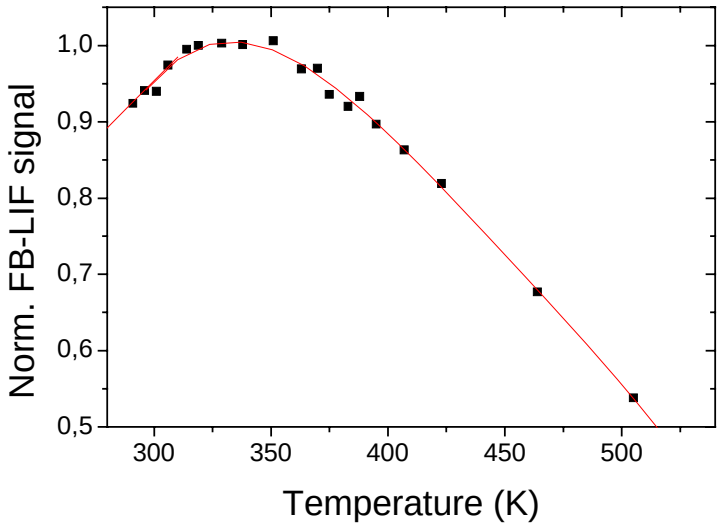

Fig. 5.26 Temperature characteristics of fluorobenzene vapor LIF

With increasing temperature the signal increases until it reaches its maximum at a temperature of about 338 ± 10 K and decreases then monotonicly. Earlier studies of fluorobenzene in nitrogen showed very similar results and also indicated that there is only a very small dependence of the LIF signal of fluorobenzene on pressure [100]. The results show that the vapor-phase temperature dependence in the range relevant for the later described experiments is rather small (< 10 %).

5.1.2.6 Fluorescence lifetimes of fluorobenzene

For the same experimental conditions as decribed in the last section the liftetime of the vapor-phase fluorobenzene fluorescence in nitrogen was measured by the use of time-correlated single-photon counting (TCSPC) with excitation of the sample by a pulsed Ti:Sapphire laser. TCSPC has become a standard method for the determination of fluorescence lifetimes in condensed matter down to 100 ps upon excitation with pulsed light sources, e.g., lasers or sub-nanosecond-LEDs (the TCSPC principle allows lifetime measurements below the duration of the excitation pulse, and if necessary the system response can be deconvoluted). In addition, TCSPC gained reasonable interest in the field of fluorescence microscopy because of the rather simple implementation of commercially-available TCSPC data evaluation boards in combination with highly-sensitive avalanche photo diodes (APD) [101,102].

The experimental setup corresponds to Fig. 5.24, the laser lightsource for the lifetime measurements was a short-pulse (~ 500 fs) frequency-tripled Ti:Sapphire laser (*MIRA Optima 900-P, Coherent*) that was operated at 76 MHz and 798 nm with pulse lengths of approximately 300 fs. As fluorobenzene fluorescence lifetimes range up to several nanoseconds, a pulse picker (*APE, pulse select*) was used to ensure an interval between

pulses of 200 – 80 ns (depending on the measurement conditions). A 3rd harmonic generator (*MIRA 9300, Coherent*) allowed for wavelength conversion to 266 nm. Fluorescence signals are detected by a UV-sensitive photomultiplier (*PMH 100, Becker & Hickl*) and processed by a TCSPC card (*SPC-132, Becker & Hickl*). TCSPC is a statistical method for lifetime measurements. After every excitation pulse statistically less than one fluorescence photon is emitted into the detector. This photon is acquired together with its time delay relative to the excitation pulse and the delays are evaluated statistically.

Photophysical models for similar molecules (toluene [103,104]) predict a monoexponential decay for the excitation wavelength of 266 nm at low temperatures, as for low vibrational excitation intersystem crossing (ISC) is the only relevant non-radiative de-excitation process. At higher temperatures the decay becomes bi-exponential what can be explained by an additional non-radiative decay path: Internal conversion (IC) becomes important for selected vibrational states at higher energies. ISC and IC states may be populated either directly via absorption or via intramolecular vibrational redistribution (IVR) following absorption [105]. With increasing temperature IVR becomes more efficient, resulting in an increasing relevance of this fast decay channel, i.e. an increase of the ratio (cf.). The temperature dependence of the long-lived state on the other hand is due to more effective intersystem crossing (ISC) to the triplet state. This spin-forbidden process becomes vibrationally allowed with increasing temperature.

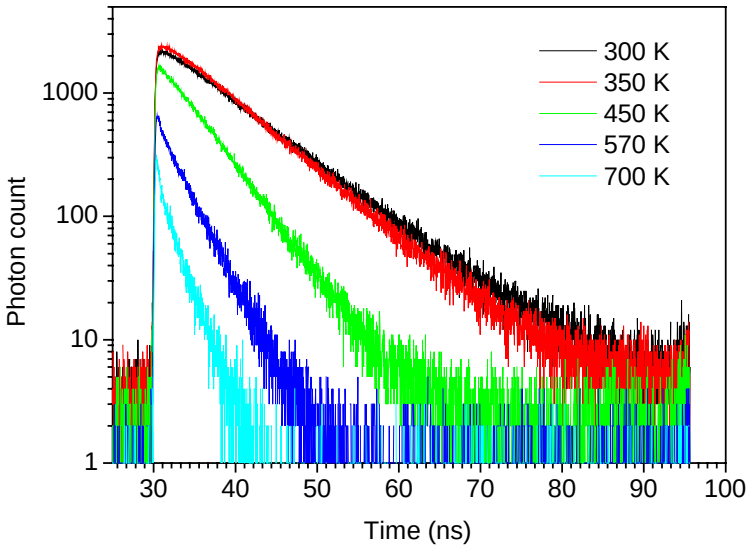

Fig. 5.27 Decay curves of fluorobenzene fluorescence at different temperatures (logarithmic intensity scale). For the higher temperatures the bi-exponential behavior can be observed from the steep early decay. The time offset is determined by the trigger setting of the TSCPC board.

Fig. 5.27 shows raw measurement data for fluorobenzene LIF at five different temperatures. The signal-to-noise ratio was better than 100 for all measurements.

A bi-exponential decay function of the following form

$$I = I_0 + A_s e^{-(t-t_0)/\tau_s} + A_l e^{-(t-t_0)/\tau_l} \tag{5.36}$$

describes the fluorescence decay very accurately. According to [104] there is a long lifetime component (indicated by the index *l*) that dominates the fluorescence decay at lower temperatures and is attributed to ISC. At temperatures above 500 K a short lifetime component (indicated by the index *s*) becomes evident, that most likely originates from IC. A standard Levenberg-Marquardt fitting algorithm was used to fit the data yielding the two lifetime components τ_s and τ_l. (For temperatures below 500 K the fit yields equal values for τ_s and τ_l as well as for A_s and A_l.). Fig. 5.28 shows the resulting lifetimes for temperatures between 300 and 800 K.

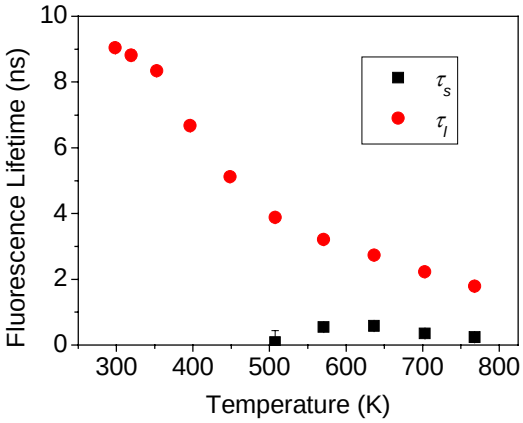

Fig. 5.28 Fluorescence lifetimes of fluorobenzene in the temperature range between 300 and 800 K and atmospheric pressure.

T (K)	**τ_l (ns)**	**τ_s(ns)**	**A_s / (A_s+A_l)**
299	9.04	-	-
319	8.81	-	-
353	8.34	-	-
396	6.67	-	-
449	5.12	-	-
507	3.88	-	-
571	3.21	0.54	0.18
637	2.73	0.58	0.33
703	2.22	0.35	0.44
768	1.79	0.24	0.49

Tab. 5.2: Fluorescence lifetimes and relative amplitudes of fluorobenzene.

The experimental setup did not allow variation in the ambient pressure, so that all results are valid for atmospheric pressure only. Nonetheless, the strong temperature dependence of the fluorescence lifetime of fluorobenzene proposes another possibility to measure the vapor-phase temperature through a local fast lifetime measurement.

5.1.2.7 Relative signal strength of liquid and vapor phase fluorescence

Relative signal strength of liquid and gas-phase fluorescence were determined in a spectrally resolved manner from measurements by Graf [98] with the intensity given per fluorescing molecule or molecule pair respectively for laser excitation at 266 nm.

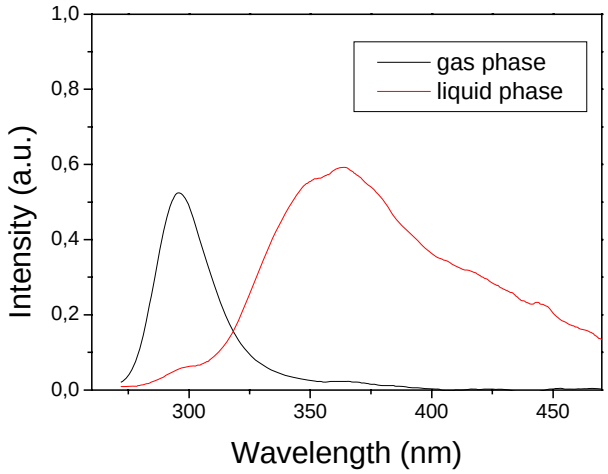

Fig. 5.29 Relative signal strength of vapor and liquid phase fluorescence per molecule for fluorobenzene and the DEMA/FB Exciplex [98]. Excitation wavelength was at 266 nm.

The collected spectral information about the FB/DEMA/n-hexane exciplex system now enables us to quantitatively measure liquid-phase temperatures as well as liquid and vapor-phase concentrations in an evaporating spray. For the temperature measurement calibration at one point with known temperature T_0 is necessary. The concentration measurement can be calibrated by correlating a known vapor concentration to the detected intensity value. Same holds for the calibration of the liquid phase.

5.1.2.8 Fuel Spray Experiment and results

To demonstrate the applicability of this exciplex system to a practical system, it was tested with different types of gasoline injectors for in a high-temperature pressure-chamber. As done before in the spectral characterization, all experiments were conducted in a pure nitrogen atmosphere.

A frequency quadrupled Nd:YAG laser at 266 nm was used as a light source. Exciplex and monomer fluorescence respectively were simultaneously detected by a three-color high speed ICCD camera (Photron Spectra). A combination of a WG 305 (Schott) long pass filter and a 295 nm bandpass was used to separate the monomer fluorescence, the

exciplex fluorescence was detected through a custom-made 400 nm bandpass. The filter curves are presented in Fig. 5.19. Different types of injectors were used: One swirl injector with a spray angle of 70° and a six-hole injector with a spray angle of 50°. The exciplex mixture was injected into a spray chamber, operated at pressures from 1-5 bar. The temperature and gas mixture inside the chamber was controlled. The nature of the exciplex technique made it necessary to work in a pure nitrogen atmosphere.

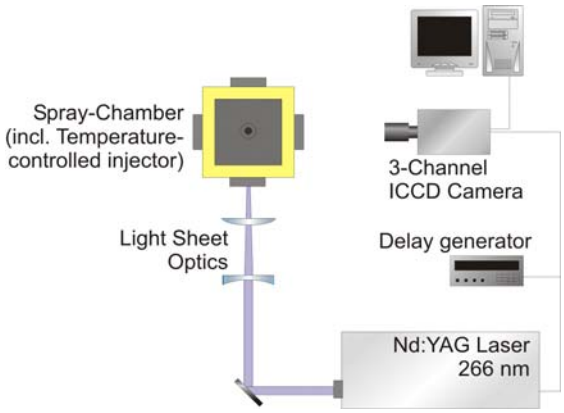

Fig. 5.30 Experimental setup: High-pressure, high-temperature spray chamber (slow N_2 purge flow).

From images early in the evaporation process, when no vapor-phase signal is expected, the cross-talk can be calibrated by comparing the signals of the vapor- and the liquid phase channel. The liquid phase temperature has to be known or assumed in order to consider the temperature effect on the cross talk signal. After subtracting the temperature dependent cross-talk signal the pure vapor-phase signal remains. Neglecting the temperature dependence results in an error in the concentration measurement of 10-15%. Results are shown in Fig. 5.31.

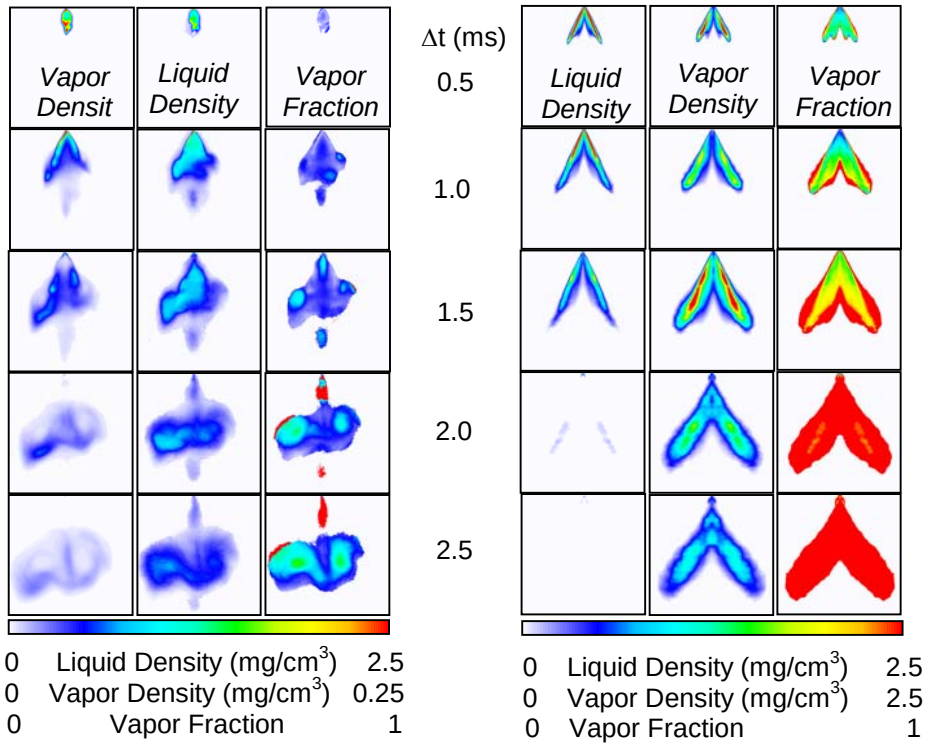

Fig. 5.31 Liquid and vapor concentrations for two injection processes: left, swirl injector, spray angle 70°, injected into 1 bar, T = 293 K; right: 6-hole injector, spray angle 50°, injected into 5 bar, T= 368 K.

The differences between the two injector types are evident: The multi-hole spray evaporates more homogeneously and produces an ignitable mixture more reliably. The swirl injector spray shows turbulent structures and a strong asymmetry. The faster evaporation of the multi-hole spray is mainly due to the higher fuel and ambient temperature. Nonetheless, the vapor fraction for the multi-hole spray is far more homogeneous, a fact that in an actual engine should lead to better ignition stability and lower cycle-to-cycle variations.

5.1.3 Tracer LIF in commercial Diesel fuel

All fluorescence experiments discussed so far have one common and very important disadvantage: they use some type of model fuel instead of real gasoline or Diesel. The reasons for that are commonly one or more of the following:

- prevention of fluorescence background from fluorescing fuel components
- better comparability with spray models that use single-component fuels or simple mixtures

Commercial fuels (gasoline and Diesel fuel) contain a variety of fluorescing compounds. Sazhin et al. have studied the spectral properties of Diesel fuel [106] and have found large absorption cross-sections for near-UV wavelengths. However, the fluorescence signal of Diesel and gasoline fuel is difficult to quantify because it originates from a large number of different species that have individual dependencies on

temperature, pressure and collisional quenching and that can be inhomogeneously distributed because of differences in their evaporation and transport properties. In order to simplify laser-based fuel diagnostics organic molecules can be added to the fuel as fluorescent tracers.

Usually tracers are preferred that can be excited within a wavelength range where the fuel is transparent, in order to avoid laser attenuation, energy transfer and interfering fluorescence signals. Commercial Diesel fuel has low absorption cross-sections in a wavelength range starting at ~600 nm and reaching into the near infrared.

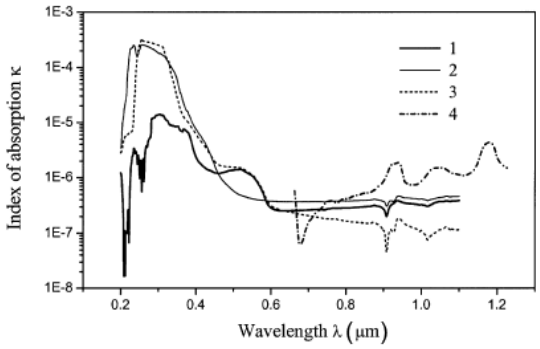

Fig. 5.32 Spectral distribution of the index of absorption κ in the ultraviolet–near-infrared range: different brands of Diesel fuel (1-3); n-heptane (4) (from[106]).

In recent years strong laser light sources have become available which operate in this wavelength region and should allow LIF measurements in sprays of commercial fuels. One laser system that fulfills the requirements for LIF in Diesel fuel and that was applied in this work is presented in section 4.4.1.4. It produces short pulse bursts at a wavelength of 671 nm

For this reason it has become necessary to find and evaluate possible fluorescent tracers that can be excited and selectively detected within in this wavelength range. Laser dyes, are commonly used as fluorescent tracers [107]. They usually have high fluorescence quantum yields and are available for excitation throughout the visible spectrum, reaching into the UV and NIR. They have a negligible vapor pressure and usually decompose before boiling. It is commonly assumed, that for moderate evaporation the dye accumulates completely inside the droplet during the evaporation process [57] thus giving a measure of the initial spray volume. No signal from the gas phase is expected. As a representative of this group Rhodamine 800 has been analyzed in this work.

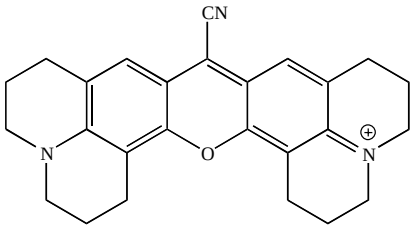

Fig. 5.33 Molecular structure of the Rhodamine 800 cation [108]

Another group of possible tracer substances is formed by fluorescent dyes and markers used in bioscience. These fluorescent dyes are optimized for quantum yield to enable the LIF detection of single molecules [109]. Fluorescence markers have been developed that can be excited at wavelengths >600 nm. These efficient fluorescence tracers, therefore, became possible candidates for spray diagnostics in real fuels as well. As a representative of this group Atto 680 (ATTO-TEC, Siegen, Germany) has been analyzed in this work.

Both analyzed tracer molecules are hydrophilic and therefore dissolve poorly in commercial fuels, which consist primarily of non-polar hydrocarbons (see Tab. 5 .3).

Hydrocarbon	**typical mass fraction (%)**
Alkanes (C_{10}-C_{25})	40 – 70
Heavy Alkenes (>C_{25})	< 2
Monocyclic Naphthenes	10 – 20
Dicyclic Naphthenes	< 5
Alkenes	0.1 – 5
Aromats	10 – 30

*Tab. 5 .3: Constituents of commercial Diesel fuels from Prof. Dr. A. Zeman (em.): Beitrag zur **Chemie der Kraftstoffe** (updated Okt.2005)*

As we will see, in order to get a sufficiently strong fluorescence signal, one needs tracer concentrations in the concentration range of 10^{-6} mol/l. The necessity for such comparably high concentrations is based on the fact, that the quantum yield of the fluorescent tracers is comparably low in this particular environment. This is believed to be caused by effective fluorescence quenching by aromatic hydrocarbons contained in the fuel. Both dyes show high quantum yields of about 0.4 when dissolved in ethanol, but this value drops by a factor of 1.9±0.8 in a fuel environment. The absorption cross-section in Diesel also drops by a factor of 2.0±0.5.

In order to obtain adequate tracer concentrations, we dissolved a specified amount of the tracer (which, in both cases comes as solid crystals at room temperature) either in

pure ethanol or in hexanol and mixed a small amount of this highly-concentrated solution (c = 6×10^{-5} mol/l) with commercial Diesel fuel. The goal was to keep the alcohol fraction in the mixture as low as possible (<10%). For higher volume fractions significant changes in the boiling-behavior and the viscosity of the fuel and therefore in evaporation characteristics and spray formation must be expected. Hexanol has the advantage of better solubility in fuel and a boiling point (T_{boil} = 430 K), that is closer to the average boiling temperature range of heavy fuels like Diesel (T_{boil} ≈ 550 K) compared to that of ethanol (T_{boil} = 351 K). On the other hand the quantum yield of the used dyes drops by a factor of 3.3±0.8 when solved in hexanol instead of ethanol and the solvability of the dyes in hexanol is in general lower than in ethanol.

5.1.3.1 Spectral characterization

Absorption spectra of different tracer-doped fuel samples were taken with a absorption-spectrometer (*Varian CARY 500 Scan*) and temperature-dependent LIF emission spectra were measured with a UV-vis photospectrometer (*Varian CARY Eclipse*). The samples were prepared with commercial Diesel fuel mixed with different amounts of a concentrated solution of the respective tracer in ethanol (c = 7.3×10^{-5} mol/l). Different amounts of this solution were mixed with Diesel in a standard 10 mm quartz cuvette. The absorption spectra were recorded at room temperature against an n-hexane reference. For the fluorescence spectra the temperature of the sample could be varied from 15 – 60°C. Fig. 5.34 shows absorption spectra of Rhodamine 800 and Atto 680 in a Diesel/ethanol mixture at different tracer concentrations and ethanol volume fractions in comparison to the absorption spectrum of pure Diesel fuel (measured against n-hexane). Both fluorescence tracers show strong absorption in the relevant wavelength region of 600 – 800 nm. The absorption of Diesel fuel is negligible at λ > 650 nm (absorption < 0.1% at 10 mm path length).

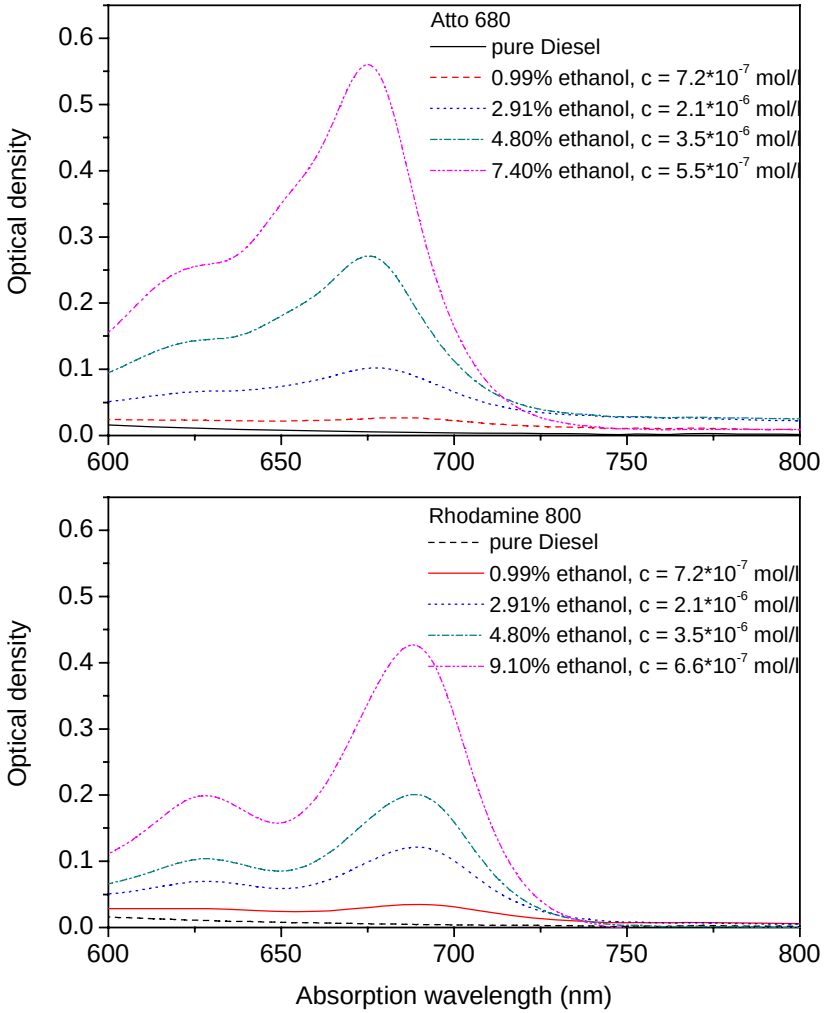

Fig. 5.34 Absorption spectra of Atto 680 (top) and Rhodamine 800 (bottom). Indicated in the boxes are the ethanol fraction of the mixture and the corresponding tracer concentrations in respect of the Diesel/ethanol mixture.

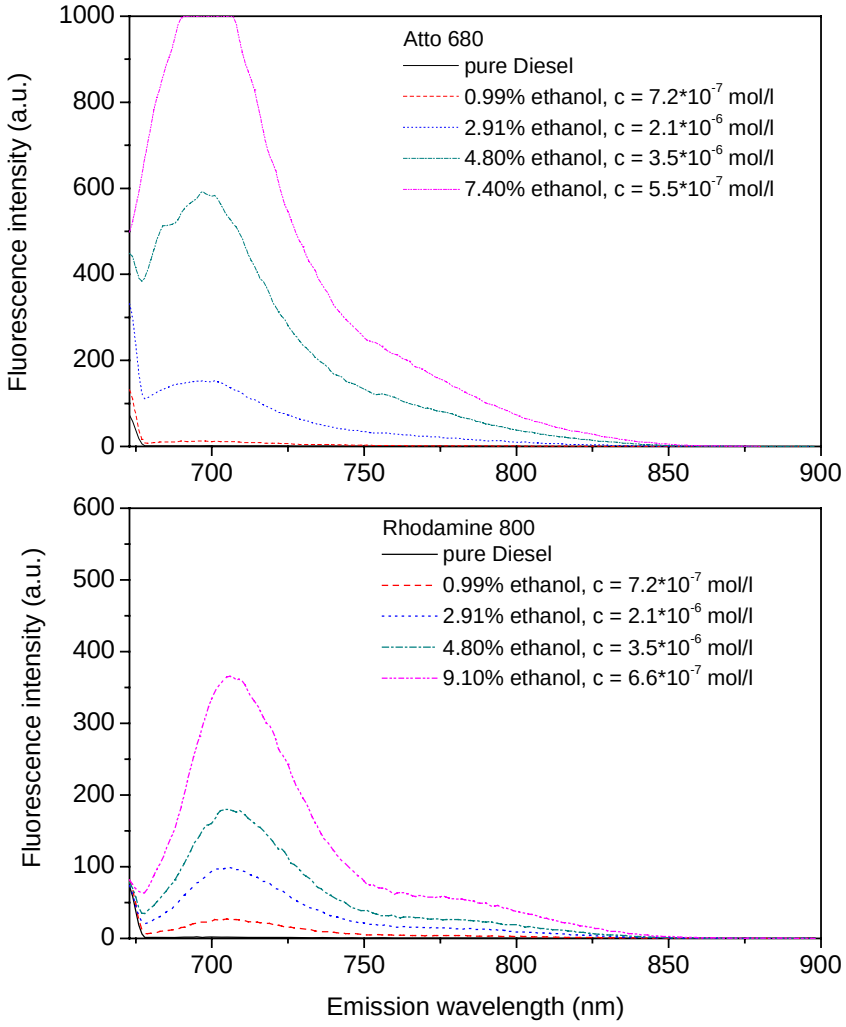

Fig. 5.35 Fluorescence spectra of Atto 680 (top) and Rhodamine 800 (bottom). Indicated in the boxes are the ethanol fraction of the mixture and the corresponding tracer concentrations in respect to the Diesel/ethanol mixture.

Fig. 5.35 shows the associated fluorescence spectra with the excitation wavelength at 671 nm. The emission maximum occurs at 696 nm and 705 nm for Atto 680 and Rhodamine 800, respectively. As seen in Fig. 5.36 for Rhodamine 800 the integrated fluorescence intensity is linear with the tracer concentration over the whole investigated range whereas the fluorescence intensity as well as the absorption of Atto 680 seems to show a quadratic dependence on the tracer concentration. The reason for this is still unknown.

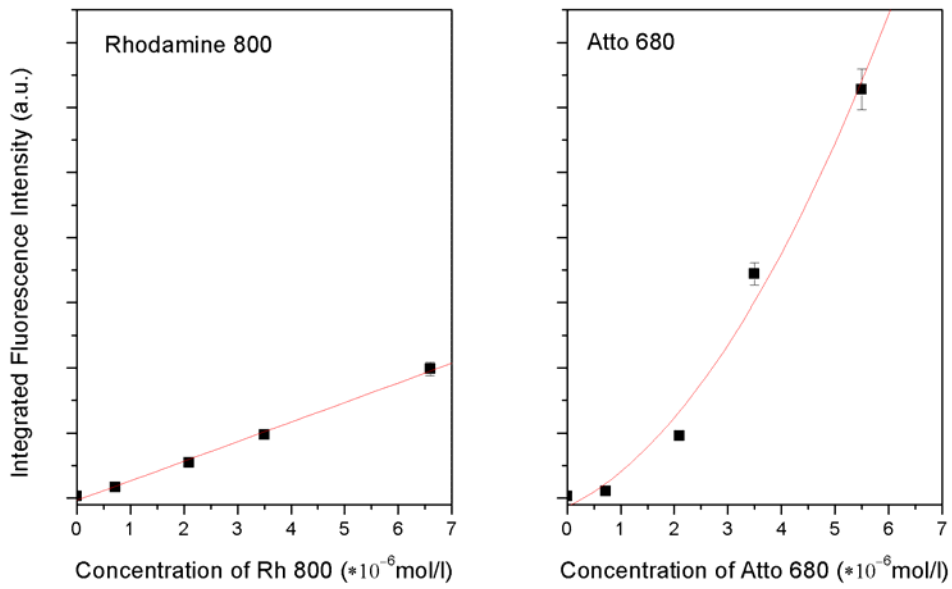

Fig. 5.36 Integrated fluorescence intensity for Rhodamine 800 and Atto 680 for different dye concentrations. The excitation wavelength was 671 nm.

The temperature-dependence of the fluorescence intensity of Atto 680 and Rhodamine 800 in Diesel fuel has been evaluated in a temperature range from 16 – 60°C. The sample was slowly heated up, and spectra were measured at different temperatures. It turned out that the shape of the spectra as well as the peak position did not change with temperature. Fig. 5.37 shows the change of the integrated fluorescence intensity with temperature.

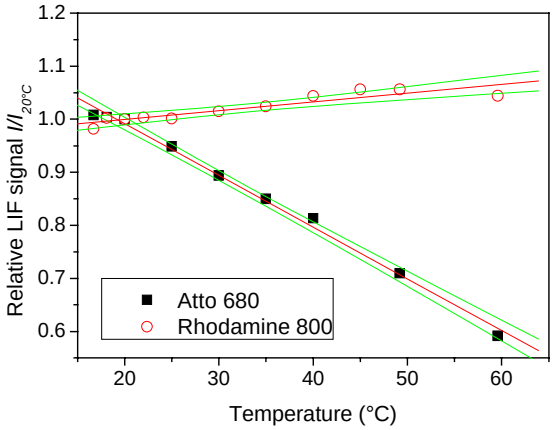

Fig. 5.37 Temperature dependence of the integrated fluorescence intensity. The intensity is normalized to its value at 20°C. The tracer concentration in both cases was $c_{tracer} = 3.5 \times 10^{-6}$ mol/l.

The intensities were corrected for thermal expansion of the solvent. Atto 680 shows strong decrease in fluorescence intensity with increasing temperature. After taking the

last spectrum at 60°C the Atto 680 sample was cooled to 22°C, the fluorescence intensity increased again but did not reach its former value. This leads to the assumption that the Atto 680 molecules decompose at higher temperatures or the solution changes its structure (i.e. separation of tracer and fuel). The fluorescence of Rhodamine 800 showed little variation with increasing temperature. No indications for decomposing of Rhodamine 800 or deterioration of the purity of the solution of the were found.

A comparison of the fluorescence intensity of Rhodamine 800 and Atto 680 in Diesel is shown in Fig. 5.38.

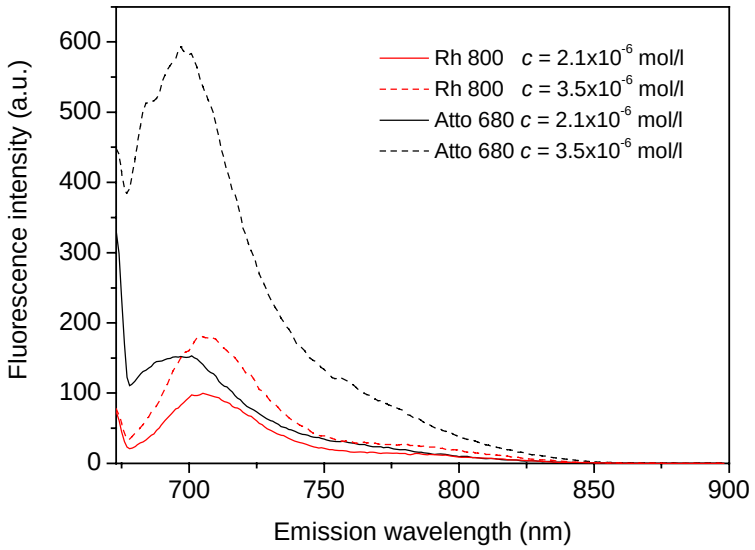

Fig. 5.38 Comparison of the fluorescence of Rhodamine 800 (red lines) and Atto 680 (black lines) for equa ldye concentrations.

The fluorescence of Atto 680 at higher concentrations seems to be much more efficient in the Diesel environment than Rhodamine 800. The reason why the relative factor between the fluorescence intensity of Atto 680 and Rhodamine 800 changes repeatably from 2 to 3 when raising the respective dye concentration from 2.1×10^{-6} to 3.5×10^{-6}mol/l is not known. The same behavior is observed with the relative absorption strengths and may be due to an unknown interaction between the Atto 680 molecule and the solvent. Both dyes have been tested for fluorescence quenching by oxygen [57] by purging the samples, first with nitrogen, then with oxygen. Fluorescence spectra were taken before and after the purging with oxygen no significant changes in the intensity were found.

5.1.3.2 Imaging experiments and results

Two-dimensional LIF and Mie-scattering images of a model spray have been recorded using the experimental setup shown in Fig. 5.39.

For these experiments the Nd:$YAlO_3$ laser system described in chapter 4.4.1 was applied. The tracer concentrations were 2×10^{-6} mol/l Rhodamine 800 and 2×10^{-6} mol/l Atto 680, respectively in Diesel with 5% hexanol. A standard medical nebulizer was used to generate a very homogenous spray with droplets of an average diameters of ~ 8.5 µm. The laser beam was formed into a thin light sheet ($d \approx 0.5$ mm) by a cylindrical lens ($f = 750$ mm). The LIF signal was imaged onto an ICCD camera (LaVision, *Streak Star*) by a Nikon $f = 105$ mm, $f_{\#} = 2$ macro lens. Scattered laser light was suppressed by a long-pass edge filter (*Omega Optical XF3095 ALP 700*). The Mie-signal was simultaneously imaged in the same way onto a second ICCD camera.

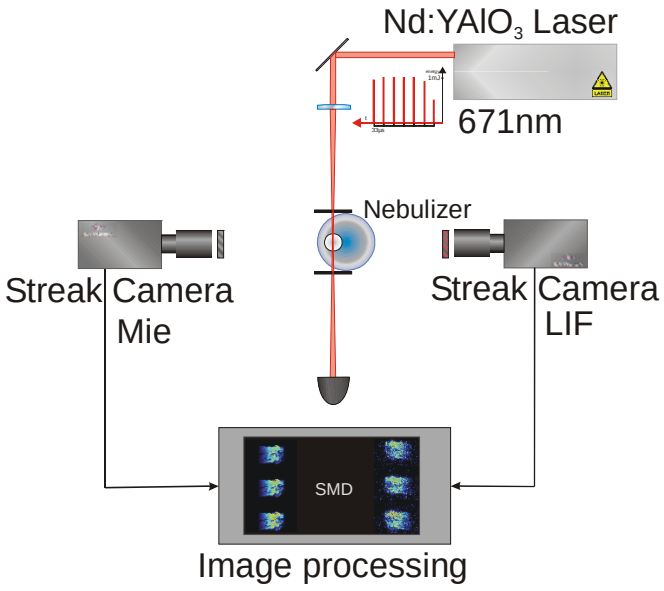

Fig. 5.39 Experimental setup for planar LIF and simultaneous Mie scattering measurements.

Fig. 5.40 shows typical single shot LIF and Mie-scattering images of the spray generated by the medical nebulizer. The droplet velocity as well as the evaporation rate in the observed spray was too low to give visible change in signal on the observed timescale ($\Delta t = 66$ µs). The LIF signal is separated from the scattered laser light by a long-pass filter with a total transmission of <1% for wavelengths < 700 nm. The LIF images were corrected for remaining scattered light and Diesel fluorescence background. Rhodamine 800 and Atto 680 were tested as a fluorescence tracer in Diesel. In both cases the tracer concentration was 2×10^{-6}mol/l. From the spectrometer measurements we expect the background fluorescence of the Diesel fuel to be less then 2% of the total fluorescence signal at this tracer concentration. The LIF signal from Atto 680 in the image experiments was stronger by an average factor of ~2 compared to Rhodamine 800 (Fig. 5.38).

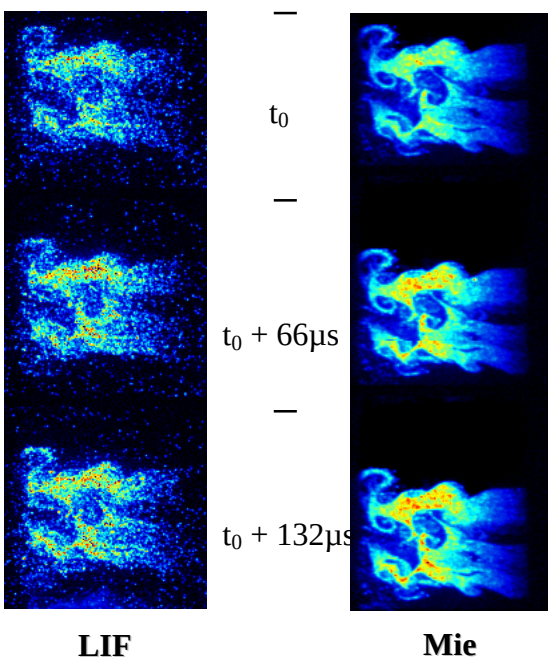

Fig. 5.40 Single-shot images of LIF signal (left) and Mie-scattering signal (right) of ethanol spray doped with Rhodamine 800 at a tracer concentration of c = 2.7×10^{-7} mol/l, simultaneously recorded and illuminated by three pulses selected from one burst of the Nd:YAlO$_3$ laser. The time difference between each pulse was 66 µs.

Fig. 5.41 shows a signal proportional to the local SMD in the nebulizer-spray, obtained by simultaneous measurement of LIF and Mie signal. The signal was averaged over 200 single shots. The images were corrected for special distortions caused by the camera optics and the image intensifier and carefully superimposed. PDA measurements on the same spray at three different positions were used to calibrate the SMD signal. There is good agreement in the local variation of the relative average droplet size measured across the field of view.

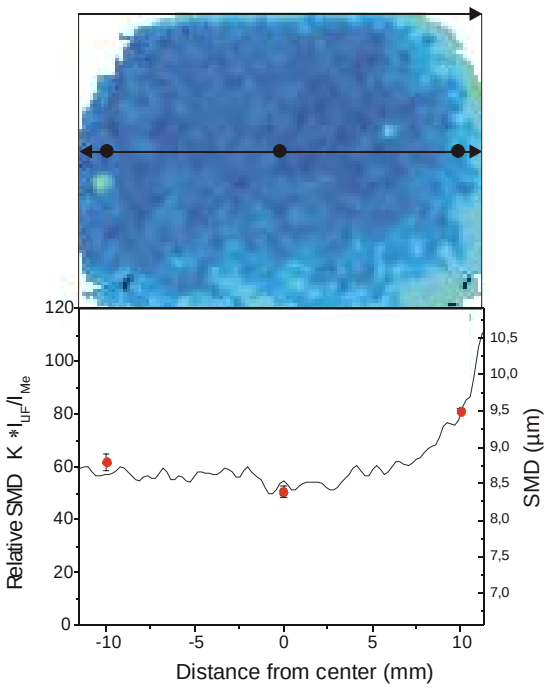

Fig. 5.41 Two-dimensional ($20 \times 20\ mm^2$) distribution of the Sauter Mean Diameter (SMD) in the Rhodamine 800-doped Diesel spray generated by a medical nebulizer. The lower plot shows a cross-section through the relative SMD field at ~ 10 mm downstream of the nozzle. The positions marked by the black dots were measured with a Phase Doppler Anemometer. The error bars indicate the uncertainty in the droplet diameter PDA measurement.

In this experiment spray, evaporation, and therefore, accumulation of the tracer inside the individual droplets could be neglected. When applying this method to a Diesel spray under more realistic conditions in terms of ambient temperature and pressure, evaporation of the spray must be considered. Rhodamine 800 can be assumed to accumulate completely inside the droplet so that the I_{LIF}/I_{Mie} ratio must be considered to be proportional to the initial – and not the actual droplet size. Late in the evaporation when the dye concentration exceeds a critical value (~1.0×10^{-2} mol/l for Rhodamine B solved in ethanol [110]) self-quenching effects must be considered. For the given starting concentration of 2×10^{-6}mol/l that means a droplet diameter reduction by a factor of 14 before self-quenching effects become significant (>1% signal loss, compare [5]). At higher concentrations self-quenching prevents further quantitative interpretation of the LIF signal.

5.2 Experiments in a Berkeley-type model spray burner

To test and to refine computational spray models the comparison with experimental results is essential. For that purpose an experimental system is needed that provides as much data as possible while being simple enough to enable a thorough numerical simulation of the system. In that way, model spray flows, as described in [111-113] and numerical simulation [114,115] complement each other – the experiments supply the required initial conditions for the simulation and can in turn be used to evaluate the quality of the mathematical models used for simulations. In this work experiments on a spray burner that fulfills the requirements as model system, were performed.

5.2.1 Burner details

The spray burner was developed in cooperation with the University of California at Berkeley [113]. It consists of a central fuel nozzle (Delavan 67700-5) and a perforated brass plate that provides a homogeneous air co-flow on top of the central burner bowl (see Fig. 5.42). The nozzle is located centrally 80 mm above the brass plate. The fuel mass flow through the nozzle is proportional to the square root of the injection pressure p_{inj}:

$$\dot{m} \propto \sqrt{p_{inj}} \tag{5.37}$$

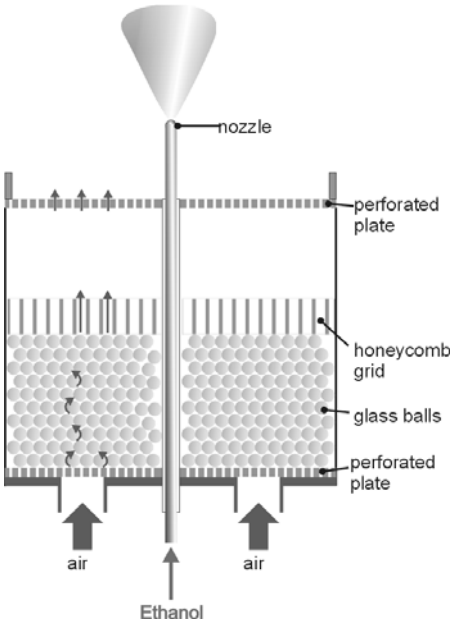

Fig. 5.42 Schematic set-up of the spray burner

The proportionality factor is called the Flow Number *FN* whose unit is $g/\sqrt{bar}\,s$ and which is equal to 0.33 [116].

$$FN = \frac{\dot{m}}{\sqrt{p}} = 0.33 \frac{g}{\sqrt{bar}\,s} \tag{5.38}$$

Before the fuel enters the burner bowl it passes through a heated coil at a temperature of 55°C. The heat is partially dissipated through the burner bowl, thus the fuel temperature at the nozzle is measured to be ~40°C. In the presented experiments ethanol was used as fuel. Ethanol has the advantage to be single-component and therefore has well-defined chemical and physical properties. This fact additionally simplifies the mathematical modeling.

In order to create well-defined boundary conditions for the spray flame the brass burner plate has approximately 2200 boreholes of 1 mm diameter each. Air flows through these holes as a co-flow of defined velocity. The burner bowl has a height of 200 mm and a diameter of 220 mm. The lower half of the bowl is filled with glass beads (∅ 9 mm) in order to homogenize the air flow. A 25 mm honeycomb grid above the glass beads aligns the co-flow in axial direction. The perforated brass plate forms the cover of the bowl.

The specific benefit of this burner geometry lies in the fact that a stable spray flame is generated without bluff-body or pilot flame stabilization which would require special mathematical treatment. Thus, from the point of numerical simulation, the two are decoupled and therefore far better insight is obtained. The initial design implied a reacting or so-called "vitiated" co-flow [113]. However, the burner in the Heidelberg laboratory was usually operated with a non-reactive (air) co-flow and liquid ethanol as fuel.

As first described in [116] two different flames could be stabilized, as shown in Fig. 5.43. One (a) is lifted by approximately 10 mm from the nozzle exit, the other (b) sits directly on the nozzle. Only type b) is stable with enabled co-flow. The pre-heating of the fuel, as described above, induced the transition from type a) to type b). The resulting flame has two flame zones. The inner flame is located 1 mm above the nozzle exit while the outer flame position depends on the fuel pressure. It is located 5 – 15 mm above the nozzle.

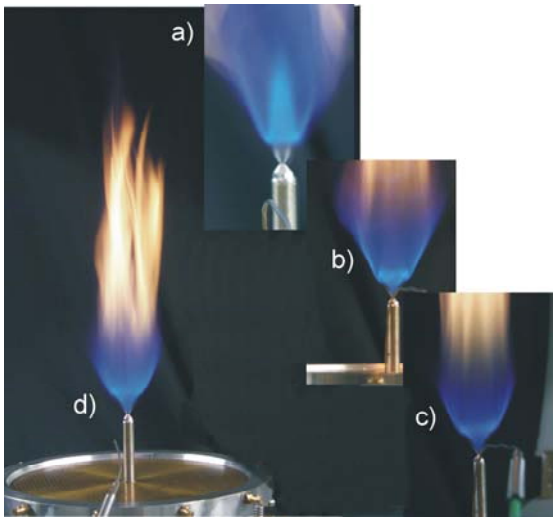

Fig. 5.43 Different types of flames at injection pressure p = 1.4 bar: Lifted flame without co-flow (a), non-lifted flame without co-flow (b), non-lifted flame with co-flow.

Injection pressures and resulting mass flows are listed in Tab. 5.4.

p [bar]	*dm/dt* [g/s]	*P* [kW]
1.4 ± 0.1	0.39 ± 0.01	11.7 ± 0.4
2.0 ± 0.1	0.47 ± 0.01	14.0 ± 0.4
2.6 ± 0.1	0.54 ± 0.01	15.9 ± 0.4

Tab. 5.4: Injection pressures p and corresponding mass-fluxes and thermal power P of the spray flame

Different co-flow fluxes were used. Tab. 5.5 shows the corresponding co-flow velocities.

Φ_H [m^3/s]	v_H [m/s]
0	0
40	0.32
80	0.64

Tab. 5.5: Volume flux Φ_H and corresponding co-flow velocities v_H.

Several experimental techniques have been applied to the spray flame of this burner over the recent years [116]. The burner provides 360° optical access and is therefore especially suitable for the application of laser-based experimental techniques.

Particle Image Velocimetry (PIV) was used previously to characterize the spray flowfield (see Fig. 5.44) [116].

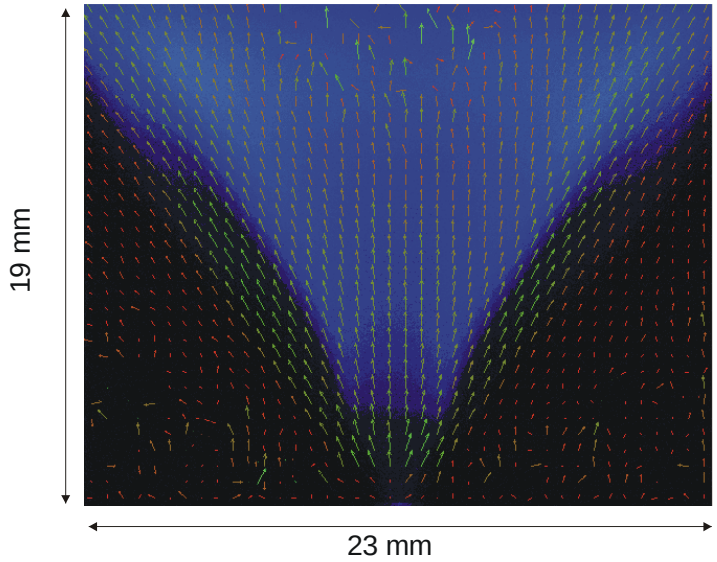

Fig. 5.44 Overlay of chemoluminescence and the velocity field of the non-lifted flame with co-flow. The nozzle is located 3 mm below the image.

From the measured mean droplet velocity the geometric Reynolds number[2] Re = 9,565 of the flow could be calculated.

5.2.2 Preliminary work

For evaluation of a spray model developed by Ge et. al. [36] at the Interdisciplinary Center for Scientific Computing in Heidelberg (IWR) the initial conditions of the spray burner were needed. For that purpose droplet-size and droplet-velocity distributions were measured for the non-reacting spray without co-flow close to the nozzle exit where the differences between reacting and non-reacting case are expected to be small. Droplet sizes and velocities were measured by Phase Doppler Anemometry (PDA). As described in section 4.3.2 PDA gives reliable results for sizes and velocities of spherical droplets in relatively dilute sprays. The size and velocity distributions are obtained by measuring a high number of droplets (4000 – 15000) at each measurement position. The PDA setup for this experiment used only one pair of intersecting laser beams and therefore measured only the axial droplet velocity component of the spray droplets. An estimation of the radial velocity component can be geometrically calculated from the known spray angle (45 ± 5°) and the measurement position [25].

Close to the nozzle this approximation is justified and verified by older PIV measurements in the reactive spray [116].

[2] The geometric Reynolds number is defined as $Re = v \cdot l \cdot \rho \cdot \eta^{-1}$, where v is the flow velocity, l the characteristic length scale, ρ the density and η the dynamic viscosity.

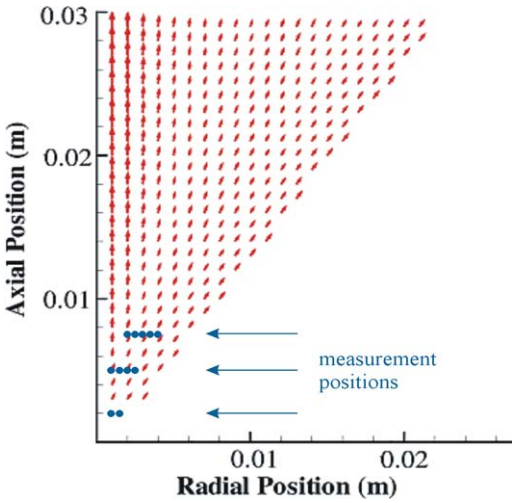

Fig. 5.45 Vector plot of the ensemble-averaged droplet velocities. Marked points indicate the PDA measurement positions (from [36]).

The simulations address the experimental condition with injection pressure p_{inj} = 2.0. Fig. 5.45 shows the vector plot of the ensemble-averaged droplet velocity simulated by Ge [37]. The marked points indicate the location of the measurements. The first section where experimental data is available is x = 2 mm is taken as the inlet profile for the computation.

PDA measurements closer to the nozzle were not possible because the droplet breakup process is not actually completed until up to ~5 mm above the nozzle (see Fig. 5.46) and the encountered liquid filaments can not be captured by the PDA which is limited to spherical particles.

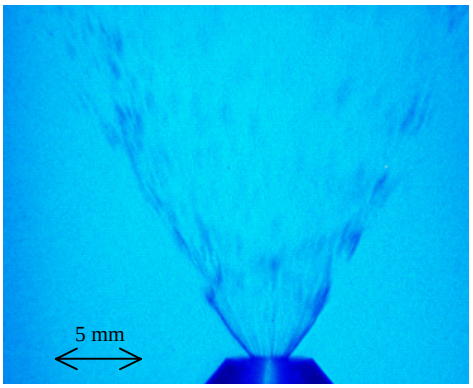

Fig. 5.46 Photograph of the ethanol spray.

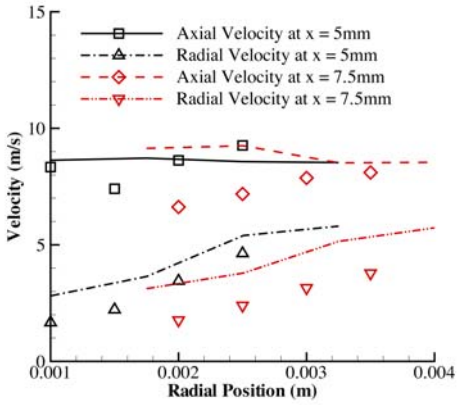

Fig. 5.47 Radial profiles of the ensemble-averaged droplet velocities (non-reactive) at sections x = 5 mm and 7.5 mm above the nozzle. Symbols: experimental data; lines: simulation (from [36]).

Fig. 5.47 shows the comparisons of experimental and numerical results of the ensemble-averaged droplet velocity at the two different axial positions x = 5 mm and 7.5 mm; Fig. 5.48 displays the comparison of the Sauter mean radii for the same locations.

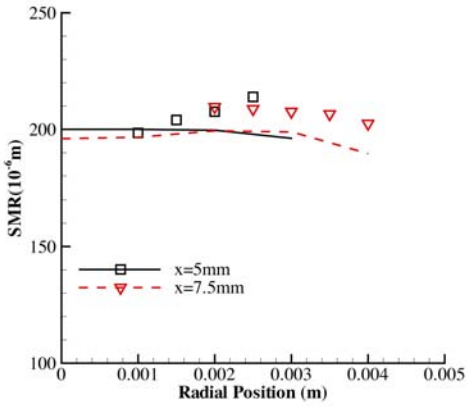

Fig. 5.48 Radial profiles of the Sauter mean radius at sections x = 5 mm and 7.5 mm. Symbols: experimental data; lines: simulation (from [36]).

The discrepancies between experiment and simulation in the droplet velocities can be attributed to the inaccurate approximation of the radial droplet velocity, unknown initial gas flow properties for the simulation, and the coarse initial droplet size distribution in the experiment. All spray calculations are very sensitive to the initial conditions of both the gas and the liquid phase. The experimental data of the droplet distribution at x = 2 mm have a coarse spatial resolution in radial direction (0.5 mm). Therefore, there is some ambiguity in determining appropriate initial conditions for the computations. Moreover, the PDA measurements discard droplets that deviate from spherical symmetry. The simulated values of the droplet velocities are systematically higher than the measured values by up to 30%. This causes a higher droplet evaporation rate leading to smaller droplet radii compared to the experimental values by up to 10%.

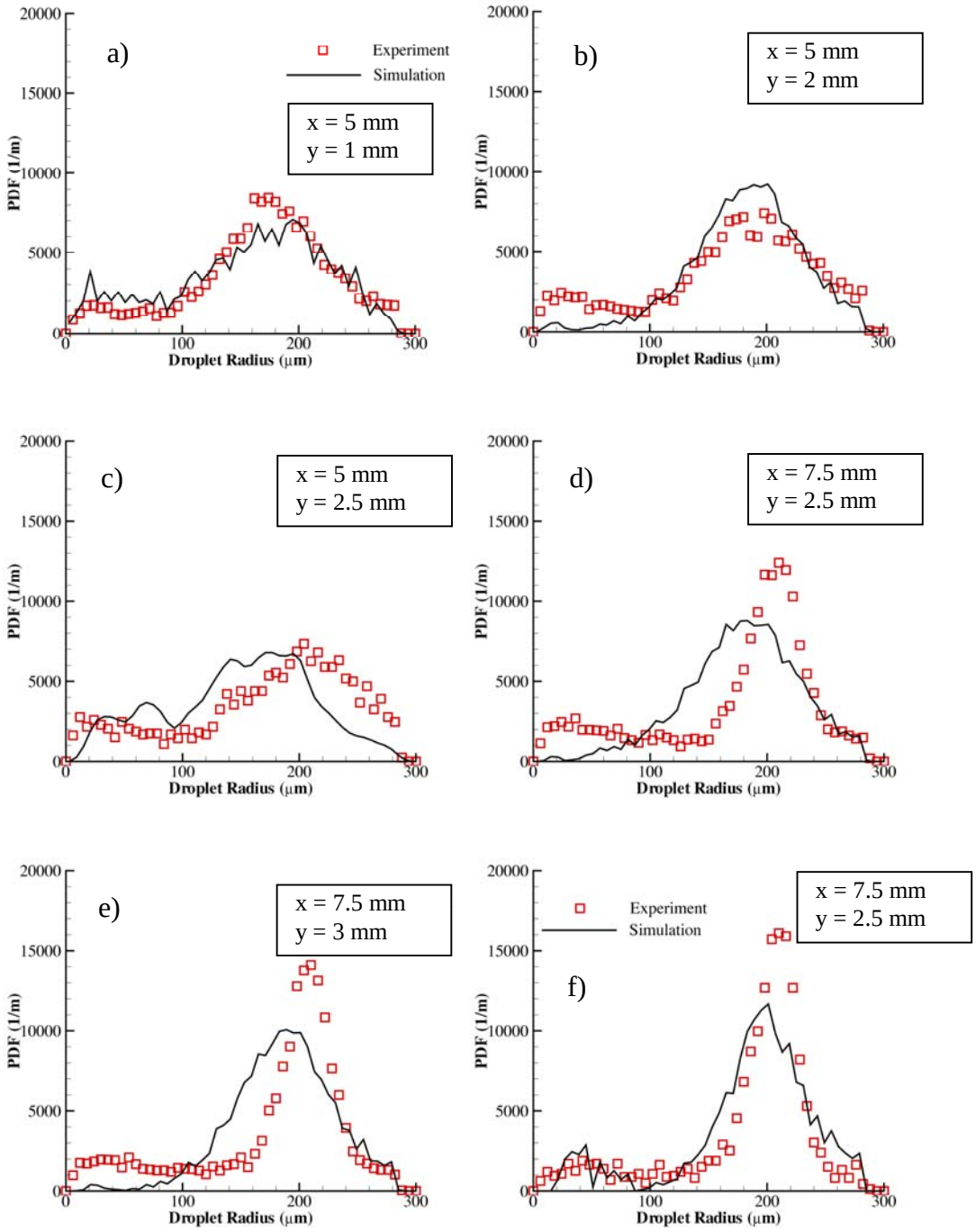

Fig. 5.49 Comparison of measured and simulated droplet size distributions at different positions in the spray. x denotes the vertical distance from the nozzle exit, y the radial distance from the central axis (from [36]).

Fig. 5.49 shows the comparison of droplet size distributions from the numerical simulation and the experiment. The droplet size distributions at the positions indicated in Fig. 5.45 are illustrated. The size of the droplet radii varies from 0 to 300 µm.

In the present computation, the whole range is split into 50 equally-sized intervals. The number fraction of each interval is calculated and then the PDFs of droplet radii are

evaluated. In general, the numerical results agree reasonably well with experimental data. Comparing the sections at x = 5 mm and 7.5 mm, the peak values of droplet size distribution shift towards large droplet radii, which indicates the progress of vaporization. The probability of small droplets at the position (x = 5 mm, y = 2 mm), (x = 7.5 mm, y = 2.5 mm), and (x = 7.5 mm, y = 3 mm) and the droplet sizes with high probabilities in the section x = 7.5 mm are under-predicted (Fig. 5.49. d-f). This may result from an imprecise estimation of the gas velocities at the inlet profile. The gas flow plays an important role in droplet evolution. Especially in the downstream regime, the time scale of the gas-liquid interaction suggests that its effect may not be neglected. The radial velocity component that has been calculated geometrically using the spray angle causes an uncertainty in the calculations that can partially explain the discrepancies.

5.2.3 Temperature measurements in the spray flame

5.2.3.1 Surrounding gas-phase temperature

Imaging of the gas-phase temperature in the spray flame has been performed based on multi-line laser-induced fluorescence measurements with seeded NO as described in section 4.3.3.6. The details of this experiment are not topic of this work, further information can be found in [117]. For the sake of completeness some results of the measurements of the gas phase temperature in the spray flame shall be presented here.

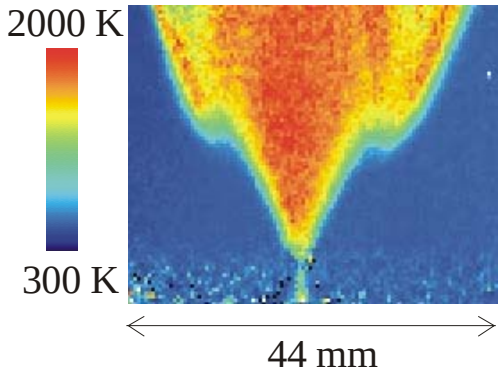

Fig. 5.50 Temperature distribution in the ethanol spray flame at 2.0 bar injection pressure and 0.32 m/s air co-flow.

Fig. 5.50 shows the gas-phase temperature field at a typical operation condition of the burner (p_{inj} = 2.0 bar, v_{Co} = 0.32 m/s) in a 44 × 36 mm^2 area of the flame above the nozzle. The nozzle exit is visible in the middle of the lower part of the image. Maximum temperatures are 1800 ±60 K (±3.3%) in the inner flame. Temperatures in the co-flow are 300 ±10 K (±3.3%). The spatial resolution is 0.4 × 0.4 mm^2.

The simulated gas-phase temperature field, as published in [118] reproduces the measured temperatures quite precisely but fails to show the detailed structures, such as the hot wings of the flame.

5.2.3.2 Liquid-phase temperature

The liquid-phase temperature was characterized by means of the fluorescence of the temperature-sensitive laser dye *Rhodamine B*. The theoretical background of the method is described in section 4.3.3.5. The molecule has two free diethylamine groups that cause the strong temperature sensitivity by an increased rate of internal conversion at higher temperatures. The molecular structure is shown in Fig. 5.51.

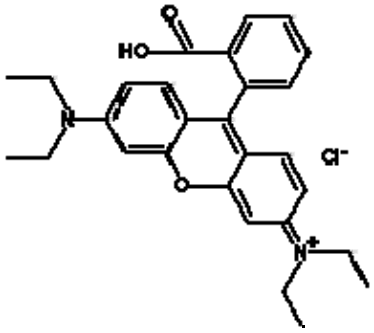

Fig. 5.51 Molecular structure of the Rhodamine B molecule($C_{28}H_{31}N_2O_3Cl$, MW: 479.02). The strong temperature dependence originates from the two freely rotating diethylamine groups.

Spectral characterization

Rhodamine B shows a broad absorption band at around 550 nm. Therefore, a frequency doubled Nd:YAG laser at 532 nm can be used as excitation light source. The fluorescence of Rhodamine B shows a Stokes shift of about 25 nm. Spectra are shown in Fig. 5.52.

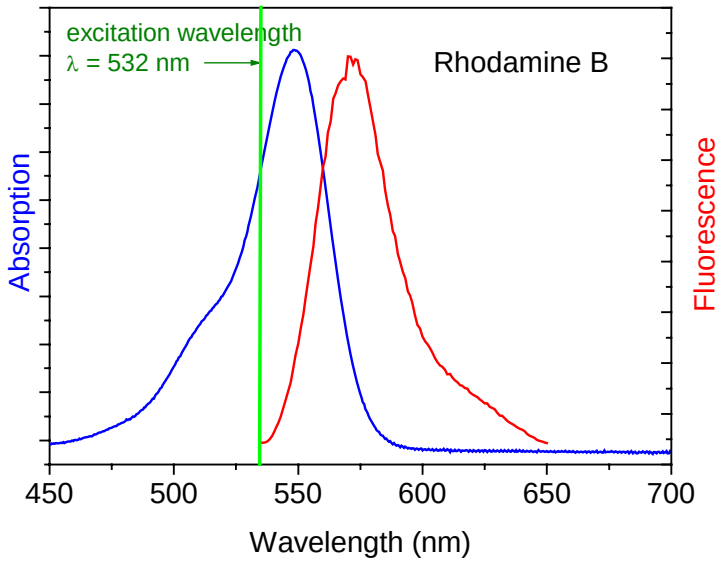

Fig. 5.52 Normalized absorption and fluorescence spectra of Rhodamine B solved in ethanol. The excitation wavelength was set to 532 nm.

Taking spectra at varying temperatures demonstrates a distinct temperature dependence of the overall fluorescence intensity.

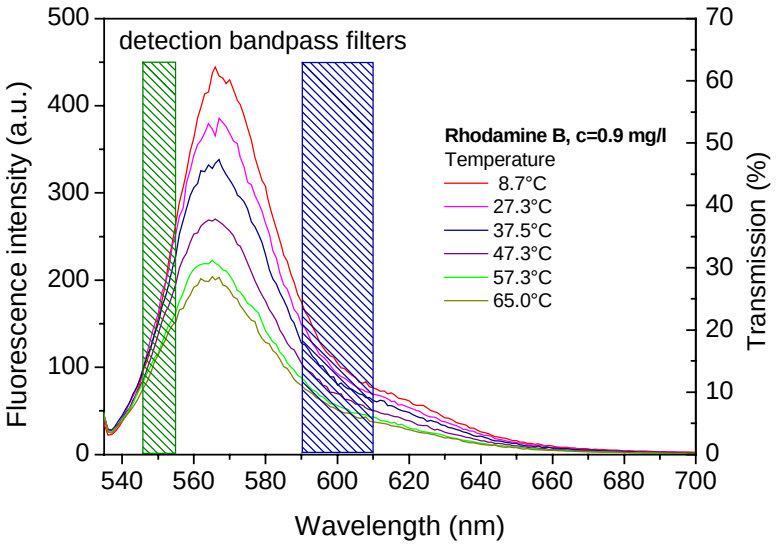

Fig. 5.53 Temperature dependent Rhodamine B LIF-emission spectra in ethanol. The hedged areas denote the transmitting wavelength regime of the optical filters used for the 2D-temperature measurement.

LIF emission spectra at temperatures between 282 and 340 K were measured using a *Varian Cary Eclipse* UV-Vis spectrometer (See Fig. 5.53). The concentration was chosen after checking for saturation and self quenching effects to $c = 2.5\times10^{-6}$ mol/l (1.2 mg/l). At this concentration excitation trapping or reabsorption of fluorescence light in the droplets should not be relevant. Calculations showed that the effect on the overall intensity and spectral shape does not exceed 0.5% for 200 µm droplets. In the 550 nm region, the effect causes a signal reduction of 1.2%.

Similar calculations showed that the application of a standard 10 mm cell in the spectrometer would cause an error in the overall intensity of 10% and of 25% in the 550 nm region. Therefore, the calibration was done using a thin layer cell (see section 5.1.2) which reduces the error to max 1.8%.

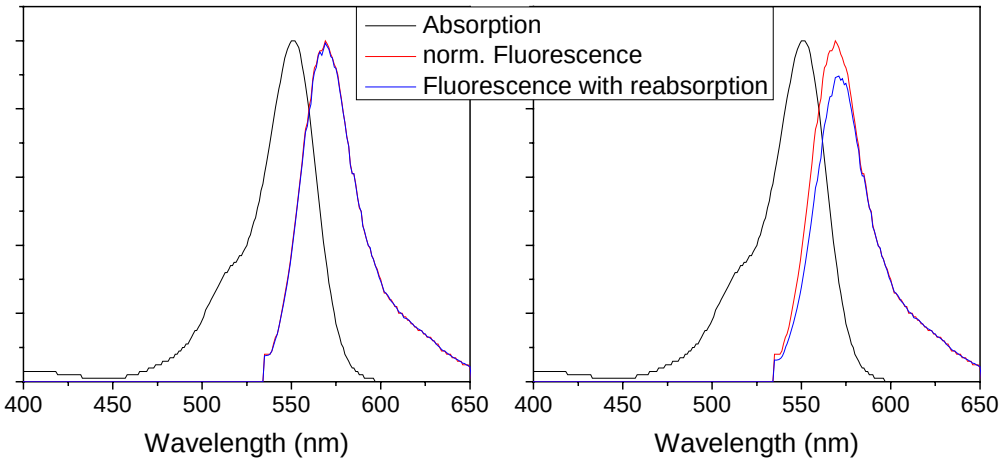

Fig. 5.54 Reabsorption of fluorescence light in a Rhodamine B solution of c = 2.5× 10^{-6}mol/l in a thin-layer cell (left) and a standard 1 cm cell (right).

According to (4.24) the temperature sensitivity itself is wavelength dependent and a sensitivity coefficient can be calculated for each wavelength from the spectra. In general, to obtain the spectral temperature sensitivity coefficient $\beta(\lambda)$ the logarithmic intensity ratio at each temperature is plotted against $\left(\frac{1}{T_0}-\frac{1}{T}\right)$, where T_0 is a chosen reference temperature. The sensitivity coefficient β can then be obtained by determining the average gradient of the rising curve. In that way β is calculated for every wavelength in the fluorescence spectrum. Negative β indicates an increase, positive β a decrease of the fluorescence intensity with increasing temperature. The objective is to find two wavelength regions that, while both showing high overall fluorescence intensity, have a preferably high difference in β.

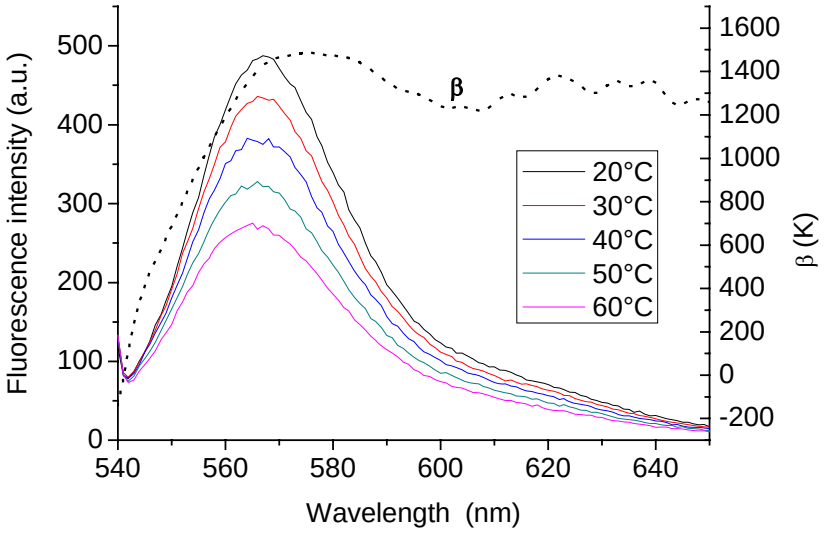

Fig. 5.55 Spectra of Rhodamine B in ethanol taken at varying temperatures in a thin layer cell. The dotted black line is the sensitivity parameter β.

It turns out that, two bandpasses at 550 ± 5 nm and 600 ± 10 nm (filter transmission curves, see Fig. 5.56) show similar overall intensities, a good difference in β and adequate spectral separation to avoid cross-talk phenomena. The difference in β is determined from the spectral analysis to be $\Delta\beta = 400 \pm 45$K. In the literature higher sensitivities are reported [5] for excitation of Rhodamine B with an Ar^+-laser at 514 nm.

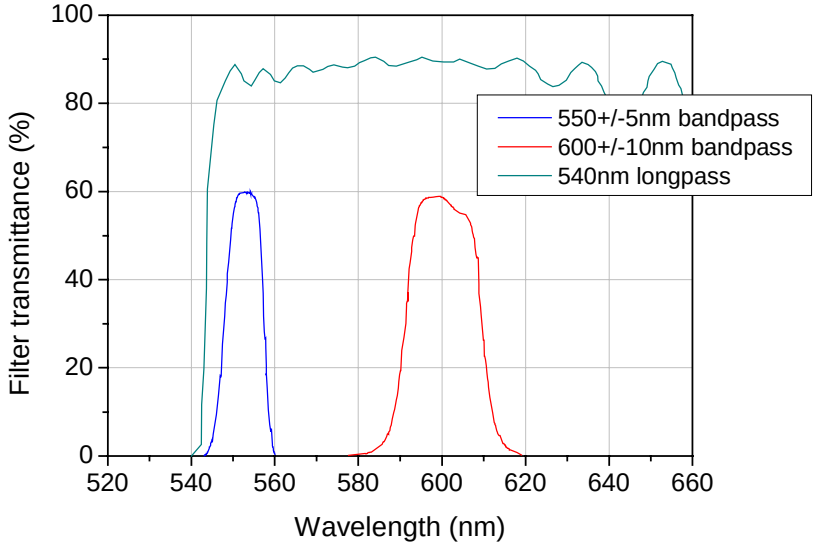

Fig. 5.56 Transmission curves for the optical filters used in the two-color LIF thermometry experiment.

Experimental setup

For this work a frequency-doubled Nd:YAG laser at 532 nm was considered to be better suited because of the available high pulse energies and short pulse durations of ~9 ns that allow snap-shot imaging even in turbulent environments like a spray flame. Fig. 5.57 shows the experimental setup schematically. The beam of the Nd:YAG laser was formed into a thin (~500 µm) light sheet by two cylindrical lenses ($f = -40$ mm and $f = 500$ mm). Two intensified CCD cameras were set up perpendicularly to the light sheet. The fluorescence signals from the Rhodamine B (2.5×10^{-6} mol/l) doped spray were imaged by two Nikon $f = 105$ mm, $f_{\#} = 2$ macro lenses, each equipped with the appropriate set of optical filters onto two CCD cameras (*LaVision StreakStar*). In addition scattered laser light is suppressed by a 540 nm longpass filter (*Omega Optical*, also shown in Fig. 5.56). The cameras were synchronized to the laser system as well as to each other. Series of images were recorded for several burner operating conditions. To minimize the detection of chemiluminescence from the flame, the exposure time was set to 0.5µs.

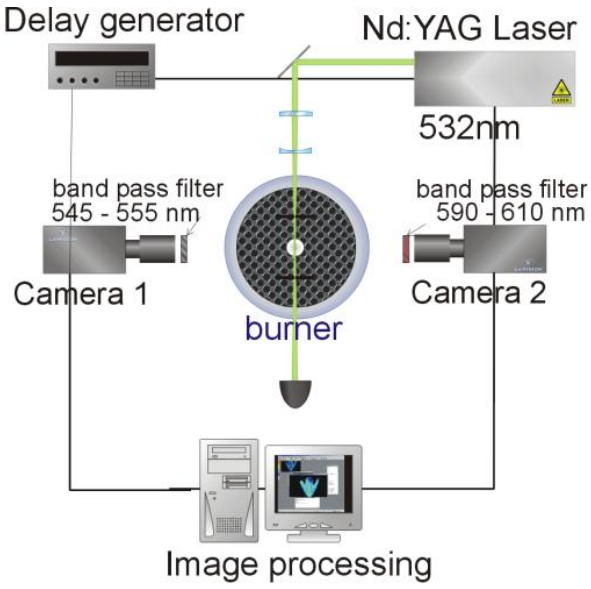

Fig. 5.57 Experimental setup for spray temperature measurement by two-color LIF.

Calibration and data analysis

The liquid-phase temperature field in the spray was computed from the ratio of the two detected spectral regions according to equation (4.30). The calculation of the ratio from the two simultaneously recorded images requires thorough correction of image distortion and careful mapping of both images. Then the ratio from the single shot images can be taken and averaged over a multitude of image sets. Typically 200–400 image sets were taken. The implemented algorithm also included a test for congruity of the two images in order to exclude and correct for glitches in the camera synchronization. A mask is applied to each single image that sets the pixel values in

between the droplets to zero. From a series of images, the average is then calculated while accounting for the number of non-zero events for each individual pixel.

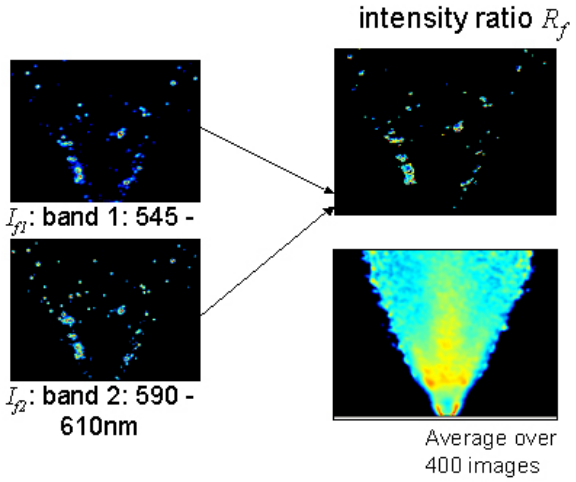

Fig. 5.58 Processing of the spray images: After correction for distortion, the single shot images from both spectral bands are mapped, the ratio is calculated and an average over 200-400 images is formed. See text for details.

For the determination of absolute temperature values from the ratio image one calibration point in the image with known temperature is required within the observed area. For this purpose the spray temperature was measured with a K-type thermocouple directly at the nozzle exit. The temperature at this point is taken as calibration temperature T_0. The corresponding LIF intensity ratio of the two detection bands is $R_f(T_0)$ (see equation (4.30)). That spatial point was identified in the spray LIF images and the LIF signal ratio at that point was used for calibration.

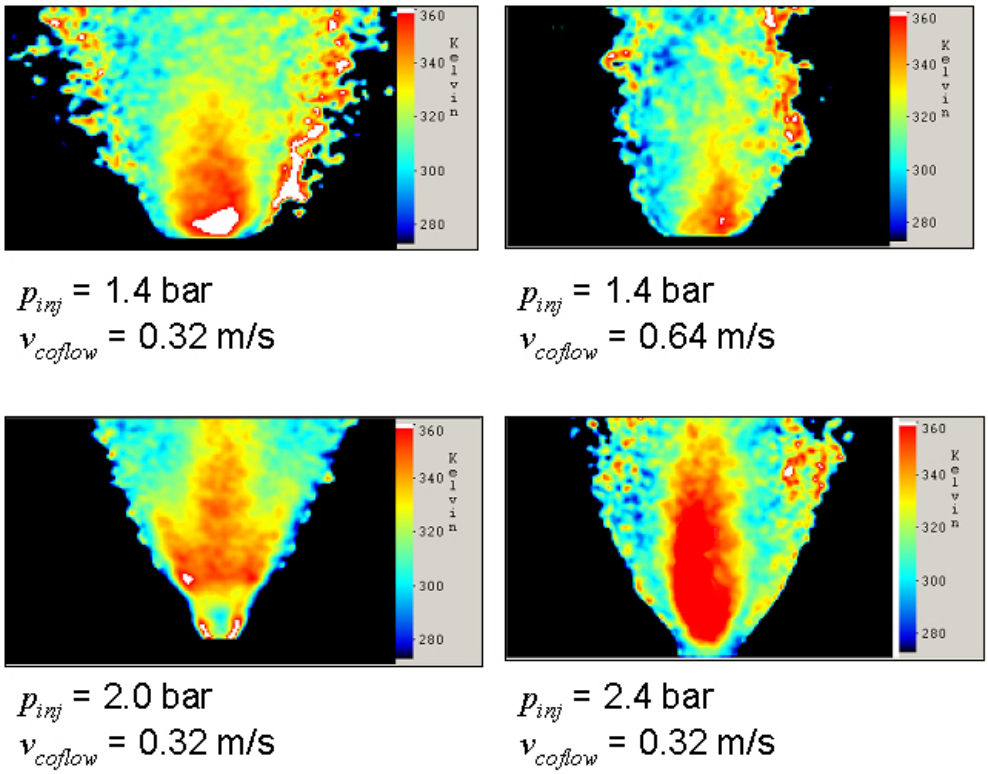

Fig. 5.59 Liquid-phase temperature fields for the ethanol spray flame at different injection pressures and co-flow velocities.

Fig. 5.59 shows temperature fields for four different burner conditions. The images represent averages over 250 images. Apart from the varying flame shapes the temperature distributions are qualitatively similar: There is a hot zone in the center of the hollow-cone spray and hot regions at the edges, where most of the liquid is present. Further down-stream, the droplets tend to be cooler which can be attributed to evaporative cooling. The temperatures vary from boiling point temperature down to 310 K. The white areas in the temperature field denote measured temperatures above the boiling point of ethanol. This effect is due to the uncertainty in the identification of the spatial location of the calibration point within the LIF images (±3–4 Pixel^2). An analysis of the sensitivity of the measurement to the calibration point location yielded that this sensitivity is quite high. It results in a temperature uncertainty of 10–15%. Additional uncertainties result from the measurement of the calibration temperature with the K-type thermocouple, which might not yield the true liquid temperature of the droplets at the calibration point but the temperature of the evaporating liquid film on the thermocouple tip. Thus, the total uncertainty, also considering the error of ~10% in $\Delta\beta$, of the measurement is ~20%.

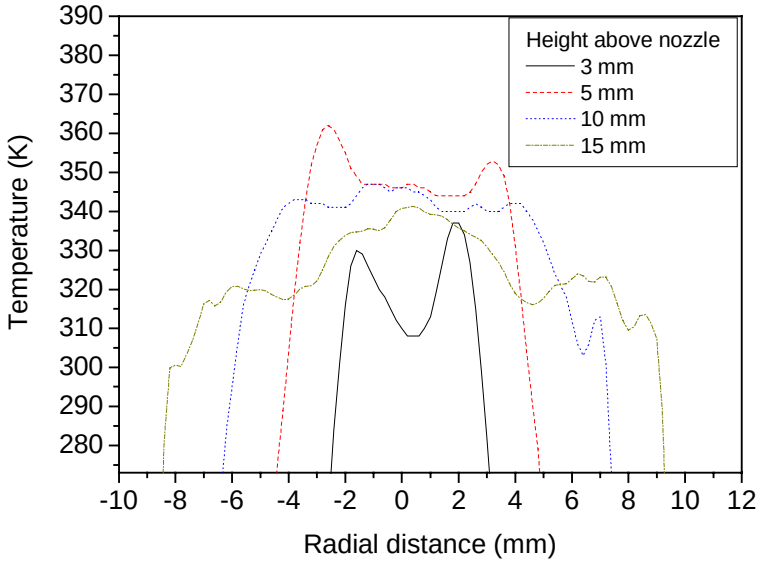

Fig. 5.60 Temperature profiles for the flame at 2.0 bar injection pressure and 0.32 m/s co-flow velocity.

Fig. 5.60 shows temperature profiles in the flame at p_{inj} = 2.0 bar and v_{coflow} = 0.32 m/s for different heights above the nozzle. The hot outer edges of the flame are clearly visible. Farther away from the nozzle the center of flame is heated up and shows a hot plateau. The comparison of the liquid-phase and gas-phase temperature fields (measured by Kronemayer et al. [117,119]) shows agreement of the hot zones' locations in liquid and gas phase (see Fig. 5.61).

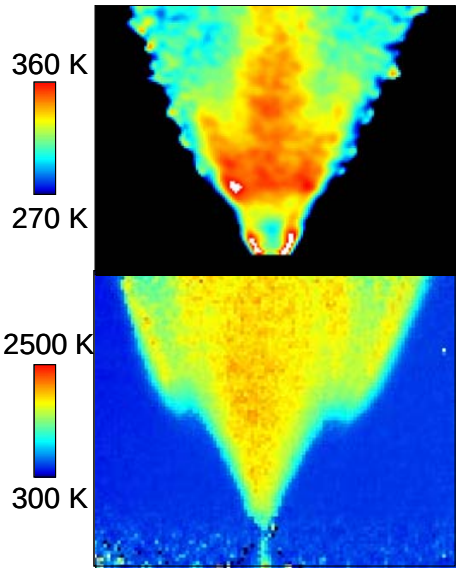

Fig. 5.61 Comparison of liquid and gas phase temperatures for p_{inj} = 2 bar and $v_{co\text{-}flow}$ = 0.32 m/s [67].

Although the temperature resolution of the two-color LIF method at the given excitation wavelength is not optimal, the used laser/filter combination allowed the application of the method in a reactive spray-flame environment.

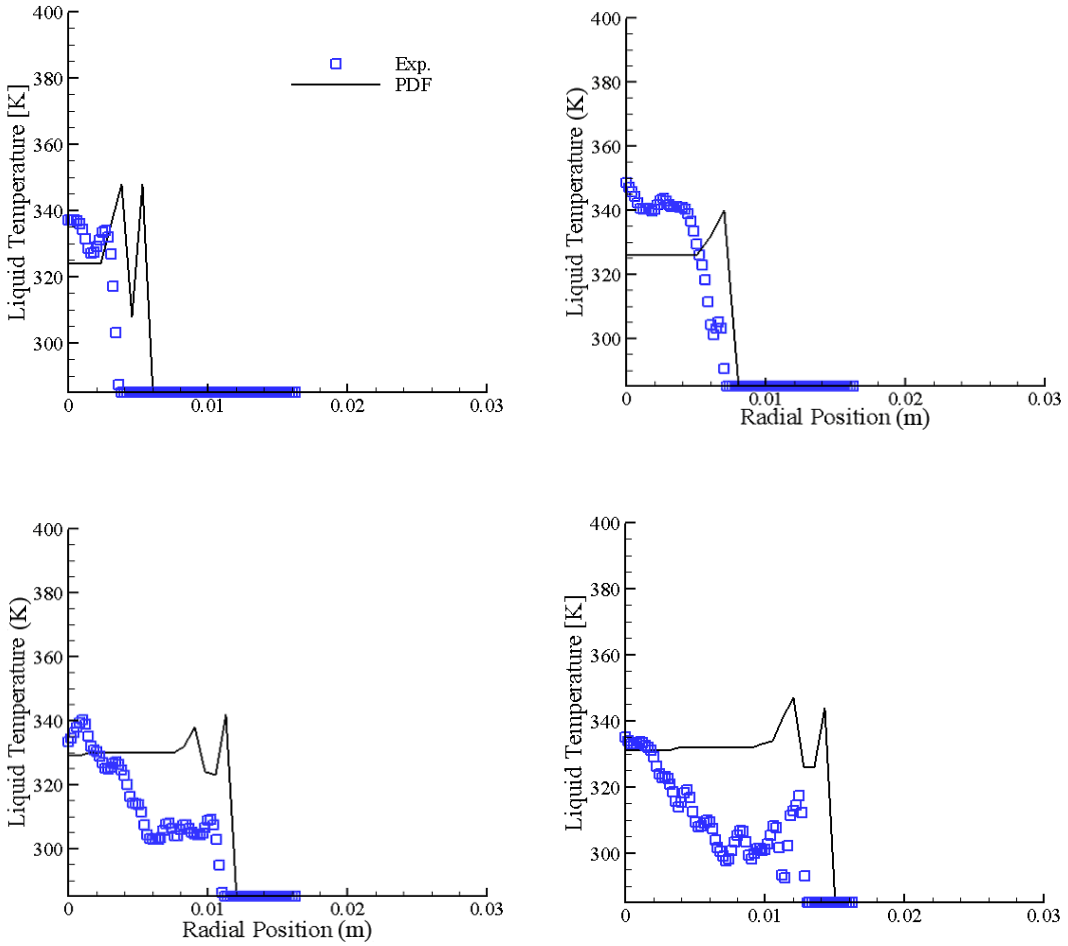

Fig. 5.62 Comparison of experimental and computational results for the liquid phase temperature from [120].

The liquid temperature was modeled by Ge [120] using a discrete droplet model (DDM). The *Uniform-Temperature Model* (infinite conductivity) model [23] and the *Abramzon and Sirignano model* [121] are used to compute the droplet temperature and evaporation rate. Both of the measured and simulated results are weighted with droplet surface area. The numerical simulation gives reasonable prediction of the experimental results. The predicted spray is broader than the measurement, which is due to the coarse measurement of droplet size distribution and droplet velocity distribution at the inlet boundary. The liquid-phase temperature near the axis is under-predicted, because the radiation heat transfer is neglected in the present simulation.

Fig. 5.62 shows the radial profiles of liquid-phase temperature at various heights above the nozzle: x = 6mm, 10mm, and 20mm. Symbols are the measurement. Close to the nozzle (c.f. the section x = 6mm), there is a valley in liquid-phase temperature near the spray edge. The droplets inside the flame are heated by the surrounding hot gas. Thus, the droplets close to the axis have relatively high temperature. The droplet temperature decreases with increasing radial distance, because the gas temperature decreases and the

droplet evaporation consumes part of the energy. Further increasing the radial distance, the droplet evaporation becomes very weak. Consequently, the heat taken away by the vapor is small. Therefore, the droplet temperature increases and reaches the peak right before the spray edge. Such a phenomenon is insignificant at the section x = 10mm according to the measurement, as the expanding inner flame heats the droplets. At the section x = 20mm, the profiles of the liquid-phase temperature show two peaks again. This is due to the outer flame existing near the spray edge. The outer flame heats the droplets inside it, which leads to the second peak in the profile of liquid-phase temperature. The numerical simulation well predicts the two-peak phenomenon. The liquid-phase temperature at higher radial position is over-predicted. One possible reason for the discrepancies between experiment and simulation is that in the experiment, the laser does not illuminate the larger droplets homogeneously but is focused by the curved droplet's surface [73]. As a result, much of the fluorescence is emitted from near the droplet surface which is not necessarily at the average droplet temperature (which is calculated in the simulation). The evaporation process cools down the droplet surface, which leads to lower temperature at the surface than the averaged droplet temperature. In the simulation, the infinite conductivity model assumes homogeneous temperature distribution inside the droplets. This may additionally contribute to higher numerical droplet temperatures compared to the experimental values in the outer spray regions.

Applicability of two-color LIF thermometry in real fuels

The applicability of the two-color LIF-thermometry technique based on Rhodamine B in combination with realistic gasoline was investigated in spectroscopic measurements. This study assumes an experiment in an optical gasoline direct-injection engine that uses a copper-vapor laser (see 4.4.1.3) rather than the Nd:YAG laser as excitation source. The motivation is the opportunity to observe temporally-resolved high-speed movies in single engine cycles due to the high repetition rate of this laser type (up to 18 kHz). The copper vapor laser (green line) is operating at 511 nm where the absorptivity of Rhodamine B is reduced to 51% relative to 532 nm. However, the better spectral separation of excitation (and hence, scattering) and fluorescence allows a filter combination, which results in an overall higher temperature sensitivity.

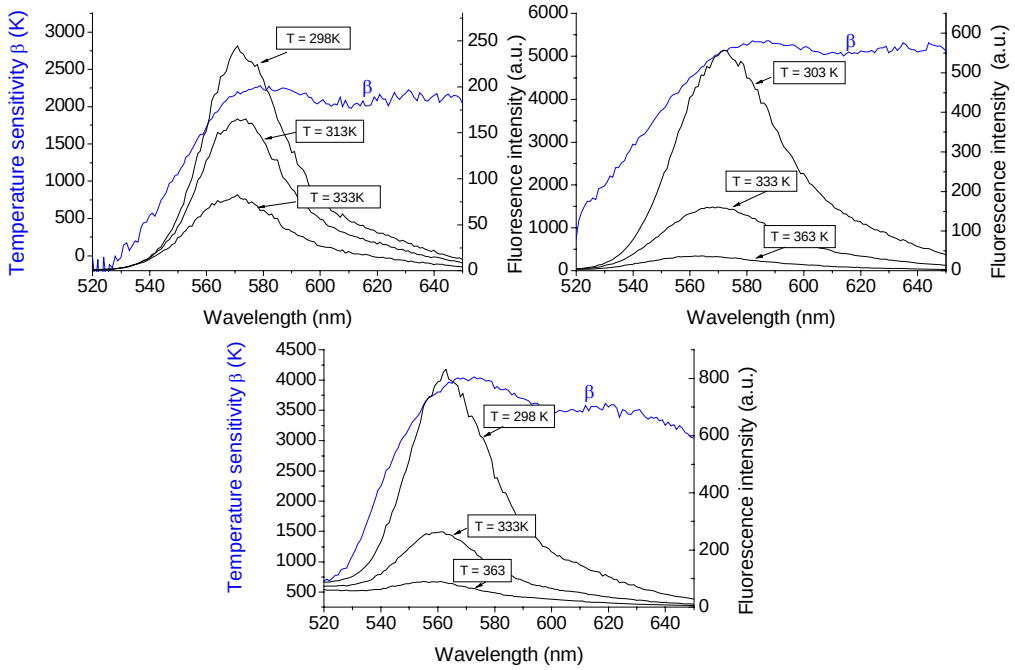

Fig. 5.63 Emission spectra of Rhodamine B, solved in pure ethanol (top left), isooctane (top right), gasoline(bottom) and temperature sensitivity coefficients (blue line). The excitation wavelength was set to 511 nm (corresponding to a copper-vapor laser).

The fluorescent tracer was dissolved in isooctane and in real gasoline respectively while ethanol was used in both cases as “detergent”. The ethanol fraction was kept to 10% - a value that corresponds to the ethanol fraction in some gasoline mixtures [122]. The tracer concentration was fixed to 2.5×10^{-6} mol/l (in respect to the overall mixture). Emission spectra at various temperatures were measured with a UV-vis photospectrometer (*Varian Cary Eclipse*). The results are shown in Fig. 5.63.

It is evident that not only the temperature sensitivity of the fluorescence but also the spectral shape strongly depends on the solvent. In the spectra taken in gasoline a slight fluorescent background is visible. Nonetheless fluorescence up to $T = 363$ K is strong enough to detect. Therefore, the application of this method in a fuel spray should be possible.

5.3 Experiments on single Droplets

5.3.1 Concepts for single droplet experiments

The experimental validation of evaporation models holds some practical challenges, caused mainly by the small droplet sizes involved in realistic systems. (For instance, the Sauter Mean diameters in a direct-injected Diesel spray are usually smaller than 20 µm.)

The task is ideally, to produce a droplet of defined size and keep it in a controlled atmosphere at a defined location for its entire lifetime.

Several methods to achieve this goal have been discussed and tested in the past. See, e.g. [42,123,124]. Some techniques that were applied for this work shall be discussed in more detail.

5.3.1.1 Fiber-suspended droplets

A very simple method is to suspend the droplet on a thin glass fiber for the time of the measurement. Different fiber arrangements are possible. In preliminary studies, a two-fiber arrangement was used: A vertical fiber to set the initial position of the droplet and a horizontal fiber to additionally fix it and prevent "creeping" of the droplet due to change in the equilibrium between adhesion and gravitational forces during the evaporation process.

This method is only applicable for comparably large droplets (500 µm – 1 mm) and due to the fibers the droplet shape is distorted. Liquids with a low specific surface tension show a stronger deviation from the spherical shape.

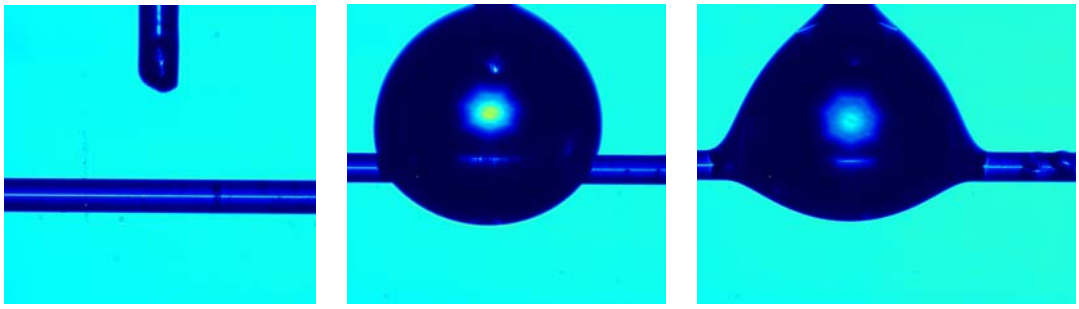

Fig. 5.64 Backlit image of the fiber arrangement and an attached droplets. Middle image: water droplet, right image: Ethanol droplet.

Fig. 5.64 shows backlight images of the described fiber arrangement (left) a suspended water droplet and a suspended ethanol droplet. The images were taken with a high resolution CCD-camera (LaVision Flowmaster).

The droplet shape is determined by the Laplace-Young Equation

$$\Delta P = P_{in} - P_{\infty} = \sigma\left(\frac{1}{r_1} + \frac{1}{r_2}\right) \tag{5.39}$$

where P_{in} is the internal pressure, P_{∞} the pressure of the surrounding atmosphere, σ the surface tension and r_1 and r_2 the radii of curvature at each point of the droplet surface [124]. As can already be observed in the figure, the disadvantages of this method lie in the distortion of the droplet shape and the consequent limitation to liquids with a highsurface tension. A further the limitation is the large initial droplet size (~1 mm in

this case). Various experiments on the evaporation of suspended droplets were presented in [70].

5.3.1.2 Electrodynamic levitation

In order to study single droplets under more realistic conditions, contact-free fixation of the droplet is necessary. One possibility to achieve "levitation" of an electrically charged droplet is to trap it in an strong electric field. Most liquids carry at least small amounts of free charges in form of ions and can therefore be charged and trapped in a high frequency electric quadrupole field. This method to trap small charged particles was introduced by Wolfgang Paul and Hans Dehmelt [125] in the 1950s who were able to trap single ions in an oscillating quadrupole field (the first “Paul”-trap).

In order for a charged particle to be trapped in an electric field a binding force must act on the particle:

$$F = -cr \tag{5.40}$$

This results in a hyperbolic potential Φ (given in Cartesian coordinates):

$$\Phi \propto ax^2 + by^2 + cz^2 \tag{5.41}$$

The potential of an electric quadrupole fulfills this requirement:

$$\Phi = \frac{\Phi_0}{2r_0^2}\left(ax^2 + by^2 + cz^2\right) \tag{5.42}$$

The Laplace equation $\Delta\Phi = 0$ imposes the condition $a + b + c = 0$. A simple way to satisfy this condition is obtained when $a = b = 1$ and $c = -2$. This results in a potential

$$\Phi = \frac{\Phi_0}{r_0^2 + 2z_0^2}(r^2 - 2z^2) \tag{5.43}$$

with $r_0^2 = 2z_0^2$ (Given in cylindrical coordinates).

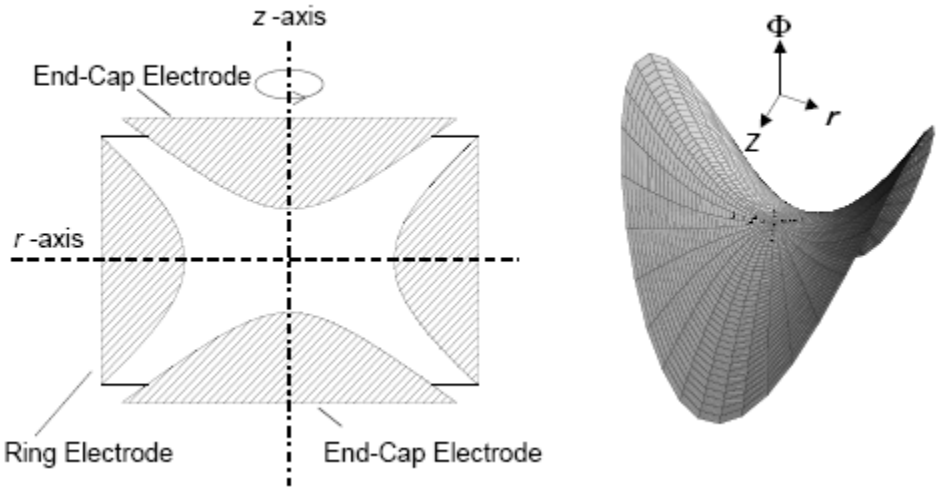

Fig. 5.65 Left: schematic of the original Paul-trap. Right: The static potential in the trap [126].

Fig. 5.65 (left-hand side) shows the electrode configuration of the first ion trap built by Wolfgang Paul. It consists of an hyperbolically shaped ring and two hyperbolic rotationally symmetric caps. The potential in an electrode configuration like that has a saddle-shape as shown in Fig. 5.65 (right-hand side). In case of a static potential there is no stable position for the particle as can be seen in Fig. 5.65. However, if an alternating voltage

$$\Phi_0 = U + V\cos\omega t \tag{5.44}$$

is applied between the caps and the ring electrode, the oscillating part of the voltage will cause – graphically speaking - the saddle-shaped potential to rotate perpendicular to the *z*-axis and therefore stabilize the particle in the center. Detailed calculations of the acting forces and the stability of such an electrodynamic trap can for instance be found in [125,126]. It should be noted that for a given trap geometry and given parameters *U*, *V* and ω stable trapping is only possible for particles in a certain charge-to-mass ratio regime determined by the equations of motion (Mathieu equations, see [125])

Easier electrode configurations are thinkable if the aim is to trap larger particles than ions: Four ring electrodes in an arrangement as shown in Fig. 5.66 (left) produce a quadrupole potential (calculated in Fig. 5.66 (right)).

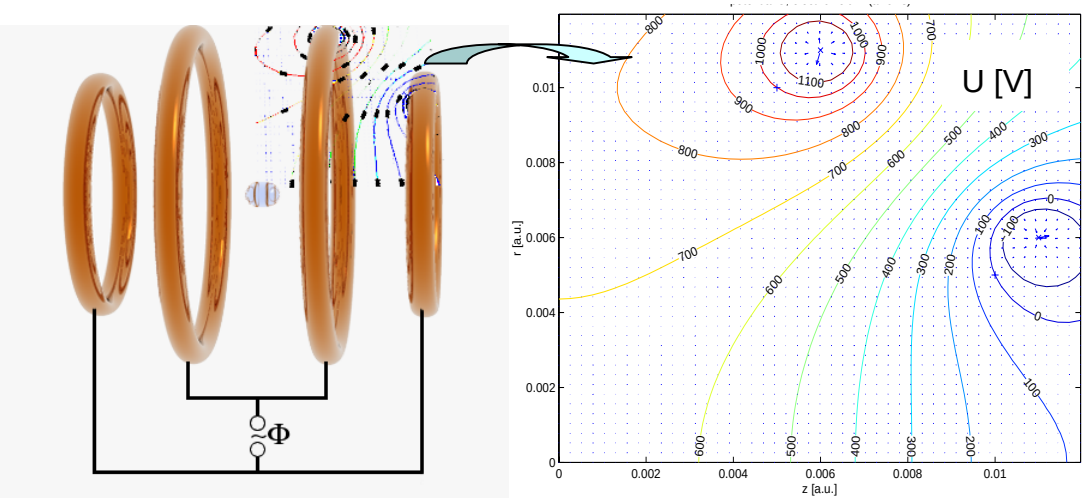

Fig. 5.66 Electrode configuration and calculated potential for a Paul trap using four ring electrodes.

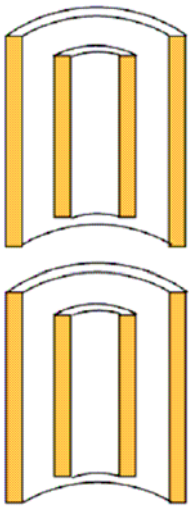

Fig. 5.67 Electrode configuration using four tubes.

This trapping technique allows very small droplet to be trapped over most of its lifetime by readjusting the trap potential during the evaporation process. Droplets in a size range of 200 – 20 µm initial diameter can be trapped and observed with an electrodynamic trap which makes it a very useful tool for single droplet experiments.

A Paul trap was set up in the lab in Heidelberg, following the design of Christian Heinisch [127]. It uses the four-tubes electrode configuration. The outer tube radius is 4 mm, the inner tube radius 1 mm. The distance between inner and outer tubes is 4 mm and 8 mm. The actual setup is shown in Fig. 5.68.

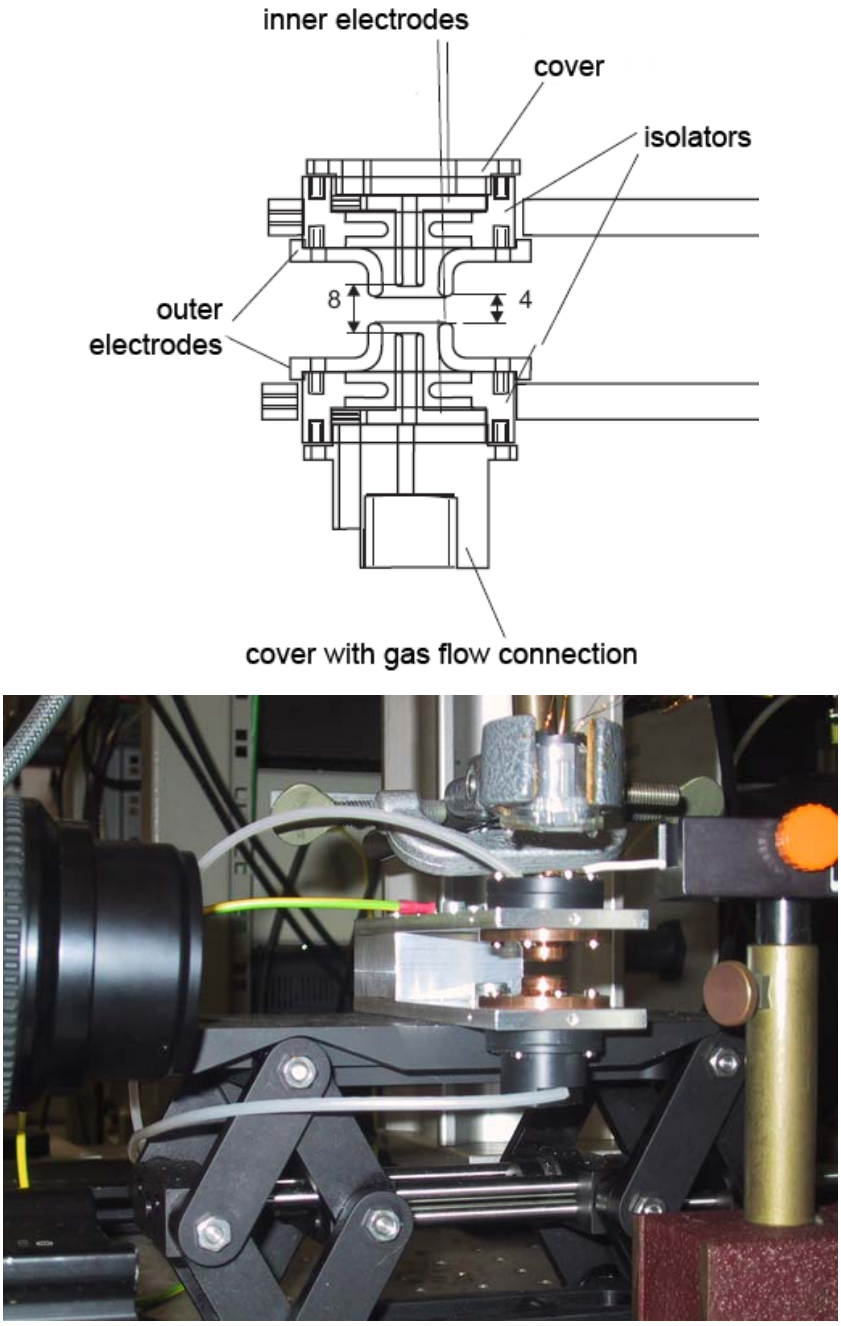

Fig. 5.68 Top: drawing of the the electrodynamic droplet trap [128]. Bottom: Photograph of the actual experimental setup.

The AC voltage for the trap is supplied by a high-voltage transformer unit driven by a function generator providing the frequency. The function generator signal must be amplified (80 W audio amplifier) before being fed into the transformer. To compensate for the gravitational force a DC voltage is superimposed, according to equation (5.44). Typical AC frequencies are in the region of ~50 Hz, the amplitude can be adjusted up to 1.5 kV, typically it is set to 400 V. The droplet is produced by a standard inkjet printer cartridge (HP 51604A) and shot into the trap from above. Directly after the cartridge nozzle the droplet passes a charged copper ring. Thus excess charges are pulled into the

droplet [129] that allow the droplet to be trapped in the oscillating electric field. The droplets have diameters of 60µm (±5%) [56].

The advantage of this configuration compared to the standard Paul trap is the excellent optical accessibility of nearly 360°, making it ideal for laser diagnostics. The specific trap design also includes the possibility of a controlled gas flow around the trapped droplet.

The effective electric field was calculated for the described electrode configuration (see Fig. 5.69) by [127]. The droplet is trapped in the field minima. The present configuration shows three field minima where only the central minimum is relevant. A charged droplet entering the electric field will perform an oscillating motion that drives it into the center.

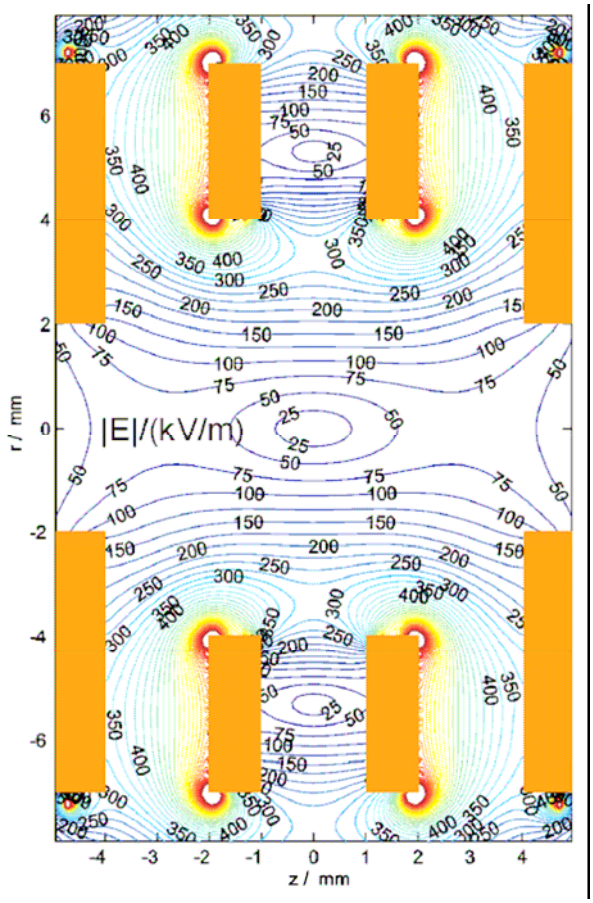

Fig. 5.69 Calculated effective electric field for the Paul trap [127].

According to the equations of motion, the droplet will continue to oscillate around the stable position. Due to the comparably large size of the droplet this oscillation will manifest in oscillating distortions of the droplet shape. However, for droplets of diameters around 50 µm the distortion should not exceed 2 – 3 nm [130].

5.3.1.3 Alternative droplet levitation techniques

In the literature several more methods of levitating single droplets are being discussed. The most important methods shall be briefly mentioned here:

- Acoustic levitation: In an acoustic levitator the droplet is trapped in a standing acoustic wave. This principle of acoustic levitation has been extensively studied in the past [42,131]. A standing acoustic wave at a frequency f of ~50 kHz is generated by a piezoceramic transducer and is reflected by a parallel plate in the distance of $L_r = n \cdot \frac{\lambda}{2}$, with $\lambda = \frac{c_0}{f}$ being the wavelength of the sound wave and c_0 the speed of sound in the surrounding atmosphere. If gravity is neglected, the droplet is trapped in one of the nodes of the standing wave, where the sound pressure has a minimum and the sound pressure gradient a maximum. In the gravitational field, the droplet is trapped at a position slightly lower than the pressure node. A detailed calculation of the acting forces and the influence of the droplet on the pressure field can be found in [131]. Acoustic levitation is limited to rather large droplets (d ~ 1 mm). Due to the sound pressure the droplet is severely distorted from the spherical shape.
- Optical levitation: Droplets of materials with high refractive indices can be trapped in the focus of a laser beam of high intensity. The droplet is levitated and stabilized using radiation pressure forces that act in direction of the laser beam as well as perpendicular to it. For transparent particles the laser operates in the TEM_{00} mode. The forces perpendicular to the beam direction result from Gaussian intensity profile [132]. If the laser beam direction is horizontal, two lasers are needed for stabilization. This configuration is referred to as "optical tweezers" [133]. For highly reflective particles the TEM^*_{01} mode of the laser can be used.
- Diamagnetic levitation: Diamagnetic particles can be levitated a very strong magnetic field. Although stable levitation of magnetic particles in a static magnetic field is forbidden by Earnshaw's theorem [134], diamagnetic particles can be trapped in the minima of an magnetic field. Since most organic materials are at least slightly diamagnetic, it is possible to levitate large objects, even small (living!) animals [135]. The required magnetic field intensities for the levitation of weakly diamagnetic substances, such as water or fuel, are high (up to 10 Tesla).

5.3.2 Droplet heating and evaporation

The heating of the droplets in the experiments presented in this work was done by a CO_2 laser operating at 9.3 or 10.6 µm at an intensity of 600 W/cm^2. Both water and ethanol show strong absorption at these wavelengths. Fig. 5.70 shows the absorption spectrum of water.

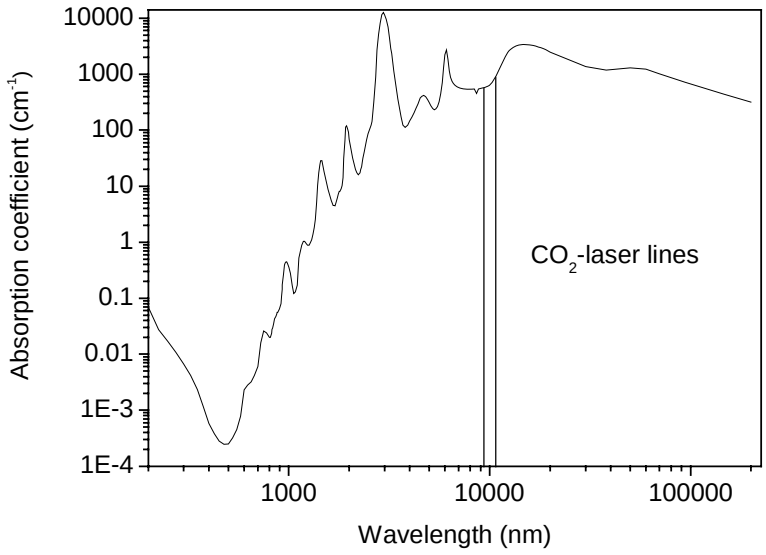

Fig. 5.70 Absorption of liquid water (25°C) in the wavelength range 200-200000 nm. The lines denote the wavelengths emitted by the CO_2 laser.

It has been shown that a droplet heated by a pulsed laser (2 Hz) evaporates according to the d^2-law [70]. The droplet evaporation process was modeled by D. Urzica [136] using an Abramzon-Sirignano approach [20] for convective evaporation of a droplet suspended on a thin glass fiber [56] using the uniform temperature model. The model has been modified to treat the situation of hot droplets being exposed to a cold, convective air stream. The modified expression for the droplet temperature accounts for the laser-induced droplet heating assuming the distillation limit for liquids with a high volatility at atmospheric pressure. The laser-heating is included in the energy equation via the absorbed energy flux W_{abs}.

$$W_{abs} = Q_{abs} \cdot I_0 \cdot \pi r^2 \tag{5.45}$$

where I_0 is the heating laser intensity and r is the droplet radius. Q_{abs} is the efficiency coefficient of the absorption and can be calculated using a Mie-scattering approach [38,40] that is based on the following equations:

$$Q_{abs} = Q_{ext} - Q_{sca} \tag{5.46}$$

with

$$Q_{ext} = \frac{C_{ext}}{\pi r^2} \quad \text{and} \quad Q_{sca} = \frac{C_{sca}}{\pi r^2} \tag{5.47}$$

$$C_{sca} = \frac{2\pi}{k^2}\sum_{n=1}^{\infty}(2n+1)(|a_n|^2 + |b_n|^2) \tag{5.48}$$

$$C_{ext} = \frac{2\pi}{k^2}\sum_{n=1}^{\infty}(2n+1)\,\mathrm{Re}\{a_n + b_n\} \tag{5.49}$$

Here, Q_{ext} and Q_{sca} denote the efficiency factors for total extinction and scattering, respectively, C_{ext} and C_{sca} are the corresponding cross sections respectively, n is the real refractive index, and a_n and b_n denote the scattering coefficients according to the theory of Mie-scattering (see chapter 4.1.1), and Re denotes their real value. For the present conditions, Q_{abs} is computed to be close to unity (Q_{abs} = 0.98). Almost all of the light that enters in a sufficiently large absorbing sphere is absorbed, none of the non-reflected light will be transmitted [38].

The evaporation model reproduces the experimental data quite good, as seen in Fig. 5.71. The deviation of the data at for 5 ms heating pulses probably originates from fluctuations in the laser output power.

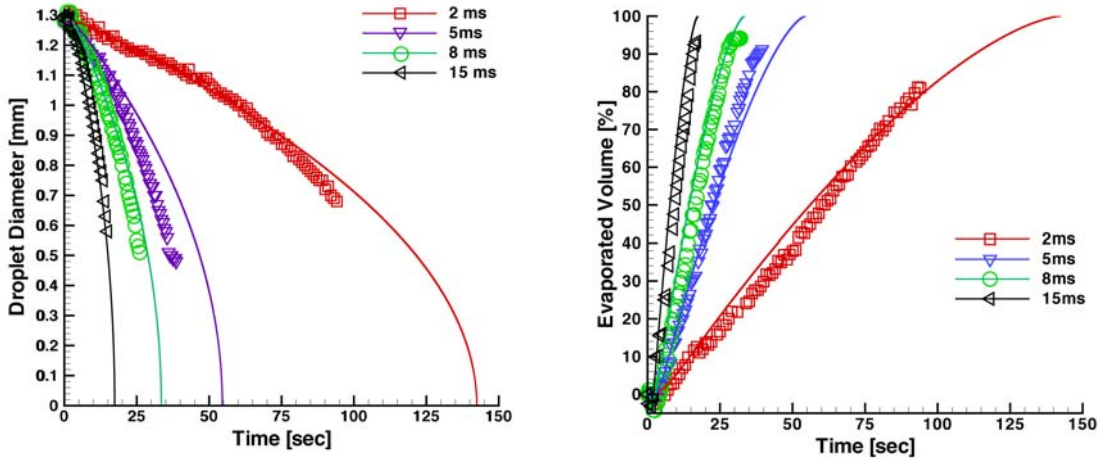

Fig. 5.71 Evaporation of a water droplet for various heating pulse lengths. Left: Droplet diameter evolution, Right: Evaporated droplet volume. Symbols denote experimental data, lines simulated data (from [142]).

The applied model also takes into account the initial increase of the droplet volume caused by thermal expansion that competes with the evaporation for the first few seconds of the process, as was indicated by the experimental data (see Fig. 5.72).

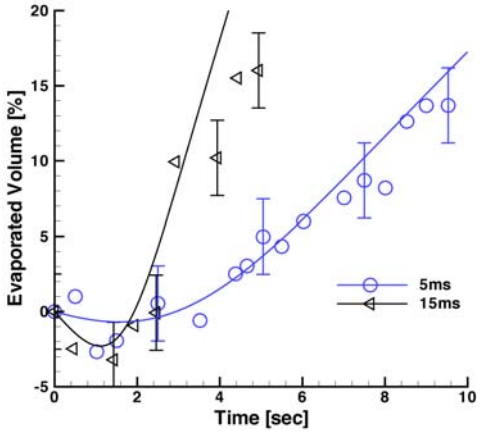

Fig. 5.72 Increase of the droplet volume due to thermal expansion at the beginning of the experiment, indicated by a negative evaporated volume value. Symbols represent experimental data, lines the modeling results (from [142]).

Calculating the droplet temperature as a function of time using the according laser heating pulse durations (as shown in Fig. 5.73) shows that the droplet quickly reaches equilibrium temperature as required for the uniform temperature model.

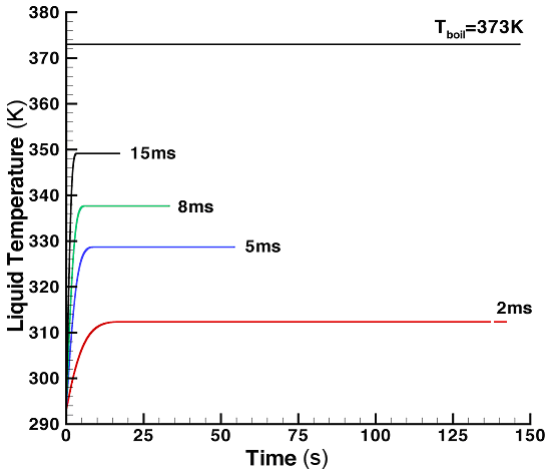

Fig. 5.73 Equilibrium droplet temperature for pulsed CO_2 laser heating with heating pulse duration from 2 to 15 ms (from [142]).

5.3.3 Temperature measurement on a levitated droplet

To confirm the calculations and to gain more insight into the heating and evaporation process temperature measurements on single droplets were performed using the two-color LIF method as applied to the reacting spray in section 5.2.3. The experimental setup is shown in Fig. 5.74.

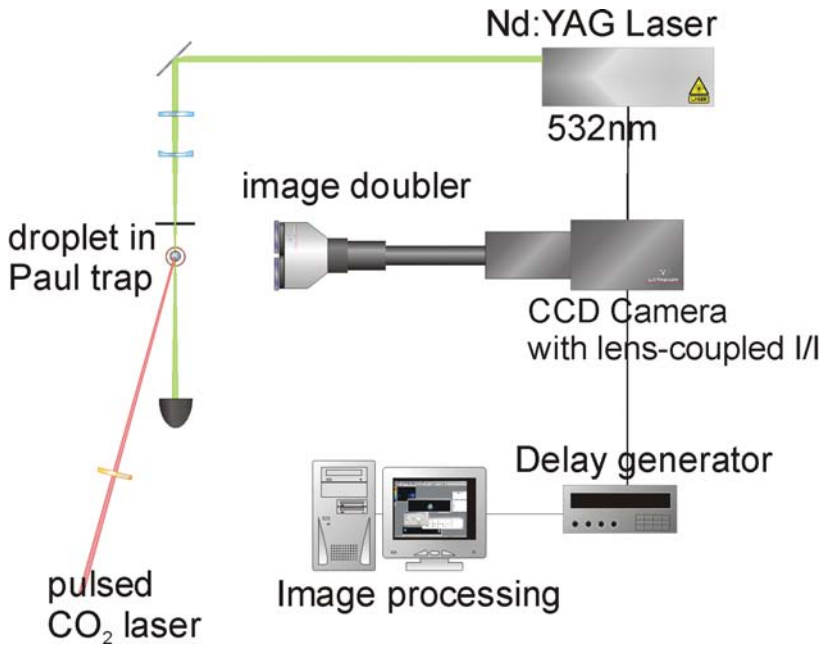

Fig. 5.74 Experimental setup for temperature measurement on a single laser-heated droplet in a Paul trap.

Instead of using two cameras this setup applied a so-called image doubler (*LaVision*) which produces two separate images of the same object on the CCD chip of a camera (*LaVision Flowmaster*). By application of the appropriate spectral filters in the two channels of the image doubler, the two images show the two spectral ranges needed for two-color LIF thermometry. For the described experiment the set of filters presented in section 5.2.3.2 was used (see Fig. 5.56). The image doubler was mounted onto a Nikon $f = 105$ mm, $f_\# = 2$ macro lens. Magnification of the double image was achieved by an extension tube, so that the projection of one pixel into the focal plane corresponds to 5 µm. Fluorescence was induced in a Rhodamine B-doped water droplet ($c = 2.5\times10^{-6}$ mol/l, $d \approx 60$ µm) by a 532 nm Nd:YAG laser (*Continuum*) at a total pulse energy of 3.2 mJ/pulse. It was ensured that this laser energy did not saturate the fluorescence of the droplet at the given concentration, as can be seen in Fig. 5.75.

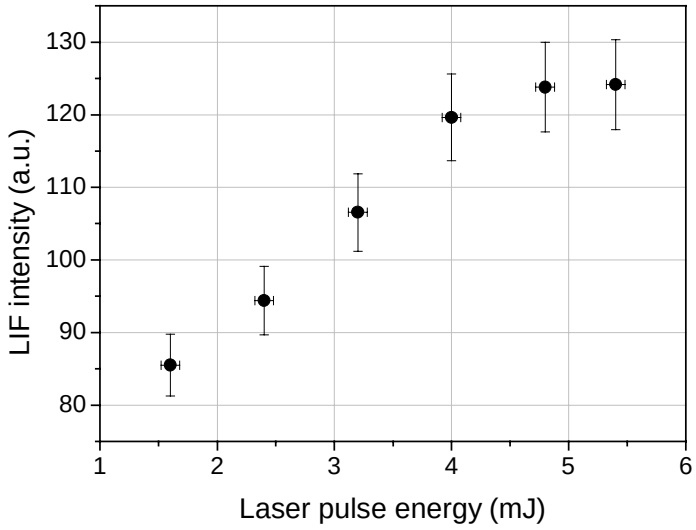

Fig. 5.75 LIF intensity (whole spectral range of Rhodamine B) for different laser pulse energies. Below ~4 mJ/pulse the behavior can be considered to be linear.

Fig. 5.76 shows a typical double LIF image of the droplet. The inhomogeneously distributed LIF intensity is most likely due to the refraction of the incident excitation beam (as discussed in [73]).

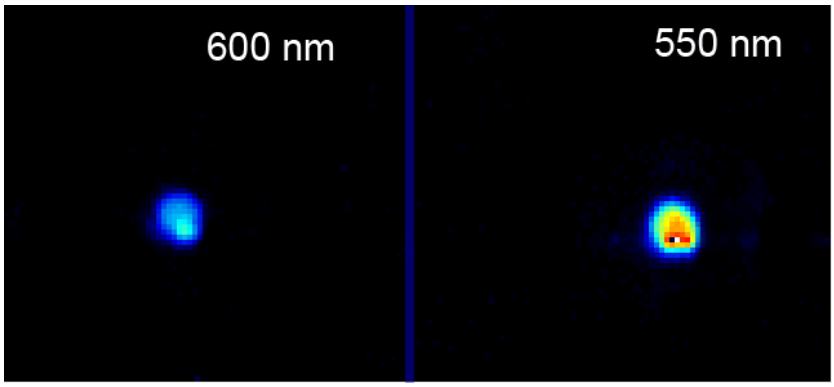

Fig. 5.76 Typical LIF image of a droplet as obtained by the image doubler. The left side shows the signal filtered by a 600±10 nm bandpass, the right side shows the signal filtered by a 550 nm bandpass.

The ratio of the integrated intensity signals from the two spectral regimes is used to calculate the droplet temperature according to equation (4.30). The ratio calculated from the first image, recorded before the heating laser is turned on, is taken as calibration point $R_f(T_0)$: the droplet temperature at this time is assumed to match room temperature T_0 = 294 K. Placed in a slightly warmer atmosphere (heated by a lamp to approximately 303 K), the droplet evaporates slowly, the temperature development is shown in Fig. 5.77. For the first few seconds the droplet cools down by 1–2 K due to heat dissipation caused by the evaporation then heats up to ambient temperature. The noisiness of the

temperature curve shows that these small temperature changes are well at the resolution limit of the method.

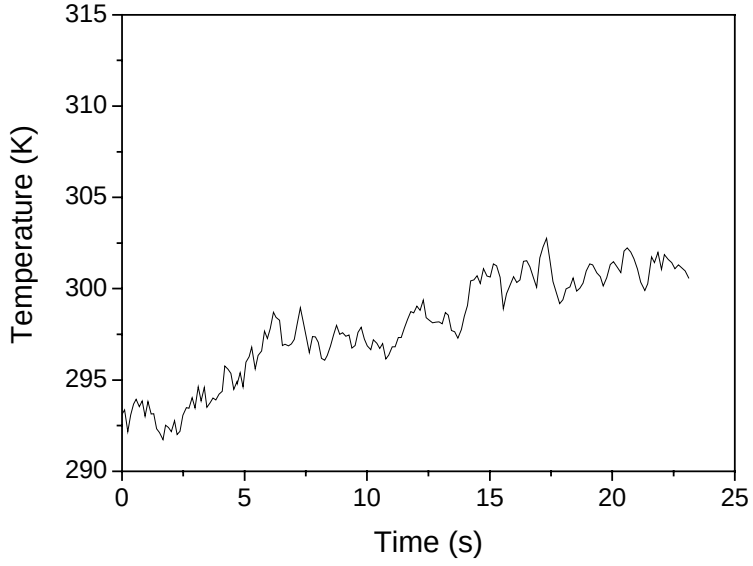

Fig. 5.77 Temperature development of a water droplet ($d \approx 60$ µm) placed in a slightly warmer ($T = 303$ K) atmosphere.

In order to achieve fast and efficient heating the droplet was heated by a CO_2 laser as described in 5.3.2, the heating wavelength set to 9.3 µm, the beam focused to the location of the droplet. The beam diameter in the focal point was still much larger than the droplet diameter (~ 1.5 mm), so a constant heating intensity can be assumed. The intensity assumed in the calculations was 600 J/cm^2. The measured temperatures are systematically higher than the simulated temperatures (see Fig. 5.78). Reasons for that being mainly uncertainties in the boundary conditions for the simulation, such as starting temperature of droplet and surrounding atmosphere. On the experimental side, fluctuations in the heating lasers' energy output as well as uncertainties in the calibration of the sensitivity coefficient $\Delta\beta$ are the main error sources.

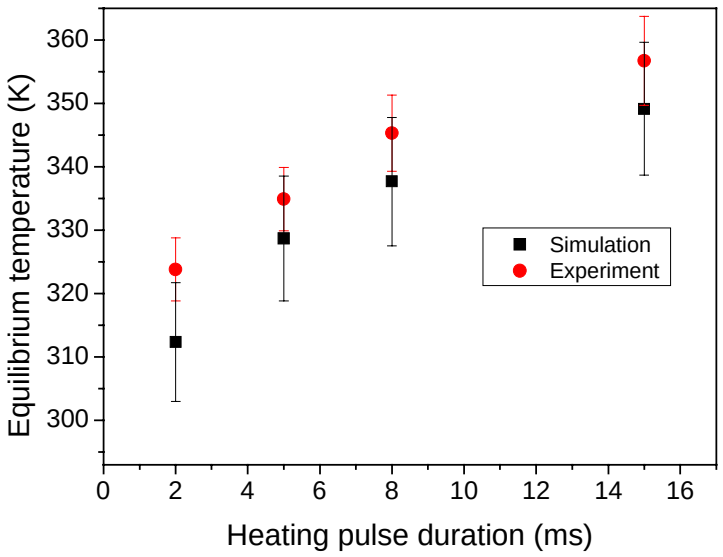

Fig. 5.78 Measured and simulated droplet temperatures for different heating pulse durations. The error in the simulated values is estimated from the uncertainty in the input parameters (laser energy and droplet volume).

5.4 Future

The presented experiments have shown the potential of different tracer-LIF techniques to analyze and gain understanding spray processes in terms of heat and mass transfer. In the future these techniques will be refined and applied to other spray systems.

- The red dye method must still be evaluated under realistic conditions as encountered in a Diesel engine in terms of temperature, pressure and spray density.
- The two-color temperature LIF method also is to be tested under engine conditions. Due to the absorption properties of Diesel fuel, it is restricted to gasoline.
- The LIEF method will be applied to a single trapped droplet to study heat and mass transfer at the droplet surface in high spatial and temporal resolution. In order to do that the present droplet trap has to be modified to be able to maintain a nitrogen atmosphere around the droplet. As the exciplex mixture is basically non-polar, a suitable additive has to be found to bring free charges into the droplet, so that it can be trapped in the electro-dynamic field while minimizing effect on the fluorescence and coevaporation of the exciplex mixture. The present droplet generator (inkjet cartridge) can only produce droplets made of water or aqueous solutions. For more realistic experiments the droplet generation technique has to be changed to be able to be able to handle all types of solvents. Possible choices are a monodisperse droplet-chain generator (see

[129]) or for better controllability a piezo-driven drop-on-demand generator as described in [137]. In addition the present heating method (CO_2 laser radiation) needs to be changed to heating of the ambient atmosphere of the droplet in order to obtain conditions that are closer to realistic processes such as cold droplets injected to a hot atmosphere.

- The imaging system can be improved to achieve higher spatial resolution by using more advanced magnification optics such as a long-distance microscope. For higher temporal resolution a camera system with shorter exposure times and a higher frame rate will be needed.
- An electrodynamic droplet trap utilizing the improvements addressed in the previous two points could then also be used to measure the gas-phase temperature field around an evaporating droplet by NO-LIF thermometry.

6 Summary and conclusions

The experiments presented in this work show the possibilities and limitations of optical spray diagnostic techniques based on laser-imaging. Direct visualization combined with the two-dimensional detection of the Mie-scattering signal was used to analyze the spray structure in an optical direct-injection engine. Even though this provided qualitative and quantitative insight into the cycle-to-cycle and in-cycle fluctuations a fuel spray produced by a multi-hole injector undergoes in the combustion chamber of a direct-injection spark-ignition engine, the results could not be correlated to ignition instabilities encountered in this type of engine. More complex mechanisms in the combustion chamber, involving the interaction of the spray with the gas-flow and the resulting effects on the spatial distribution of the ignitable fuel-air mixture must be considered. Fluorescence-based methods promise to further improve the understanding of these spray processes. They can provide two-dimensional information about droplet sizes, temperatures and vapor and liquid phase concentrations. This work focuses mainly on three methods, all based on laser-induced fluorescence of tracer molecules added to the fuel (tracer LIF).

The laser-induced exciplex fluorescence (LIEF) method allows the simultaneous detection of liquid and vapor phase of the spray by using the spectral separation of the fluorescence from the exciplex that is only present in the liquid phase and the monomer. An exciplex system (n,n-diethylmethylamine, fluorobenzene in n-hexane) that is known for its coevaporative behavior was thoroughly characterized in terms of the temperature dependence of the exciplex and monomer fluorescence. This knowledge allowed the application of this system to quantitatively measure fuel vapor and liquid phase concentrations in a high-pressure high-temperature chamber. Different types of injectors were used and compared. Special care was taken to minimize the so-called “cross-talk” effect. Since this effect is temperature dependent and the liquid temperature was not known in the measurements, uncertainty remains. The temperature dependence of the liquid exciplex fluorescence provides a possibility to actually measure the liquid-phase temperature (simultaneously to the liquid and vapor phase concentrations). A concept in terms of possible detections bands and filter combinations has been elaborated and is presented in this work. The temperature-dependence of the gas-phase fluorescence was analyzed in a heated stream of fluorobenzene in nitrogen. The results showed that for the temperature range where the spray-chamber experiments were conducted, temperature-correction is not necessary, future experiments in hotter environments, however, will have to consider a decrease in the fluorescence intensity from the gas-phase at elevated temperatures. The temperature-dependence of the fluorescence-lifetime of fluorobenzene, was characterized, and was found to present a possibility to measure the gas-phase temperature.

The idea of using the temperature dependence of the fluorescence properties can be extended to other types of tracers. The laser dye Rhodamine B shows a strong sensitivity to temperature in terms of it fluorescence intensity. This temperature sensitivity depends on the detection wavelength, but not on the dye concentration. By taking the ratio of the fluorescence from two wavelength-regions with a strong difference in the sensitivity, the liquid temperature of an evaporating spray can be measured. In this work this method was applied to a reacting ethanol spray in a spray burner.

As we aim to apply tracer-LIF techniques to spray systems that are as close to practical applications as possible, the presented methods were all tested in real fuels – Diesel as well as gasoline. The LIEF method is limited to a single-component fuel (n-hexane) in order to maintain its fluorescence properties and constant relative concentrations during evaporation. However, all the Rhodamine tracers were solved in realistic, multi-component fuels. As Diesel fuel itself shows strong absorption even at visible wavelengths, a tracer (Rhodamine 800) was chosen that can be excited in the 650 – 700 nm range, where the absorption of the fuel sufficiently weak. A new solid-state laser system, specifically developed for this purpose, operating at 671 nm, was applied to measure droplet sizes by means of planar LIF/Mie dropsizing in a Diesel spray doped with a fluorescent tracer.

As all tracers that were applied in this work are hydrophilic, it was necessary to use a detergent in order to dissolve them in the non-polar fuel. Long-chain alcohols such as hexanol were used to dissolve the tracer in Diesel fuel. For gasoline, ethanol was sufficient, even more so as ethanol is a constituent of certain gasoline mixtures. However, the quantum yield of the tracer when solved in real fuel compared to single-component solvents is usually perceptibly lower. In addition, the solvent affects the fluorescence spectrum and its temperature dependence. These effects were studied for Rhodamine 800 in Diesel and Rhodamine B in gasoline.

The following table summarizes the tracer methods applied and advanced in this work, in terms of applicability and error margins.

Method	Tracer/solvent	Masured quantity	Reactive spray (engine)	Non-reactive spray	Single droplet
LIF/Mie dropsizing	Rhodamine 800 / Diesel + 10% ethanol	Sauter-mean diameter	± 20% due to tracer accumulation during evaporation	± 5%, mainly due to reabsorption	
two-color LIF thermometry	Rhodamine B / ethanol	liquid temperature	± 10% (precision) due to calibration errors	± 1.5 K [5]	± 1.5 K
multiline NO-thermometry	NO / air	gas-phase temperature	<4%	<1%	
LIEF	FB/DEMA/n-hexane	liquid fuel concentration	not applicable due to oxygen-quenching	<10 %, due to absorption effects	
LIEF	FB/DEMA/n-hexane (FB fluorescence)	vapor concentrations		<10 % if temperature-dependent cross-talk is considered	

Tab. 6.1: Summary of the methods applied in this work together with specific error margins.

It must be emphasized that the LIEF method allows in principle and with the adequate experimental equipment the simultaneous two-dimensional detection of vapor and liquid fuel concentrations as well as liquid fuel temperatures.

In contrast, the following tables shows other laser-based methods to measure the same spray quantities with high precision. These methods all have the disadvantage of being only zero or one-dimensional and limited to certain fuels or spray–types.

Method	Measured quantity	Error margins	Comment
PDA [2]	droplet size-distribution, droplet velocity distribution, SMD	<2% for dilute sprays	not applicable in dense sprays, point-measurement, droplets must be perfectly spherical
CARS [138,139]	gas-phase temperature	± 60 K (for single shot measurements)	
Raman scattering [140]	liquid phase temperature		line-of-sight, only applicable for single-component fuels
Rainbow refractometry [141]	droplet refractive index → temperature, droplet size	± 6 K (temperature) ~5 % (radius)	not applicable in dense sprays, point-measurement, droplets must be perfectly spherical
Malvern dropsizing (Fraunhofer diffraction) [3]	droplet size		line-of-sight averaged

Tab. 6.2: Alternative optical diagnostic-methods and their error-margins and fields of application.

Another goal of this work was to give experimental benchmarks and exact boundary conditions for new numerical methods to simulate evaporating single droplets or reacting sprays. For this purpose, drop-size distributions, droplet-velocity distributions and temperature fields of the liquid and gas-phase of a Berkeley-type ethanol spray-burner were measured. The drop-size and velocity distributions were used as input for a new spray model implementing a Eulerian-Lagrangian approach, k-ε turbulence and detailed chemistry through a spray flamelet model. Good agreement of experimental and model results were found and areas where the model as well as the experiments need to be improved were identified. Models like this can thus be optimized and be used to gain further understanding of spray processes and enable optimization of spray combustion processes in terms of fuel consumption and pollutant emissions.

To study the evaporation of a single droplet, an electrodynamic levitator (Paul-trap), that traps charged droplets in high-frequency electric field, was designed and setup. The droplet was heated by a pulsed CO_2-laser. For this setup an new droplet evaporation model, that calculates the energy, that is absorbed by the droplet from a Mie-scattering approach, was implemented and showed promising results concerning droplet size and temperature. Future improvements of the setup will allow the detailed study of interface phenomena at the droplet surface, using tracer-LIF techniques.

7 References

1. M. C. Drake, T. D. Fansler, and A. M. Lippert, "Stratified-charge combustion: modeling and imaging of a spray-guided direct-injection spark-ignition engine," Proc. Combust. Inst. **30**, 2683-91 (2005).
2. H.-E. Albrecht, N. Damaschke, M. Borys, and C. Tropea, *Laser Doppler and Phase Doppler Measurement Techniques*. Experimental Fluid Mechanics (Springer, Heidelberg, 2003, 738).
3. J. Swithenbank, J. M. Beer, D. Abbott, and C. G. McCreath, "paper 76-69," in *14th Aerospace Science Meeting* (Washington, DC, 1976).
4. J. Hom and N. Chigier, "Rainbow refractometry: simultaneous measurement of temperature, refractive index, and size of droplets," Appl. Opt. **41**, 1899-1907 (2002).
5. P. Lavieille, F. Lemoine, G. Lavergne, and M. Lebouché, "Evaporating and combusting droplet temperature measurements using two-color laser-induced fluorescence," Exp. Fluids **31**, 45-55 (2001).
6. I. Düwel, P. Peuser, P. Zeller, J. Wolfrum, and C. Schulz, "Laser-based Spray Diagnostics in Commercial Fuels using an new all solid-state laser system," in *19th ILASS Europe 2004* (Nottingham, England, 2004), 266-271.
7. J. B. Ghandhi, P. G. Felton, B. F. Gajdeczko, and F. V. Bracco, "Investigation of the Fuel Distribution in a Two-Stroke Engine with an Air-Assisted Injector," SAE technical paper series No. 940394 (1994).
8. H. R. Ricardo, "Recent Research Work on the Internal Combustion Engine"," SAE Trans. **14**, 30-32 (1922).
9. F.-Q. Zhao, D. L. Harrington, and M.-C. Lai, "Automotive gasoline direct-injection engines," Warrendale PA: Soc. Autom. Engrs. (2002).
10. A. S. Solomon, R. W. Anderson, P. M. Najt, and F.-Q. Zhao, "Direct Fuel Injection for Gasoline Engines PT-80," SAE Technical Paper Series (2000).
11. A. M. Lippert, T. D. Fansler, M. C. Drake, and A. S. Solomon, "High-speed imaging and CFD modeling of sprays and combustion in a spray- guided spark-ignition direct injection engine," in *6. AVL Internationales Symposium für Verbrennungsdiagnostik* (Baden-Baden, 2004).
12. T. D. Fansler, M. C. Drake, I. Düwel, and F. P. Zimmermann, "Fuel-Spray and Spark-Plug Interactions in a Spray-Guided Direct-Injection Gasoline Engine," in *7. Internationales Symposium für Verbrennungsdiagnostik* (Baden-Baden, 2006).
13. Kraftfahrt-Bundesamt, *Statistische Mitteilungen - Reihe 2: Fahrzeugbestand*. 2005. p. 294.
14. M. Blessing, *Untersuchung und Charakterisierung von Zerstäubung, Strahlausbreitung und Gemischbildung aktueller Dieseldirekteinspritzsysteme*, in *Institut für Verbrennungsmotoren und Kraftfahrwesen*. 2004, Universität Stuttgart: Stuttgart.

15. R. H. Stanglmaier and C. E. Roberts, "Homogeneous charge compression ignition (HCCI): Benefits, compromises, and future engine applications," SAE Trans. **108**, 2138-2145 (1999).

16. D. L. Reuss and V. Sick, "Inhomogeneities in HCCI combustion: An imaging study," SAE Trans. **114**, 867-882 (2005).

17. H. Kopecek, H. Maier, G. Reider, F. Winter, and E. Wintner, "Laser ignition of methane-air mixtures at high pressures," Experimental Thermal and Fluid Science **27**, 499-503 (2003).

18. J. Liu, P. D. Ronney, F. Wang, L. C. Lee, and M. Gundersen, "Transient Plasma Ignition For Lean Burn Applications," in *41st Aerospace Sciences Meeting* (Reno, Nevada, 2003), 2003-6208.

19. A. Frohn and N. Roth, *Dynamics of Droplets*, 1 ed (Springer Verlag, Stuttgart, 2000, 292).

20. W. A. Sirignano, *Fluid Dynamics and Transport of Droplets and Sprays*, 1 ed (Cambridge University Press, Irvine, California, 1999, 311).

21. G. M. Faeth, "Current status of droplet and liquid combustion," Prog. Energy Combust. Sci. **3**, 191-224 (1977).

22. J. Wilms, *Evaporation of Multicomponent Droplets*, in *Fakultät für Luft- und Raumfahrttechnik und Geodäsie*. 2005, Universität Stuttgart.

23. G. M. Faeth, "Evaporation and Combustion of Sprays," Prog. Energy Combust. Sci. **9**, 1-76 (1983).

24. A. H. Lefebvre, *Atomization and Sprays*, 1 ed (Taylor & Francis Publishers, 1989).

25. C. A. Chryssakis, D. N. Assanis, J.-K. Lee, and K. Nishida, "Fuel Spray Simluation of High-Pressure Swirl-Injector for DISI Engines and Comparison with Laser Diagnostic Measurements," SAE technical paper series no. 2003-01-0007 (2003).

26. M. Gavaises and C. Arcoumanis, "Modelling of sprays from high-pressure swirl atomizers," Int. J. Engine Research **2**, 95-117 (2001).

27. Y. Iwamoto, K. Noma, O. Nakayama, T. Yamauchi, and H. Ando, "Development of Gasoline Direct Injection Engine," SAE technical paper series no. 970541 (1997).

28. F.-Q. Zhao, M.-C. Lai, and D. L. Harrington, "Automotive spark-ignited direct-injection gasoline engines," Progress in Energy and Combustion Science **25**, 437-562 (1999).

29. N. Mitroglou, J. M. Nouri, M. Gavaises, and C. Arcoumanis, "Spray characteristics of a multi-hole injector for direct-injection gasoline engines," Int. J. Engine Research **7**, 255-270 (2006).

30. A. M. Lippert, S. H. El Tahry, M. S. Huebler, S. E. Parrish, H. Inoue, T. Noyori, K. Nakama, and T. Abe, "Development and optimisation of a small-displacement spark-ignition direct-injection - Stratified operation," SAE technical paper series no. 2004-01-0539 (2004).

31. J. M. Nouri, M. A. Hamid, Y. Yan, and C. Arcoumanis, "Spray characterization of a piezo pintle-type injector for gasoline direct injection-engines," in *Second*

International Conference on Optical and Laser Diagnostics (London, UK, 2005), 238-250.

32. Y. Yan, G. S., J. M. Nouri, R. D. Lockett, and C. Arcoumanis, "Investigation of spray characteristics in a spray guided DISI engine using PLIF and LDV," in *Second International Conference on Optical and Laser Diagnostics* (London, UK, 2005), 70-82.
33. S. Horender and M. Sommerfeld, "Droplet-Droplet and Droplet-Vapor Interaction in an evaporating monodispersed spray," in *20th ILASS Europe* (Orléans, France, 2005), 283-287.
34. F. Halter, C. Chauveau, C. Mounaim-Rousselle, and I. Gökalp, "Experimental studies on the vaporization of a three-dimensional droplet network," in *20th ILASS Europe* (Orléans, France, 2005), 295-300.
35. P. Eckert, C. Baumgarten, and G. P. Merker, "Potentials and Limitations of Diesel Engines Combustion Simulation," in *7th International Symposium on Internal Combustion Diagnostics* (Baden-Baden, 2006), 287-302.
36. H.-W. Ge, *Probability Density Function Modeling of Turbulent Non–reactive and Reactive Spray Flows*. 2006, Universität Heidelberg. p. 148.
37. H. Ge and E. Gutheil, "Probability Density Function (PDF) Simulation of Turbulent Spray Flows," Atomization and Sprays, 531-542 (2006).
38. C. Bohren and D. Huffman, *Absorption and Scattering of Light by Small Particles* (Wiley, New York, 1998).
39. P. W. Atkins, *Physikalische Chemie*, 1 ed (VCH-Verlag, Oxford, UK, 1990, 889).
40. H. C. van de Hulst, *Light Scattering by Small Particles* (Dover Publications, Inc., New York, 1981).
41. P. Laven, *Mieplot*. 2004.
42. A. L. Yarin, G. Brenn, O. Kastner, and C. Tropea, "Evaporation of acoustically levitated droplets," J. Fuid Mech. **399** (1999).
43. L. Rayleigh, "On the scattering of light by small particles," Philosophical Magazine **41**, 447-451 (1871).
44. G. Otter and R. Honecker, *Atomphysik.* Atome-Moleküle-Kerne. Vol. 1 (Teubner, Stuttgart, 1993).
45. H. Kuhn, "Free Electron Model for Absorption Spectra of Organic Dyes," The Journal of Chemical Physics **17**, 840-841 (1948).
46. U. Brackmann, *Lambdachrome® Laser Dyes*, 3rd ed (Lambda Physik, Goettingen, 2000, 284).
47. K. H. Drexhage, "Structure and Properties of Laser Dyes," in *Dye Lasers*, F.P. Schäfer, Editor (Springer, Heidelberg, 1973).
48. T. Förster, "Zwischenmolekulare Energieumwandlung und Fluoreszenz," Annalen der Physik **2**, 55-75 (1948).
49. I. L. Arbeloa and P. R. Ojeda, "Dimeric states of Rhodamine B," Chem. Phys. Lett. **87**, 556-560 (1982).

50. I. Düwel, T. Kunzelmann, J. Schorr, C. Schulz, and J. Wolfrum, "Application of fuel tracers with different volatilities for planar LIF/Mie drop sizing in evaporating systems," in *Proc. of the 9th ICLASS 2003* (Sorrento, Italy, 2003).

51. W. D. Bachalo and M. J. Houser, "Phase Doppler spray analyzer for simultaneous measuremwents of dropsize and velocity distributions," Opt. Eng. **23**, 583-590 (1984).

52. W. D. Bachalo, "The Phase Doppler Method: Analysis, Performance Evaluations and Applications," Part. Part. Syst. Charact. **11**, 73-83 (1994).

53. F. Lemoine, Y. Antoine, M. Wolff, and M. Lebouché, "Simultaneous temperature and 2D velocity measurements in a turbulent heated jet using combined laser-induced fluorescence and LDA," Exp. Fluids **26**, 315-323 (1999).

54. R. Domann and Y. Hardalupas, "A Study of Parameters that Influence the Accuracy of the Planar Droplet Sizing (PDS) Technique," Particle & Particle Systems Characterization **18**, 3-11 (2001).

55. M. Fischer and J. Georges, "Use of thermal lens spectrometry for the investigation of dimerization equilibria of rhodamine 6G in water and aqueous micellar solution," Spectrochimica Acta Part A **53**, 1419-1430 (1997).

56. I. Düwel, *Beobachtung der laserinduzierten Einzeltropfenverdampfung mit Hilfe der laserinduzierten Fluoreszenz*, in *Fakultät für Physik und Astronomie*. 2003, Ruprecht-Karls Universität: Heidelberg. p. 99.

57. I. Düwel, J. Schorr, J. Wolfrum, and C. Schulz, "Laser-induced fluorescence of tracers dissoved in evaporating droplets," Appl. Phys. B **78**, 127-131 (2004).

58. W. Koban, J. Schorr, and C. Schulz, "Oxygen-distribution imaging with a novel two-tracer laser-induced fluorescence technique," Appl. Phys. B **74** (2002).

59. C.-F. Lee and F. V. Bracco, "Exciplex Technique applied to two-phase flows," in *The 36th Conference on Aeronautics and Astronautics* (Hsin-Chu, Taiwan, 1994), 459-465.

60. W. Koban, J. D. Koch, R. K. Hanson, and C. Schulz, "Oxygen quenching of toluene fluorescence at elevated temperatures," Appl. Phys. B **80**, 777-784 (2005).

61. P. Wieske, S. Wissel, G. Grünefeld, and S. Pischinger, "Improvement of LIEF by wavelength-resolved acquisition of multiple images using a single CCD detector - Simultaneous 2D measurement of air/fuel ratio, temperature distribution of the liquid phase and qualitative distribution of the liquid phase with the Multi-2D technique," Appl. Phys. B **83**, 323-329 (2006).

62. B. Hiller and R. K. Hanson, "Properties of the iodone molecule relevant to laser-induced fluorescence experiments in gas flows," Exp. Fluids **10**, 1-11 (1990).

63. J. C. André and J. Molinari, "Mise au point les différents facteurs physicochimiques influant sur la mesure de concentration de traceures fluorescencts et leurs conséquences pratiques en hydrologie," J. Hydrol. **30**, 257-285 (1976).

64. F. Lemoine and B. Leporcq, "An efficient optical pressure measurement in compressible flows: laser-induced fluorescence," Exp. Fluids **19**, 150-158 (1995).

65. A. O. Vyrodow, J. Heinze, M. Dillmann, U. E. Meier, and W. Stricker, "Laser-induced fluorescence thermometry and concentration measurements on NO A-X (0,0) transitions in the exhaust gas of high pressure CH_4/air flames," Appl. Phys. B. **61**, 409-414 (1995).

66. W. G. Bessler and C. Schulz, "Quantitative multi-line NO-LIF temperature imaging," Appl. Phys. B **78**, 519-533 (2004).

67. H. Kronemayer, W. G. Bessler, and C. Schulz, "Gas-phase temperature imaging in spray systems using multi-line NO-LIF thermometry," Appl. Phys. B Rap. Com. **81**, 1071-1074 (2005).

68. W. G. Bessler, C. Schulz, T. Lee, J. B. Jeffries, and R. K. Hanson, "Carbon dioxide UV laser-induced fluorescence in high-pressure flames," Chem. Phys. Lett. **375**, 344-349 (2003).

69. W. G. Bessler, C. Schulz, V. Sick, and J. W. Daily, "A versatile modeling tool for nitric oxide LIF spectra (http://www.pci.uni-heidelberg.de/pci/lifsim)," in *3rd Joint meeting of the US sections of The Combustion Institute* (Chicago, 2003), PI1-6.

70. I. Düwel, J. Schorr, J. Wolfrum, and C. Schulz, "Laser-induced fluorescence of tracers dissolved in evaporating droplets," Appl. Phys. B **78**, 127-131 (2004).

71. C.-N. Yeh, H. Kosaka, and T. Kamimoto, "A fluorescence / scattering imaging technique for instantaneous 2-D measurement of particle size distribution in a transient spray," Proc. 3rd Congr. on Opt. Part. Sizing, Yokohama-Japan, (1993).

72. M. C. Jermy and D. Greenhalgh, "Planar dropsizing by elastic and fluorescence scattering in sprays too dense for phase Doppler measurement," Appl. Phys. B **71**, 703-710 (2000).

73. R. Domann and Y. Hardalupas, "Spatial distribution of fluorescence intensity within large droplets and its dependence on dye concentration," Applied Optics **40**, 3586-3597 (2001).

74. F. K. Kneubühl and M. W. Sigrist, *Laser*, 5 ed (Teubner, 1999).

75. D. Meschede, *Optik, Licht und Laser* (B.G. Teubner, Stuttgart - Leipzig, 1999).

76. I. Düwel, J. Schorr, P. Peuser, P. Zeller, J. Wolfrum, and C. Schulz, "Spray diagnostics using an all solid-state Nd:$YAlO_3$ laser and fluorescence tracers in commercial gasoline and Diesel fuels," Appl. Phys. B **79**, 249 - 254 (2004).

77. N. H. Leibinger-Kammüller, *Werkzeug Laser* (Vogel, Würzburg, 2006, 300).

78. C. Barnes, *Copper at the Cutting Edge: the Copper Vapor Laser*. 2001.

79. R. P. Mildren and J. A. Piper, "Compact and efficient kinetically enhanced copper vapor lasers of high average power (100W)," Opt. Lett. **28**, 1936-1938 (2003).

80. S. Böckle, *Hochempfindlicher Nachweis von Majoritäten- und Minoritätenspezies durch Raman- und Fluoreszenzspektroskopie in einer turbulenten Vormischflamme und im Abgasstrahl eines kommerziellen Düsentriebwerks*, in *Fakultät für Physik und Astronomie*. 1998, Ruprecht-Karls-Universität: Heidelberg.

81. LaVision, *ICCD Fundamentals*. 2003.

82. LaVision, *Pro-Package Manual for DaVis 6.* 2002: Göttingen.

83. W. Hübner, A. Witt, B. Hoss, T. Albrecht, B. Durst, and A. Abdelfattah, "Methodensatz bei der Entwicklung eines weiterführenden DI Brennverfahrens," in *24. Internationales Wiener Motorensymposium* (15-16 May, 2003).

84. T. D. Fansler, B. Stojkovic, M. C. Drake, and M. E. Rosalik, "Local fuel concentration measurements in internal combustion engines using spark-emission spectroscopy," Appl. Phys. B **75**, 577-590 (2002).

85. T. D. Fansler and M. C. Drake, "Designer diagnostics for developing direct-injection gasoline engines," in *Second International Conference on Optical and Laser Diagnostics (ICOLAD 2005)* (City University, London, UK, 2005).

86. D. Zimmermann and e. al., "Inflammation of Stratified Mixtures in Spray Guided DI Gasoline Engines: Optimization by Application of High Speed Imaging Techniques," in *6. AVL Internationales Symposium für Verbrennungsdiagnostik* (Baden-Baden, 2004).

87. C. Parigger, D. H. Plemmons, R. J. Litchford, and S. M. Jeng, "Exciplex Liquid-Phase Thermometer Using Time-Resolved Laser-Induced Fluorescence," Opt. Lett. **23**, 76-78 (1998).

88. S. Escobar, J. E. González, and L. A. Rivera, "Laser-induced fluorescence temperature sensor for in-flight droplets," Experimental Heat Transfer **14**, 119-134 (2001).

89. L. A. Melton, "Spectrally separated fluorescence emissions for diesel fuel droplets and vapor," Appl. Opt. **22**, 2224 - (1983).

90. C.-N. Yeh, T. Kamimoto, S. Kobori, and H. Kosaka, "2D imaging of fuel vapor concentration in a Diesel spray via exciplex-based fluorescence technique," SAE technical paper series No. 932652 (1993).

91. J. U. Kim, B. Golding, H. J. Schock, P. Keller, and D. G. Nocera, "Exciplex Fluorescence Visualization System for Pre-Combustion Diagnosis of an Automotive Gasoline Engine," Advances in Engine Combustion and Flow Diagnostics, 295-300 (1996).

92. K.-U. Münch, H. Krämer, and A. Leipertz, "Investigation of Fuel Evaporation Inside the Intake of a SI Engine Using Laser-Induced Exciplex Fluorescence with a New Seed," SAE technical paper series no. 961930, 101-107 (1996).

93. R. Shimizu, S. Matumoto, S. Furuno, M. Murayama, and S. Kojima, "Measurement of air-fuel mixture distribution in a gasoline engine using LIEF technique," SAE technical paper series no. 922356 (1992).

94. L. A. Melton, "Exciplex-Based Vapor/Liquid Visualization Systems Appropriate for Automotive Gasolines," Applied Spectroscopy **47**, 782-786 (1993).

95. A. P. Fröba, F. Rabenstein, K.-U. Münch, and A. Leipertz, "Mixture of Triethylamine (TEA) and Benzene as a New Seeding Material for the Quantitative Two-Dimensional Laser-Induced Exciplex Fluorescence Imaging of Vapor and Liquid Fuel Inside SI Engines," Combust. Flame **112**, 199-209 (1998).

96. J. P. Styron, P. L. Kelly-Zion, C. F. Lee, J. E. Peters, and R. A. White, "Multicomponent Liquid and Vapor Fuel Distribution Measurements in the

Cylinder of a Port-Injected, Spark-Ignition Engine," SAE technical paper series no. 2000-01-0243 (2000).

97. M. Skogsberg, P. Dahlander, R. Lindgren, and I. Denbratt, "Effects of Injector Parameters on Mixture Formation for Multi-Hole Nozzles in a Spray-Guided Gasoline DI Engine," SAE technical paper series no. 2005-1-0097 (2005).
98. N. Graf, *Einsatz der Laserinduzierten Fluoreszenz organischer Moleküle zur Visualisierung von Gemischbildungs- und Verbrennungsprozessen*, in *Naturwissenschaftlich-Mathematische Gesamtfakultät*. 2003, Ruprecht-Karls-Universität: Heidelberg.
99. J. Schorr, *Entwicklung und Anwendung von Fluoreszenztracer-Verfahren für die lasergestützte, abbildende Spraydiagnosik*, in *Naturwissenschaftlich-Mathematische Gesamtfakultät*. 2003, Ruprecht-Karls-Universität: Heidelberg.
100. S. Frigo, *Evaluation of fluorescing tracers for hexane and isooctane*. 1993, Department of Mechanical and Aerospace Engineering, Princeton University. p. 34.
101. W. Becker, *Advanced Time-Correlated Single Photon Counting Techniques*. Springer Series in Chemical Physics. Vol. 81 (Springer, 2005).
102. D. P. Herten, A. Biebricher, M. Heilemann, T. Heinlein, C. Müller, S. P., P. Tinnefeld, K. D. Westen, M. Sauer, and J. Wolfrum, "Optical single molecule techniques for analytical and biological applications," Recent Res. Devel. Applied Phys. **7**, 345-368 (2004).
103. W. Koban, *Photophysical characterization of toluene and 3-pentanone for quantitative imaging of fuel/air ratio and temperature in combustion systems*, in *Combined Faculties for the Natural Sciences and for Mathematics*. 2005, Ruperto-Carola University: Heidelberg. p. 115.
104. F. P. Zimmermann, *New approaches for optical and microoptical diagnostics in IC engines*, in *Naturwissenschaftlich-Mathematische Gesamtfakultät*. 2006, Ruprecht-Karls Universität: Heidelberg. p. 151.
105. M. Jacon, C. Lardeux, R. Lopezdelgado, and A. Tramer, "3rd Deacy Channel and Vibrational Redestribution Problems in Benzene-Derivatives," Chemical Physics **24**, 145-157 (1977).
106. L. A. Dombrovsky, S. S. Sazhin, S. V. Mikhalovsky, R. Wood, and M. R. Heikal, "Spectral properties of diesel fuel droplets," Fuel **82**, 15 - 22 (2003).
107. L. Zimmer, Y. Ikeda, R. Domann, and Y. Hardalupas, "Simultaneous LIF and Mie scattering measurements for branch-like spray cluster in industrial oil burner," in *40th AIAA Aerospace Sciences meeting and Exhibit* (Reno, 2002), 10.
108. O. O. Abugo, R. Nair, and J. R. Lakowicz, "Fluorescence Properties of Rhodamine 800 in Whole Blood and Plasma," Analytical Biochemistry **279**, 142-150 (2000).
109. V. Buschmann, K. D. Weston, and M. Sauer, "Spectroscopic Study and Evaluation of Red-Absorbing Fluorescent Dyes," Bioconjugate Chem. **14**, 195-204 (2003).

110. I. López Arbeloa and K. K. Rohtagni-Mukherjee, "Solvent Effects on the Photophysics of the molecular forms of Rhodamine B. Internal Conversion Mechanism," Chemical Physics Letters **129**, 607-614 (1986).

111. V. G. McDonell and G. S. Samuelsen, "An Experimental Data Base for Computational Fluid Dynamics of Reacting and Nonreacting Methanol Sprays," J. Fluids Engineer. **117**, 145-153 (1995).

112. M. Sommerfeld and H. H. Qiu, "Experimental Studies of Spray Evaporation in Turbulent Flow," Int. J. Heat Fluid Flow **19**, 10-22 (1998).

113. R. Cabra, T. Myhrvold, J.-Y. Chen, R. W. Dibble, A. N. Karpetis, and R. S. Barlow, "Simultaneous laser-Raman-Rayleigh-LIF measurements and numerical modeling results of a lifted turbulent H_2/N_2 jet flame in a vitiated flow," Proc. Combust. Inst. **29**, 1881-1888 (2002).

114. C. Hollmann and E. Gutheil, "Modeling of Turbulent Spray Diffusion Flames Including Detailed Chemistry," Proc. Combust. Inst **26**, 1731-1738 (1996).

115. F. X. Demoulin and R. Borghi, "Modeling of Turbulent Spray Combustion with Application to Diesel Like Experiment," Combust. Flame **129**, 281-293 (2002).

116. T. Kunzelmann, *Charakterisierung von Sprayflammen mittels abbildender Laserspektroskopie*, in *Mathematisch-Naturwissenschftliche Gesamtfakultät*. 2002, Ruprecht-Karls Universität: Heidelberg. p. 103.

117. H. Kronemayer, *Spektroskopische Messung der Gastemperatur mittels NO-LIF in Spraysystemen*, in *Fakultät für Chemie und Geowissenschaften*. 2004, Ruprecht-Karls-Universität: Heidelberg.

118. I. Düwel, H.-W. Ge, H. Kronemayer, R. W. Dibble, E. Gutheil, C. Schulz, and J. Wolfrum, "Experimental and numerical characterization of a turbulent spray flame," Proc. Comb. Inst. **31**, 2247-2255 (2007).

119. H. Kronemayer, I. Düwel, and C. Schulz, "Temperature imaging in spray flames," in *European Combustion Meeting* (Louvain-la-Neuve, Belgium, 2005).

120. H.-W. Ge, I. Düwel, H. Kronemayer, R. W. Dibble, E. Gutheil, C. Schulz, and J. Wolfrum, "Laser based experimental and Monte Carlo PDF numerical investigation of an ethanol/air spray flame," Chem. Eng. Science **submitted** (2007).

121. B. Abramzon and W. A. Sirignano, Int. J. Heat Mass Transfer **9**, 1605-1618 (1989).

122. K. Launder, *From Promise to Purpose: Opportunities and Constraints for Ethanol-based Transportation Fuels*. 2001, Michigan State University, Department of Resource Development. p. 53.

123. A. L. Yarin, G. Brenn, and D. Rensink, "Evaporation of acoustically levitated droplets of binary liquid mixtures," International Journal of Heat and Fluid Flow **23**, 471-486 (2002).

124. S. X. Q. Lin and X. D. Chen, "Improving the glass-filament method for accurate measurement of drying kinetics of liquid droplets," Chemical Engineering research & design **80**, 401-410 (2002).

125. W. Paul, "Electromagnetic traps for charged and neutral particles," Reviews of Modern Physics **62**, 531-540 (1990).

126. M. Tona, *Study on Spherical Microlasers Levitated in an Ion Trap*. 2002, Kochi University of Technology. p. 132.

127. C. Heinisch, S. Bakic, N. Damaschke, J. Petter, T. Tschudi, and C. Tropea, "Neue Paulfallengeometrie zur Fixierung von Tropfen und Partikeln in Gasströmungen mit 360°-Zugang für Laserdiagnostik," in *Fachtagung "Lasermethoden in der Strömungsmesstechnik"* (Braunschweig, 2006).

128. C. Heinisch, *Personal Communication*. 2006.

129. T. Leclaire, *Entwicklung eines Verfahrens zur Erzeugung monodisperser Partikel mit definierter elektrischer Ladung*, in *Fachbereich Ingenieurwissenschaften, Abteilung Maschinenbau*. 2005, Universität Duisburg-Essen: Duisburg.

130. B. Krämer, H. Hübner, H. Vortisch, L. Wöste, T. Leisner, M. Schwell, E. Rühl, and H. Baumgärtel, "Homogeneous nucleation rates of supercooled water measured in single levitated microdroplets," Journal of Chemical Physics **111**, 6521-6527 (1999).

131. O. Kastner, *Theoretische und experimentelle Untersuchungen zum Stoffübergang von Einzeltropfen in einem akustischen Rohrlevitator*, in *Technische Fakultät*. 2001, Universität Erlangen-Nürnberg: Erlangen. p. 173.

132. A. Ashkin, "Acceleration and trapping of particles by radiation pressure," Phys. Rev. Lett. **24**, 156-159 (1970).

133. D. G. Grier, "A revolution in optical manipulation," Nature **424**, 810-816 (2003).

134. M. D. Simon, L. O. Heflinger, and A. K. Geim, "Diamagnetically stabilized magnet levitation," Am. J. Phys. **69**, 702-713 (2000).

135. M. D. Simon and A. K. Geim, "Diamagnetic levitation: Flying frogs and floating magnets (invited)," Journal of Applied Physics **87**, 6200-6204 (2000).

136. D. Urzica, I. Düwel, C. Schulz, and E. Gutheil, "Laser-Induced Evaporation of a Single Droplet - An Experimental and Computational Investigation," in *Proc. of the 19th ILASS Europe 2005* (Orléans, 2005), 241-246.

137. H. Ulmke, T. Wriedt, and K. Bauckhage, "Piezoelectric Droplet Generator for the Calibration of Particle-Sizing Instruments," Chem. Eng. Technol. **24**, 265-268 (2001).

138. A. C. Eckbreth, "CARS thermometry in practical combustors," Combust. Flame **39**, 133-147 (1980).

139. F. Beyrau, A. Bruer, T. Seeger, and A. Leipertz, "Gas-phase temperature measurement in the vaporizing spray of a gasoline direct-injection injector by use of pure rotational coherent anti-Stokes Raman scattering," Optics Letters **29**, 247-249 (2004).

140. G. Grünefeld, V. Beushausen, P. Andresen, and W. Hentschel, "Spatially resolved Raman scattering for multi-species and temperature analysis in technically applied combustion systems: Spray flame and four-cylinder in-line engine," Appl. Phys. B. **58**, 333-342 (1994).

141. P. Massoli, "Rainbow refractometry applied to radially inhomogeneous spheres: the critical case of evaporating droplets," Appl. Opt. **37**, 3227-3235 (1998).

142. D. Urzica, *PhD Thesis, Universität Heidelberg, to be submitted*. 2007.

Acknowledgements

An dieser Stelle möchte ich allen danken, die auf ihre Weise zum Gelingen dieser Arbeit beigetragen haben.

An erster Stelle gebührt mein Dank Herrn Prof. Dr. Christof Schulz für die Vergabe des interessanten Themas, die hervorragende Betreuung, seine vielen konstruktiven Vorschläge und Hinweise und nicht zuletzt für seine Geduld.

Ich danke außerdem Herrn Prof. Dr. Jürgen Wolfrum für die Aufnahme in seinen Arbeitskreis und die Bereitstellung der nötigen Infrastruktur und die Übernahme des Zweitgutachtens.

Mein besonderer Dank geht an die ehemalige Arbeitsgruppe 2D-LIF (jetzt IVG Duisburg), vor allem Daniel Barzan, Axel Hoffmann, Max Hofmann, Wieland Koban, Helmut Kronemayer, Burkhard Lewerich, My Yen Luong und Frank Zimmermann für das gute Arbeitsklima und ihre ständige Hilfs- und Diskussionsbereitschaft.

Ferner danke ich Herrn Gerhard Schott, Herrn Uwe Branczyk sowie dem Team von der feinmechanischen Werkstatt des PCI, ohne die die Experimente oft so nicht möglich gewesen wären.

Very special thanks to Dr. Mike Drake and Dr. Todd Fansler from General Motors R&D who taught me to be a better scientist, for the tremendously good and instructive time I spent at the Warren Tech Center and for their continued interest in my work.

Für die Finanzierung dieser Arbeit im Rahmen des SFB 359 sowie des Graduiertenkollegs 1114, danke ich der Deutschen Forschungsgemeinschaft.

Nicht zuletzt jedoch danke ich meiner Familie und meinen Freunden, ohne deren Rückhalt und Zuspruch diese Arbeit niemals Wirklichkeit geworden wäre.

Ich danke meinen Eltern und Geschwistern, die mich immer unterstützt haben, besonders meiner Schwester, Susanne Düwel, für die Durchsicht dieser Arbeit

Ganz besonders danke ich meinem Freund, Jörg Fick, für alles.

Ich erkläre hiermit, dass ich diese Arbeit selbständig verfasst und keine anderen als die angegebenen Quellen und Hilfsmittel benutzt habe.

Heidelberg, 5. März 2007 ……...

(Isabell Düwel)